STRAINED LAYER InGaAs/GaAs SINGLE QUANTUM WELL LASERS UNDER HIGH INJECTION.

Raghuraman Ranganathan
B.Sc (Physics), D. G. Vaishnav, Madras, India, 1984
M.Sc (Physics), Indian Institute of Tech., Madras, India, 1986
M.S. (E. E.), Indian Institute of Tech., Madras, India, 1990

A dissertation submitted to the faculty
of the Oregon Graduate Institute
of Science & Technology
in partial fulfillment of the
requirements for the degree
Doctor of Philosophy
in
Electrical Engineering

April 1993

The dissertation "Strained layer InGaAs/GaAs single quantum well lasers under high injection" by Raghuraman Ranganathan has been examined and approved by the following Examination Committee:

Reinhart Engelmann, Thesis Advisor
Professor

Fred J. Holmes
Professor

Richard K. DeFreez
Associate Professor

Kirk P. Boyer
Manager, Tektronix Inc.

ACKNOWLEDGEMENTS

To all who have made this dissertation possible I wish to express my sincere thanks and appreciation for their constant encouragement and timely suggestions.

To my supervisor, Dr. Reinhart Engelmann, whose invaluable guidance, support, and funding was so critical for successful completion of this thesis, I would like to express my gratitude. In particular his comments were of enormous help in putting the results of this research in proper perspective and making this thesis a reality. The many discussions that I had with him has helped widen not only my technical knowledge but also my appreciation of the finer aspects of life beyond academics. I consider myself fortunate and lucky to have had such an incredibly supportive professor as my advisor in spite of all my foibles as a graduate student.

To Dr. Richard DeFreez, who "infected" me with the "zeal" for experimental research and was a constant source of inspiration, I am most grateful. I would also like to sincerely thank him for providing necessary equipment and technical assistance from his lab towards my research.

To Dr. Fred Holmes and Dr. Kirk Boyer, I am very thankful for their participation on my thesis examination committee and their time and efforts in careful examination of my thesis. I wish to thank Dr. John Arthur and Mr. Leon Ungier of Oregon State University who were instrumental in providing me with the wafer without which this study would have not been so successfully completed in time. Dr. Kirk Boyer and Dr. Lee Van Nice helped

me a great deal, taking time off their busy schedule, teaching me the necessary processing and also allowing me to use the facilities in their Solid State Laboratory at Tektronix.

To my fellow, graduate students, past and present, Dr. Nu Yu, Dr. David Bossert, CangSang Zhao, Yijun Cai, Marc Felisky, and to department staff member Peter Carleson go many thanks for their assistance and contributions.

To Deva & Sumita, Sudharshan & Jalaja, Rajesh, Sukumar and Yeshwant who were constant companions during my many ups and downs in my graduate life at OGI, I wish to offer my special thanks. I can consider myself to be truly lucky to have been amidst such a wonderful group after having come a long way from India.

Few words could aptly describe my true sense of appreciation for all that my parents have done with their love, affection and constant encouragement to help me to try and be the best.

This work was supported by Siemens Research Laboratories. I would like to thank Mr. Klaus Mettler for the research grant, devices and the laser mount from Siemens. I am grateful to Dr. Ian Goodridge (UET, Beaverton) for donating the optical table. I would like to acknowledge the special efforts towards the generous equipment grants from Tektronix, Beaverton, for which Mr. Rick Rummel (Tektronix) provided advice in equipment selection and from HP Labs, Palo Alto, CA, for which Dr. Waguih Ishak provided support of the grant application and direct equipment donation and Mr. Ken Matheson of the local sales office (HP) provided advise and support.

Table of Contents

ACKNOWLEDGEMENTS iii

LIST OF FIGURES vii

LIST OF TABLES x

ABSTRACT xi

1. INTRODUCTION 1

2. HIGH INJECTION OPERATION OF STRAINED-LAYER LASERS 9

    2.1 Introduction 9

    2.2 Design considerations 10

        2.2.1 Threshold current 10

        2.2.2 Carrier spill-over 14

    2.3 Wavelength switching in strained layer lasers 17

3. TIME-INTEGRATED OPERATING CHARACTERISTICS AND WAVELENGTH SWITCHING 22

    3.1 Introduction 22

    3.2 Device structure and fabrication 22

    3.3 Optoelectronic characterization vs. cavity loss 25

        3.3.1 Light current characteristic 27

        3.3.2 Threshold current 36

        3.3.3 Internal loss and quantum efficiency 41

    3.4 Spectral characteristics of wavelength switching devices 53

3.4.1 Experimental set up 53
3.4.2 Devices 56
3.4.3 Measurements 57
3.4.3.1. The 15 μm × 355 μm Device 57
3.3.4.2. The 15 μm × 575 μm Device 64
4. TEMPORAL STUDIES OF WAVELENGTH SWITCHING 71
4.1 Introduction 71
4.2 Experiment 72
4.2.1 Devices 72
4.2.2 Set up for spectral studies 72
4.2.3 Set up for dynamic studies 73
4.3 Results and discussion 75
4.3.1 Spectral studies 75
4.3.1.1 Device characteristics (15 μm × 200 μm) 75
4.3.1.2 Spectral characteristics (gated measurements) 82
4.3.2 Dynamic studies 93
4.3.2.1 Device characteristics (15 μm × 600 μm) 93
4.3.2.2 Sub-nanosecond resolved light pulse 95
4.3.2.3 Relaxation oscillation frequency 101
4.3.2.4 Damping 112
5. DEVICE CHARACTERISTICS UNDER QUASI-DOUBLE-HETEROSTRUCTURE OPERATION 117

5.1 Introduction........117
5.2 Device Structure and Threshold Characteristics........119
5.3 Experimental Technique........120
5.4 Results........124
5.4.1 Differential Gain........124
5.4.2 Mode Shift and Differential Index........132
5.4.3 Linewidth enhancement factor........135
5.5 Discussion........138
6. CONCLUSIONS........141
REFERENCES........145
APPENDIX A : Processing of laser chips........154
APPENDIX B : Temperature control circuit........157
VITA........159

List of Figures

2.1 Calculated gain spectra for a Separate Confinement Heterostructure (SCH) single quantum well laser 16

2.2 Pictorial representation of recombination in a SCH single quantum well laser 19

3.1 Schematic representation of the epilayer structure grown by Molecular Beam Epitaxy (MBE) technique 23

3.2 Schematic representation of the measurement set up for average power output of laser using Tektronix digital photometer 26

3.3 The light-current for 50 μm × 865 μm in pulsed operation 29

3.4 The light-current for 50 μm × 400 μm in pulsed operation 30

3.5 The light-current for 50 μm × 200 μm in pulsed operation 31

3.6 Lateral modes of 50 μm × 200 μm at 958 nm and 911 nm 32

3.7 The light-current for 15 μm × 400 μm in pulsed operation 34

3.8 The light-current for 15 μm × 400 μm in pulsed operation 35

3.9 External differential efficiency vs. mirror loss 43

3.10 Cavity length dependence of threshold current density for broad area (50 μm) stripe devices 45

3.11 The light-current and shift in lasing wavelength as a function of drive current for 50μm × 200 μm device 46

3.12 Cavity length dependence of threshold current density for narrow stripe (15 μm) devices 48

3.13 Stripe width dependence of threshold current density for devices with cavity length of 355 μm ... 49
3.14 The light current and shift in lasing wavelength with drive current for 15 μm × 355 μm device ... 51
3.15 The light-current and shift in lasing wavelength with drive current for 15 μm × 575 μm device ... 52
3.16 Computer controlled experimental arrangement for time-averaged spectrally resolved near field measurements ... 54
3.17 Range of measurement, as indicated in the light-current curve, chosen for spectral measurements on 15 μm × 355 μm device ... 58
3.18 Spectrum and gain at 236 mA for 15 μm × 355 μm device ... 59
3.19 Spectrum and gain at 302 mA for 15 μm × 355 μm device ... 60
3.20 Spectrum and gain at 330 mA for 15 μm × 355 μm device ... 61
3.21 (Netgain . Length) product at various injection levels ... 63
3.22 Spectrum at 285 mA for 15 μm × 575 μm device ... 65
3.23 Spectrum at 400 mA for 15 μm × 575 μm device ... 66
3.24 Spectrum at 453 mA for 15 μm × 575 μm device ... 67
3.25 Spectrum at 500 mA for 15 μm × 575 μm device ... 69
3.26 Spectrum at 550 mA for 15 μm × 575 μm device ... 70
4.1 Sub-nanosecond resolved light pulse measurement set up ... 74
4.2 (a) Light output and (b) lasing wavelength for 15 μm × 200 μm ... 76
4.3 Set up using 200 MHz EG&G Judson photodetector ... 78
4.4 Light pulse as detected by FFD 200 for 15 μm × 200 μm ... 79
4.5 Spectrally resolved light pulse detected with FFD 200 ... 81
4.6 Spectra (Gated : single pulse) at 155 mA ... 83

4.7 Spectra (Gated : single pulse) at 165 mA 84
4.8 Spectra (Gated : single pulse) at 170 mA 85
4.9 Spectra (Gated : single pulse) at 190 mA 86
4.10 Spectra (Gated : double pulse) at 167 mA 88
4.11 Spectra (Gated : double pulse) at 185 mA 89
4.12 Spectra (Gated : varying pulse separation) at 167 mA 90
4.13 Spectra (Gated : varying pulse separation) at 185 mA 91
4.14 (a) Light output and (b) lasing wavelength for 15 μm × 600 μm 94
4.15 Average light pulse traces for 15 μm × 600 μm device 96
4.16 Single sweep trace for 15 μm × 600 μm at 782 mA 98
4.17 Single sweep trace for 15 μm × 600 μm at 838 mA 99
4.18 Injection level dependence of the FWHM of the relaxation oscillation peak 102
4.19 Power dependence of the square of the resonance frequency 106
4.20 Injection level dependence of the parameter G_0 109
4.21 Power dependence of the damping, Γ 114
5.1 Light-current curve for 5 μm × 200 μm 121
5.2 Evolution of mode spectrum with drive level 125
5.3 Gain spectrum at 71 mA, 73 mA and 75 mA 126
5.4 (Netgain.Length) product variation with current at 877 nm 127
5.5 Spectral variation of the differential gain 129
5.6 Total mode shift at 877 nm 132
5.7 Spectral variation of the mode shift 134
5.8 Spectral variation of the linewidth enhancement factor 136

List of Tables

3.1a Electrical and optical characteristics : Wafer 1-17-12-90/2A....................37

3.1b Electrical and optical characteristics : Wafer 1-17-12-90/2B....................38

5.1 Parameters used in the estimation of carrier density..............................131

5.2 Estimated values at the optimum wavelength (λ = 877 nm).................139

ABSTRACT

STRAINED LAYER InGaAs/GaAs SINGLE QUANTUM WELL LASERS UNDER HIGH INJECTION

R. Raghuraman

Oregon Graduate Institute, 1993

Supervising Professor : Reinhart Engelmann

The widespread interest in strained-layer InGaAs/GaAs quantum-well (QW) lasers which extend the available wavelength emission beyond GaAs has been a result of advances in the epitaxial growth of strained layers. Although extensive research has been done on these lasers, not much is understood about the modified device properties under fairly high injection conditions, which is of both practical and theoretical interest. In this dissertation, the experimental studies on the optical characteristics of devices, in pulsed operation, is reported for single quantum well $In_{0.2}Ga_{0.8}As$ strained layer in a Separate Confinement Heterostructure (SCH). At high injections. with substantial carrier spill-over into the barrier (GaAs) regions, the appropriate cavity dimensions for operation in two or more wavelengths has been investigated. Time integrated and time resolved spectral investigations coupled with sub-nanosecond resolved light pulse measurements indicate the complex nature of the switching mechanism as a result of gain

nonlinearities due to spectral and spatial (not only laterally but also vertically due to carrier spill-over in to the barrier) hole burning mechanisms. A power dependent nonlinear gain contribution even at lower powers lead to the instability condition of gain enhancement (dg/dP>0). This resulted in a de-damping of the resonance frequency whose effect decreased with increasing power. Subsequently gain suppression effects forced the relaxation oscillation frequency to saturate. The nonlinearities facilitated the switching of lasing emission to shorter wavelengths. Furthermore, the properties of strained layer devices have been investigated under substantially high injections with complete carrier spill over into the barrier regions. A remarkably low linewidth enhancement factor and higher differential gain have been found in spite of the device lasing in a quasi-Double Heterostructure (quasi-DH) mode from the GaAs barrier regions. The experimental results at high injections makes such lasers attractive for utilizing their wavelength switching capability over a wide wavelength range by proper control of losses in the lasing cavity.

Chapter 1

INTRODUCTION

Semiconductor laser sources have been found to be promising candidates for use in high-speed photonic integrated circuits for optical interconnections in large computer systems and in optical communications. The properties of a new class of superlattices and quantum-well heterostructures are in many ways superior to those of bulk materials. Some of their superior performance characteristics are lower threshold current density, higher external quantum efficiency, less temperature dependent threshold current, higher differential optical gain, improved coherency with reduced lasing linewidth, superior mode stability, larger modulation bandwidth and reduced chirping during modulation[1].

Improvements in the above mentioned characteristics have been a result of increased understanding of controlled epitaxial growth and device operation. The unique combination of practical, physical, electrical, optical and chemical features has been the primary reason for the development of the most sophisticated heterostructure AlGaAs/GaAs laser system. The chemical system is such that it is feasible to grow high quality structures with basic epitaxial growth methods, such as liquid phase epitaxy (LPE), and with more advanced thin layer epitaxial methods such as metalorganic chemical vapor deposition (MOCVD) and molecular beam epitaxy (MBE). The

fortunate coincidence that AlAs and GaAs have, for all practical purposes, the same lattice constant ($\Delta a/a < 0.12\%$) is probably the single most important feature of the AlGaAs/GaAs heterostructure system. Without any problems of lattice mismatch and the associated dislocation formation, it allows design of any structure until the onset of indirect transitions. From such lattice matched AlGaAs/GaAs conventional double heterostructure and quantum well lasers, the range of available wavelengths is from 0.65 μm to 0.88 μm. The band edge for GaAs defines the long wavelength limit and AlGaAs active layers or quantum size effect, or both, are used to achieve emission at shorter wavelengths. The increased influence of the large mass indirect conduction band minima at X and L on direct recombination processes near Γ limits the shortest wavelength possible.

After AlGaAs/GaAs, the other material system for lasers that has been studied extensively is InGaAsP/InP. Though the chemical system is suited to LPE growth, it is difficult to handle elements like Phosphorous in the more advanced epitaxial growth systems like MOCVD and MBE, although it is being used in both systems. In addition for obtaining a lattice match between InGaAsP and InP, it is necessary to have better control of the stoichiometry during growth of the alloy. The application as a source in long wavelength communications, in the 1.3 and 1.55 μm windows with minimum dispersion and low loss fibres, has been a strong catalyst for developing this heterostructure system. The range of wavelengths achievable in this system from conventional double-heterostructures and quantum well heterostructure lasers are between 1.1 μm and 1.7 μm. Insufficient heterostructure conduction band discontinuity determines the short

wavelength limit and devices operate with high threshold carrier densities due to poor carrier confinement. The band edge of the ternary InGaAs lattice matched to InP provides the long wavelength limit.

Such lattice matched heterostructure systems, however, do not offer operational laser systems in the wavelength range of 0.88 μm - 1.1μm. Some important applications require laser emission in this range, including frequency doubling of wavelengths around the 1.06 μm emission of Nd:YAG solid state lasers, and pumping of Er-doped silica fiber amplifiers at 0.98μm. The most suitable material system for this wavelength range of interest, from the available direct gap III-V compound semiconductors, is $In_xGa_{1-x}As$. The addition of Indium in GaAs allows variation of the bandgap monotonically from 1.41 eV (GaAs) to 0.36 eV (InAs). However, no binary substrate material that is lattice matched to the alloy is available in this range of wavelengths. InAs has a lattice constant of 6.058 Å. To grow epitaxial films of InGaAs on GaAs (lattice constant of 5.653 Å), suitable for laser operation, it is therefore necessary to violate the lattice matching requirement between the two material systems. Thus a very large mismatch ($\Delta a/a$ as much as 3%) has to be accommodated in such a heterostructure system. However, with advanced techniques like MBE and improvement in control of stoichiometry and growth conditions, it has been shown that epitaxial films whose lattice constant differs from that of the substrate, can be constructed with fairly low defect density if they are sufficiently thin[2,3].

The film thus grown is structurally constrained to be coherent with the substrate by forcing the lattice constant of the film to adjust in the plane of growth to match that of the substrate. The elastic deformation due to a stress

on the film applied by the larger volume substrate forces the film to be "strained" in response. Such epitaxial layers are referred to as being "coherently strained" or "pseudomorphic". There are however fundamental limits to the thickness to which these structures can be grown maintaining the necessary "coherency" with the substrate. The energy associated with the elastic deformation in the pseudomorphic film imposes this constraint[3]. For low enough Indium concentration the limiting thickness is large enough to be useful for growth of suitable devices. For instance, with 30% Indium, epitaxial films with thickness of 10nm can be grown maintaining the pseudomorphic nature[4].

After initial work in the early 1970's on strained-layer superlattices, most of the work on devices using strained-layers has occurred in the past few years. Exhaustive accounts on different semiconductor material systems using strained-layers are available[5,6]. Development of such devices as photoexcited lasers[7-9], quantum well injection lasers[10-15], light emitting diodes[16,17], photodetectors[18], and high-electron-mobility-transistors[19,20] using strained layer have been a result of the progress in fabrication of pseudomorphic semiconductor structures.

Injection lasers utilizing such InGaAs strained-layers have many interesting properties. Lower transparency currents[21], low threshold current density broad area devices[13], and relatively high continuous wave output powers[22,23] have been obtained. In addition, higher modulation speeds[24] through enhanced differential gain[21,25,26], larger carrier dependence of the real refractive index[25], and reduced linewidth enhancement factor[25,27] has been observed compared to their GaAs/AlGaAs unstrained counterparts. The

further improved properties of the quantum well lasers with the addition of strain in the quantum well layer, reflects the unique advantages of lasing from the lowest (n=1) energy subbands produced by the quantum size effect and the strain induced splitting of the heavy and light hole level in the valence band[28]. In the case of compressive stress as in InGaAs on GaAs, the holes at the highest valence band maximum are "heavy" in the direction of quantization (perpendicular to the epitaxial film plane). The biaxial strain gives rise to an isolated, anisotropic heavy hole band with in-plane light-hole character (in compressive strain). The simultaneous reduction of the valence band density-of-states effective mass resulting in minimized asymmetry between the valence and conduction bands has been tendered as an explanation for the observed improvements. The biaxial layer strain alters the atomic bond lengths and bond angles thus resulting in the modification of the upper valence bands[29].

Design considerations for the strained-layer single quantum well lasers have to take into account the constraints imposed by the critical thickness of the strained layer on the one hand[30] and the quantum well thickness optimized for a particular application on the other. This results in a need for an indepth and systematic study of such devices to optimize the cavity specifications both in terms of its structure and the electrical and optical characteristics depending on the application. When properly designed, the mismatched layer is thin enough that the difference in lattice constants is accommodated by elastic strain instead of misfit dislocations[3]. Several different structures such as ridge waveguide lasers[14,31,32], transverse junction lasers[29], oxide-defined[33,34] and shallow mesa stripe-geometry gain-guided

devices[30] have been reported with excellent performance for a variety of optical confining layer AlGaAs compositions, (carrier collection) barrier layer (Al)GaAs compositions, InGaAs quantum well active regions, and other growth parameters, using either MOCVD or MBE growth techniques.

In this thesis study particular interest has been placed on the behavior of strained-layer quantum well lasers at extremely high injection levels where carrier spill over into the barrier region becomes significant due to insufficient barrier height at the InGaAs/GaAs hetero-interface resulting in poor confinement of carriers. Recombination from the barrier would then dominate at sufficiently high drive levels with devices eventually lasing at the shorter barrier wavelength which has been observed by Shieh *et al.*[35] and by Beernink *et al.*[36] in narrow stripe gain-guided InGaAs/GaAs single quantum well lasers. In analyzing the gain induced antiguiding effect in such lasers[35], it was felt that the strain-modified band structure could influence the strength of the gain induced antiguide since they are expected to be closely related. The difference in the gain guiding behavior between the InGaAs/GaAs and GaAs/AlGaAs quantum well lasers resulted in the observed larger lateral leaky mode losses of the former. A comparative study of the threshold current behavior with stripe width showed dramatic difference between the unstrained GaAs/AlGaAs and strained InGaAs/GaAs systems. Though the threshold current in the former was found to decrease with decreasing stripe-width, consistent with reduced pumping area, the latter system showed a relatively strong increase when reducing stripe widths. With the lateral optical loss being no longer negligible, coupled with a smaller confinement factor in single quantum well lasers, increased pumping

levels are thus necessary to counter the losses. Here it should be noted that gain saturation effects are present in the strained system even at relatively low values for the modal gain. Such saturation behavior could also potentially affect the high speed performance, theoretically predicted to be high (up to 90 GHz[37]) due to the expected enhancement of differential gain. The well known saturation of linear gain in quantum wells[1] leads to rapid bandfilling and population of higher levels, eventually including the barrier and, thus, provides an additional incentive to investigate such devices for their potential in wavelength switching applications.

The motivation to thoroughly study the optical characteristics under fairly high injections in a systematic manner, provided by the factors discussed above, is to understand better the spectral and dynamic behavior associated with substantial shifts in the operating wavelength from the quantum well value to the distinctly shorter barrier recombination. The work presented in this dissertation focusses on the experimental characterization of single quantum well devices under pulsed operating conditions in terms of their optical output behavior through extensive spectral (both time averaged and partially time resolved) and sub-nanosecond resolved light pulse measurements. By appropriate choice of cavity dimensions it is shown that controlled switching of lasing emission, between the n=1 and the n=2 quantum levels and eventually to the barrier, with increasing drive level, is possible. Furthermore, by understanding the spectral content at different drive levels and correlating the results to the observed light pulse behavior, a better handle is thereby obtained to explain the influence of nonlinearities, in addition to the larger carrier induced antiguiding observed, that not only

causes the switching behavior, but also limits the achievable dynamic characteristics in strained quantum well lasers. With the increased losses in narrow stripe devices, the question also arises as to how such a device, that operates from the barrier, so to speak in a purely "quasi double heterostructure" mode, influences such properties as linewidth enhancement factor, which when operated on the lowest quantum well transition, is expected to be reduced by a factor of more that two thirds[38] in strained quantum well lasers based on the expected enhancement of differential gain. In order to provide a sound basis for comparison this work addresses only single quantum well stripe-geometry gain-guided semiconductor diode lasers with a 20% Indium concentration in the active layer (quantum well).

The organization of the dissertation is as follows. Chapter 2 provides a brief analysis of the high injection conditions and its influence on the device operation. The device structure, processing and characterization in terms of its fundamental electrical and optical characteristics, as well as the results of a systematic evaluation of the (time-averaged) switching of operating wavelength with appropriate choice of cavity dimensions is provided in Chapter 3. Chapter 4 deals with extensive spectral measurements to determine explicitly the spectral content (in a partially time resolved manner) as a function of injection level and also correlate the results to sub-nanosecond resolved light pulse observations thus obtaining a better understanding of the possible physical mechanisms involved in the switching process. The experimental results on the device characteristics under quasi-double heterostructure operation is presented in Chapter 5. Finally, conclusions and suggestions for future work are given in Chapter 6.

Chapter 2

HIGH INJECTION OPERATION OF STRAINED-LAYER LASERS

2.1 Introduction

A substantial amount of work is being done to develop high quality and high performance strained layer lasers toward the goal of achieving reliable operation suitable for application in a variety of operating conditions. The extent of stress[31] in a typical strained active quantum well layer in the InGaAs/GaAs system is about 1 - 3×10^{10} dyne/cm^2. This might cause dislocations fatal to lasing especially at high power operations essential for a practical pumping source for Er^{3+} - doped fiber optical amplifiers[39]. To identify optimal structures, different devices, including ridge waveguide, buried heterostructure, oxide-defined and mesa stripe-geometry gain guided lasers, and so on, have been developed. This chapter provides an overview of the device structure with a strained active layer and the constraints in particular for operation under high injection when losses in the cavity are higher. Implications of carrier spill-over out of the quantum well into the surrounding regions are discussed followed by the final section on possible applications in wavelength switching.

2.2 Design considerations

2.2.1 Threshold current

Previously unattainable wavelengths of operation in semiconductor lasers have been successfully achieved by suitable variation of the bandgap of the active region through incorporation of strain with the loosening of the lattice matching constraint in such heterostructures[11,13,14,22,29,40]. The biaxial strain thus induced in strained-layer $In_xGa_{1-x}As/GaAs$ quantum wells has been shown by recent studies to induce a lowering of the in-plane effective mass through lifting of the degeneracy of the valence heavy and light hole bands[41,42]. It has been shown theoretically[28,37,43,44] and verified experimentally[24] that the resulting reduced density of states in the valence band provides a reduction in the threshold current for such strained layer devices.

The threshold current in a laser is determined by the threshold current density and the physical area of the active layer. It would be natural to consider reducing the threshold current by minimizing the width and length of the laser cavity, the current density for transparency and also to overcome the cavity loss and carrier leakage, if any. In a strained layer laser, the reduced asymmetry between the valence and conduction bands helps to achieve lower transparency currents. It is well known that the excess carrier density required to invert the bands, which requires that the separation of the quasi-Fermi levels be larger than the bandgap energy, is typically greater than 10^{18} carriers

per cm^3 (both electrons and holes). The quality of the epitaxial layers from which the junction is formed will influence the ability to achieve this excess carrier density. Improper crystal growth could lead to large number of energy levels deep within the band gap. This in turn could lead to increase in nonradiative recombination through these levels and hence reduce the available carrier density for inversion requiring higher injection drive levels. With sufficient progress in the growth techniques, it has been possible to reduce the extent of device imperfections like junction leakage via deep levels or waveguide imperfections which could otherwise play a significant role in determining the threshold current density.

Reducing the cavity length gives a monotonic decrease in threshold currents in typical double heterostructure lasers. However, it has been found that for single quantum well lasers the threshold current rises rapidly for cavity lengths below a critical value[45]. This behavior was attributed to the pronounced linear gain saturation in the quantum well structure[46,47] due to the small carrier confinement factor. It is interesting to note in this context that a more dramatic increase of threshold current towards shorter cavity length has been observed for broad stripe strained layer InGaAs/GaAs single quantum well lasers[48] as compared to their unstrained counterparts[49]. In addition, Shieh *et al.*[35] have observed a rapid increase in the threshold current when the stripe width was made narrow in a gain-guided stripe-geometry strained-layer laser. The unusually large index antiguide resulting from the injected carriers increased the lateral optical losses as the stripe width was reduced. The unstrained GaAs/AlGaAs single quantum well lasers, unlike the strained layer devices, exhibited a decrease in threshold

current as the stripe width was reduced consistent with a reduction in the pumping area. Whereas the gain induced antiguide effect in the unstrained GaAs/AlGaAs quantum well laser system is much weaker than in the unstrained GaAs double heterostructure lasers[50], the modification of the band structure in the strained InGaAs/GaAs quantum well lasers was felt to cause the observed difference in the gain-guiding behavior between the two quantum well systems. Such a conclusion was arrived at from an investigation of the far fields and estimation of the carrier induced change of the index and the Petermann K factor[51]. The larger values for the K factor compared to similar GaAs/AlGaAs unstrained quantum well lasers confirmed the larger antiguiding and hence the increased lateral losses and the higher thresholds for narrow stripe strained-layer devices.

By suitable choice of the thickness of the quantum well one can select the wavelengths at which the device operates. A wider well would reduce the energy separation between the n=1 and the n=2 transitions and vice versa. Availability of higher subbands in the quantum well is dependent on the depth of the quantum well, i.e., the indium concentration. Furthermore, it is necessary to consider the critical thickness limits corresponding to the percentage of Indium in such strained layer structures vis a vis the optimum quantum well thickness with regard to improved performance. It has been reported in the literature that there exists an optimum thickness for a given concentration of Indium in the quantum well[52]. In evaluating the dependence of threshold current density on the quantum well width, it was indicated that there was an increase in the threshold for smaller widths, whereas it did not change much for widths between 40 Å and 90 Å at 25%

Indium concentration in the active layer. The reason for the existence of a minimum in the threshold current for a given Indium concentration was attributed to the capture time of electrons which reaches a minimum and is a monotonic function of the width[53]. Hence for a narrow well the collection efficiency becomes poor resulting in a higher threshold current density. Choosing the width of the quantum well between 40 Å and 90 Å, the optical cavity losses, including waveguide imperfections and lateral leaky losses, would essentially determine the threshold characteristics of the strained quantum well lasers.

Interestingly, the maximum modal gain available in the quantum well is independent of the thickness if the confinement factor is assumed to vary linearly with well thickness as in the case of optical waveguides formed by a separate confinement heterostructure. A reduction in the confinement factor when decreasing the well thickness, is compensated by an increase in the available density of states, which is inversely related to the well thickness[54]. Comparing, for the lowest QW transition, the maximum modal gain available in a compressive-strained system, like the InGaAs/GaAs, to the unstrained system, like GaAs/AlGaAs, it is found to be smaller by one half in the former[55]. Thus strained QW systems are expected to shift more readily to the shorter wavelength transitions that correspond to the available higher energy levels, when the optical loss from the laser cavity is increased. Even carrier spill-over may result.

2.2.2 Carrier spill-over

With higher losses leading to higher thresholds, the carrier distribution in the surrounding regions (barriers and cladding) need to be considered at the required higher injection levels. Carrier "leakage" out of the quantum well is then an important contribution to the total current. Such a leakage mechanism, that fills up the higher energy levels, becomes stronger with increased injection as the quasi-Fermi levels move farther into the bands. The potential height at the well/barrier interface, essentially determined by the Indium concentration as in the InGaAs/GaAs system, controls the extent of this spill-over of the carriers. In addition, the concentration of Al influences the degree to which carriers are present in the cladding ($Al_xGa_{1-x}As$). This in turn influences the current injection efficiency[56] which is the ratio of the current into the active layer to the total current. Spill-over is important in the case of QW lasers than in conventional DH lasers because there are additional layers, other than the active layer, with a direct band gap where carrier recombination can take place.

Knowledge of the potential steps and the positions of the quasi-Fermi levels helps determine the carrier leakage out of the quantum well into the guiding region[57]. However, due to the difference between the conduction and valence bands in terms of the effective mass, the spill-over of electrons and holes tends to be different. An internal electro-static field is thus established and forces a reduction in the difference in the carrier distributions in the two bands. This injection induced confinement effect has been considered in a simplified approach[58] based on the assumption of flat quasi-Fermi levels and

charge neutrality in the quantum well and barrier regions with step-like band profiles. By assuming that the space charge distribution induced by the injection is an interface dipole sheet, the built-in potential at the hetero-junction between the well and the barrier is forced to change to offset the virtual charge built up. Equivalently, to fulfill the charge neutrality condition the band offset is used as an adjustable parameter. Furthermore, Cai *et al.*[58] found that this type of carrier confinement is effective within a certain range of carrier sheet densities (7.0×10^{12} cm^{-2} - 8.0×10^{13} cm^{-2} for the total injected carrier sheet density). Below the lower value the spill-over becomes insignificant, and above the upper limit the spill-over is so large that the device operates like a double-heterostructure laser. The value for the band offset was found to be critically influencing the extent of charge neutrality between the two limits for the carrier density. For a particular choice of the band offset, estimating the gain spectra, with the barrier recombination also included, clearly showed substantial bandfilling of higher energy subbands in the quantum well and domination by the barrier recombination at fairly high injections. The band offset that best satisfied the imposed charge neutrality constraint was 0.49 . Fig. 2.1 shows the calculated gain spectra for an $In_{0.2}Ga_{0.8}As$/GaAs SCH-SQW laser at 300 °K for T.E. (transverse electric) mode, with the constraint of less than 5% deviation from charge neutrality imposed locally in the quantum well, over a 200 nm wavelength range at different injection levels. The barrier gain was normalized to QW gain using the ratio of the gain confinement factors in the two regions.

Shieh *et al.*[35] found that associated with the increase in threshold current was a dramatic increase in the lasing photon energy from about 1.30

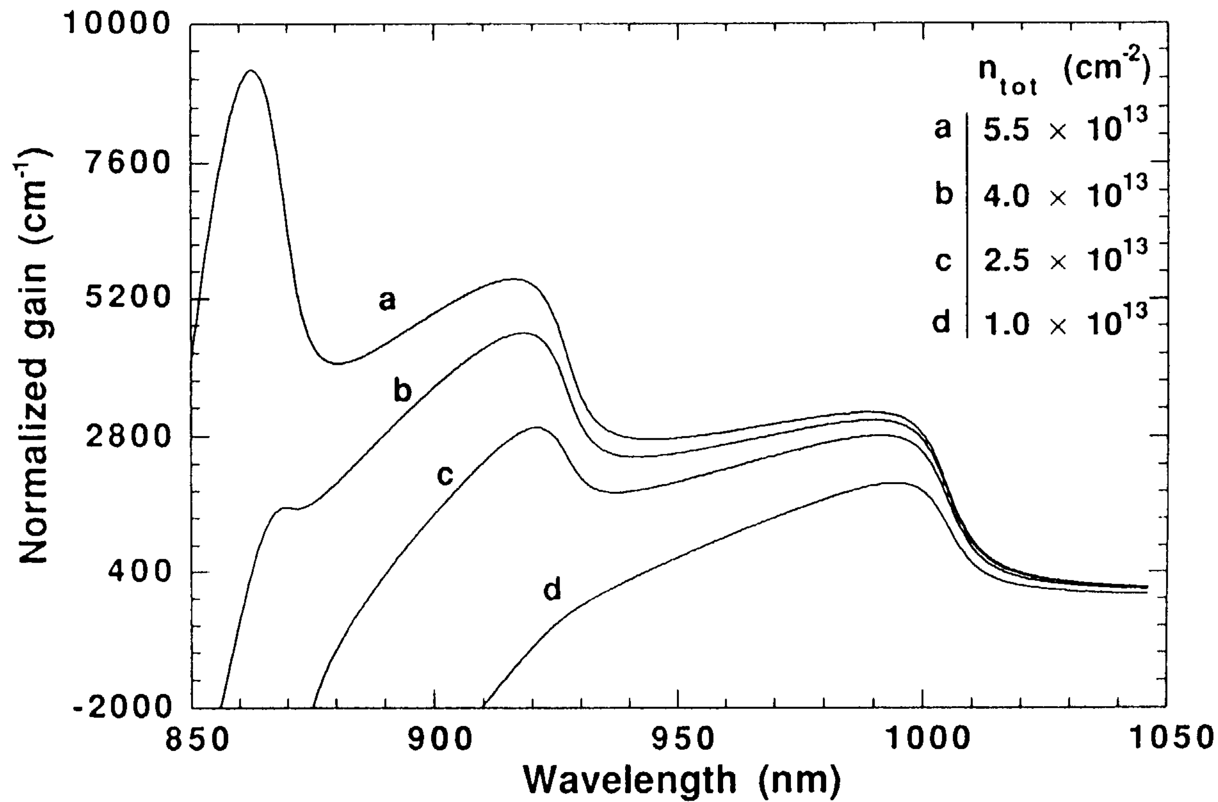

Figure 2.1. Calculated gain profiles at various injected sheet carrier densities (as shown in the inset) for the Separate Confinement Heterostructure (SCH) with an $In_{0.2}Ga_{0.8}As$ single quantum well. Note that at the highest value for n_{tot} (5.5×10^{13} cm^{-2}) the barrier transition (≈ 860 nm) is strong compared to n=1 (≈ 1000 nm) and n=2 (≈ 915 nm).

eV to 1.39 eV when the stripe width was reduced from 50 μm to 15 μm, a shift of about 90 meV, as a result of substantial bandfilling due to the high gain required to overcome the optical losses in the cavity. Beernink *et al.*[36] have also reported the influence of higher refraction losses associated with the strong carrier induced antiguiding resulting in certain devices lasing on higher transitions in the quantum well, and in the GaAs barriers. The quasi-Fermi levels are determined by both the charge neutrality condition and the condition that the net modal gain is equal to the sum of the losses. Hence with sufficient losses, either with a short cavity or a narrow stripe, the increased losses, mirror or lateral, respectively, would prevent the onset of lasing on the quantized levels in the InGaAs, but rather establish lasing in the GaAs barriers.

2.3 Wavelength switching in strained layer lasers

We have seen how the gain in the higher energy states rapidly increases with increasing injection level due to the excessive carrier spill-over from the quantum well to the barrier. With carrier spill-over into the barrier regions becoming an important consideration at high injections shifting of lasing wavelengths to shorter values may occur. Critical thickness constraints on the strained layer[30] need to be balanced with the optimum depth and thickness of the quantum well required for a particular wavelength characteristic when designing the strained-layer devices with wavelength shifting capabilities in mind. This aspect coupled with the well known saturation of linear gain in quantum wells[1] leading to rapid band filling and

population of higher levels with increased losses provides an incentive to investigate such devices for their potential in wavelength switching applications.

Fig. 2.2 provides a simple pictorial representation for the recombination regions depending on the injection level. As mentioned earlier, the location of the quasi-Fermi levels are basically determined by the losses in the cavity. In the case of low injection, where the losses are small, inversion of the band populations occurs when the n=1 level is reached. The device then lases at the wavelength corresponding to the e1-hh1 transition (e1 refers to the first electron level in the conduction band; hh1 refers to the first heavy hole level in the valence band). Operating the device in this injection regime before gain saturation comes into play is important to fully exploit the advantages of a strained quantum well laser. With increased losses, the condition that the net modal gain be equal to the sum of the losses forces the quasi-Fermi levels to be pushed higher eventually making the device operate either on the higher energy subband in the quantum well (n=2 : e2-hh2) or on the higher band of the surrounding barrier layers (GaAs). This is illustrated in the intermediate or high injection case.

Wavelength switching of laser emission has been reported under conditions of high optical loss for unstrained quantum well lasers (GaAs/AlGaAs)[59-61], for a narrow oxide stripe strained-layer single quantum well device (InGaAs/GaAs)[62] and, recently, for buried heterostructure multiple quantum well lasers (InGaAs/GaAs)[63]. Particular attention is needed to the behavior at extremely high injection levels where carrier spill-over into the barrier region becomes significant. This can lead to a substantial

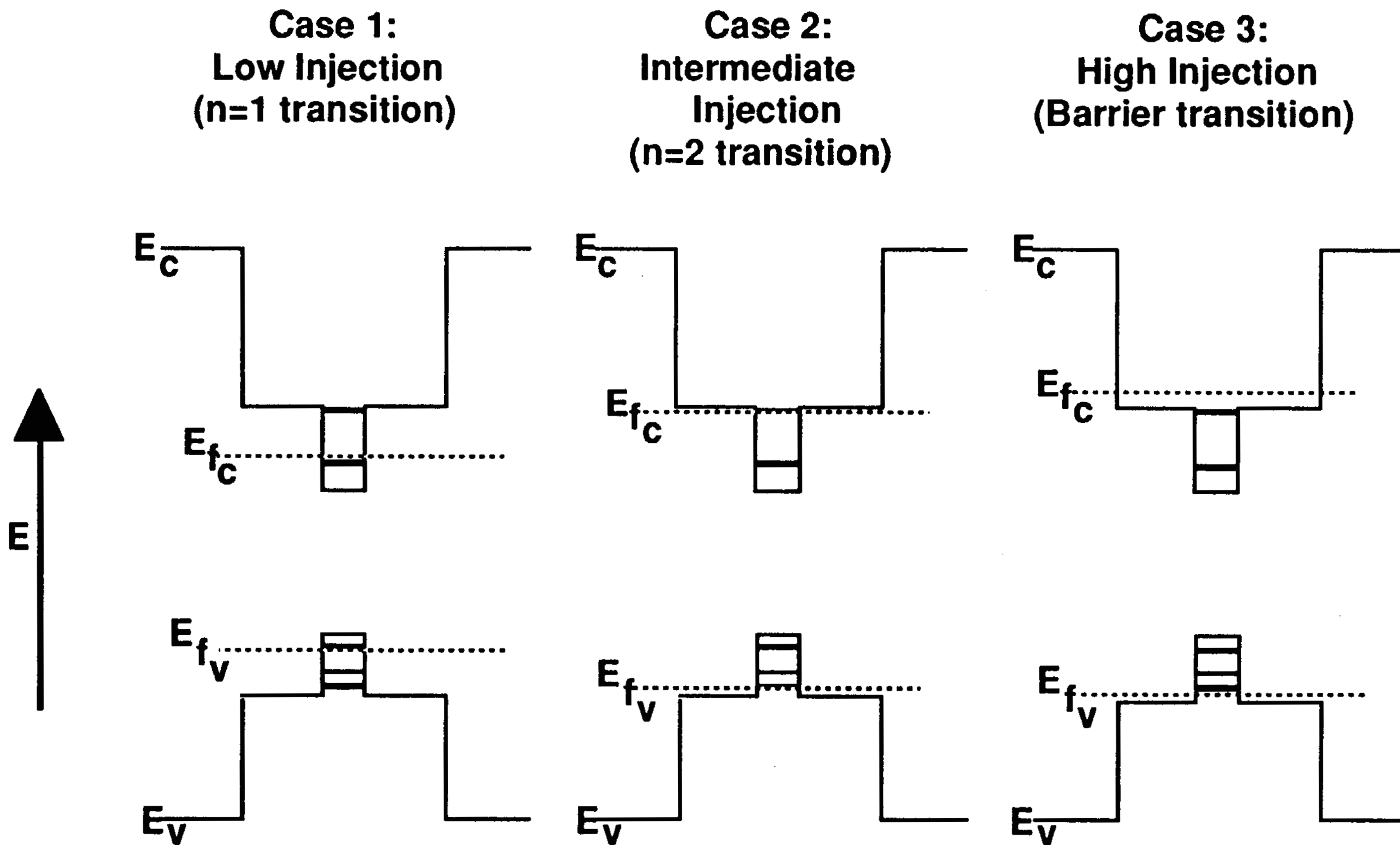

Figure 2.2. Pictorial representation of recombination regimes in a (SCH) single-quantum-well laser. (bold line is for heavy hole and thin line for light hole level in the valence band)

wavelength shift from the QW value to the distinctly shorter value of barrier recombination, a phenomenon particularly useful for wavelength switching applications.

Oscillations of GaAs QW laser diodes whose wavelengths are considerably shorter than the n = 1 quantized state transitions have been explained in terms of gain contributions from the higher (n = 2) energy subbands[64]. In line with our previous discussions, Göbel *et.al.*[65] suggested that the way to achieve laser action involving the n = 2 and higher subbands is to increase cavity losses sufficiently. In a typical Fabry Perot laser with symmetric facets the losses are related to the threshold mode gain as follows :

$$G_{th} = \Gamma\, g_{th} = \alpha_i + \frac{1}{L}\ln(R)$$

The three parameters that could be used to control the loss are the cavity length L, the mirror reflectivity R, and the internal loss α_i. In addition, the local gain, g_{th}, depends on the degree to which the carriers are confined in the well region and the gain confinement factor, Γ, is therefore an important additional consideration in a single quantum well device when compared to a multiple quantum well system[63]. The internal loss α_i also includes the large lateral losses observed in strained layer gain-guided systems[48]. As pointed out before, there is a dramatic increase in the threshold as the stripe width is made smaller due to this lateral loss. The choice of stripe widths, therefore, also influences the overall cavity loss. Thus it is possible, by appropriate combination of cavity length and stripe width, to control cavity loss (mirror

and lateral loss, respectively) given that the mirror reflectivities are not changed (left uncoated in our investigation). Utilizing this idea we have studied a number of devices in a systematic manner and observed transitions to shorter wavelengths including recombination from the GaAs barrier region depending on the cavity specifications. The results will be presented in the next chapter.

Chapter 3

TIME-INTEGRATED OPERATING CHARACTERISTICS AND WAVELENGTH SWITCHING

3.1 Introduction

The electrical, optical, and spectral characteristics may be used to understand the performance of the strained layer single quantum well lasers operated under fairly high injections. In this chapter particular emphasis has been on understanding the behavior in a quasi-static condition where the devices, though operated in pulsed mode, are measured in "averaged" or "time-integrated" sense. After a detailed account of the characterization followed by the demonstration of wavelength switching, the final section will discuss the spectral content, in a "time-integrated" sense, as a function of the drive current with possible mechanisms elucidated for the observed shift in lasing wavelength.

3.2 Device structure and fabrication

The strained InGaAs/GaAs separate confinement single quantum well laser structure investigated is shown in Fig. 3.1. It was grown using a Perkin-Elmer 425B Molecular Beam Epitaxy system[66]. The growth process and

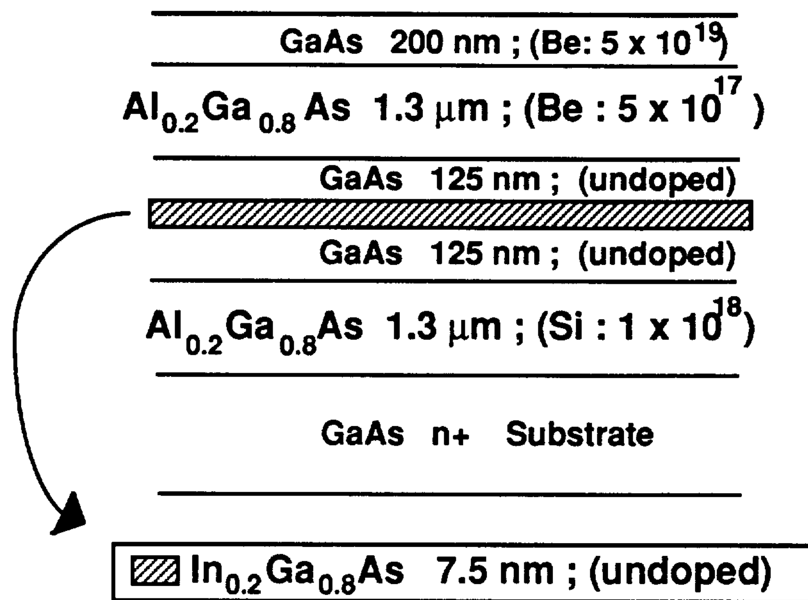

Figure 3.1. Schematic representation of the epilayer structure grown by Molecular Beam Epitaxy (MBE) technique

relevant parameters for a similar strained layer structure but with a graded AlGaAs barrier layer are given in Ref 66. The active layer was 7.5 nm thick $In_{0.2}Ga_{0.8}As$ with a 125 nm GaAs confinement layer on either side, all undoped. These layers were further sandwiched between p- and n- type 1.3 μm thick $Al_{0.2}Ga_{0.8}As$ cladding layers doped with Be (5×10^{17} cm^{-3}) and Si (1×10^{18} cm^{-3}), respectively. The p^+ GaAs contact layer of 200 nm thickness was doped with Be to about 5×10^{19} cm^{-3} for good ohmic contact. The concentration profiles of the grown layers were analyzed using Auger Spectroscopy and found to be consistent with the specifications. Since the preparation of the samples was not done in dust free environments particulate related defects were seen to be present. The pin hole like features could not be removed by use of simple cleaning procedures using solvents.

The as grown wafers were then processed into devices with different cavity lengths and stripe widths using standard photo-lithography, wet chemical etching, metallization techniques and facet cleaving. The complete procedure is presented in Appendix A. Shallow mesa-stripe Schottky barrier confined laser technology[67] was felt to be a convenient and simple way to provide lateral confinement resulting in gain-guiding. The compromise on the choice of ease of fabrication does reflect in higher threshold currents, however. Laser cavities in the range of 200-1000 μm were fabricated by cleaving with no coating or passivation applied to the mirrors.

3.3 Optoelectronic characterization vs. cavity loss

The cleaved devices were characterized by pulsed light-current measurements using the set up shown in Fig 3.2. As shown in the schematic, the laser chip was pressure mounted in a clamp header which was supplied by Siemens. The center pin that provided the path for current was also used to hold the device in place. All devices were mounted p-side up with the facet barely protruding from the edge of the mount without any special heatsinking or good thermal contact with the mount. Care was taken to avoid damaging the stripe by placing the tip of the center pin well away from the stripe area. The temperature of the mount was stabilized using an active circuit with a thermoelectric cooler (MELCOR CP1.0 - 63 - 06L) and a thermistor element (OMEGA F3105) placed close to the laser chip to monitor the temperature of the laser mount to complete the feedback loop. The thermoelectric cooler was carefully placed between the smoothed surfaces of the laser mount holder and water cooling jacket. The water cooling jacket helped in maintaining the "hot" ("cold") junction at the temperature of water ($\approx$ 15 °C) for "cooling" ("heating") periods. The flow rate of the water through the jacket was adjusted so as to minimize turbulence and associated vibration to the laser mount. The temperature dependent voltage generated across the thermistor (RTD) was used to compare with a preset voltage to generate a control voltage for driving the circuit for the thermoelectric cooler. Depending on the sensed voltage (temperature) at the RTD element, heat was either provided to or drawn from the laser mount to maintain the temperature at the set value. The complete circuit to control the drive voltage

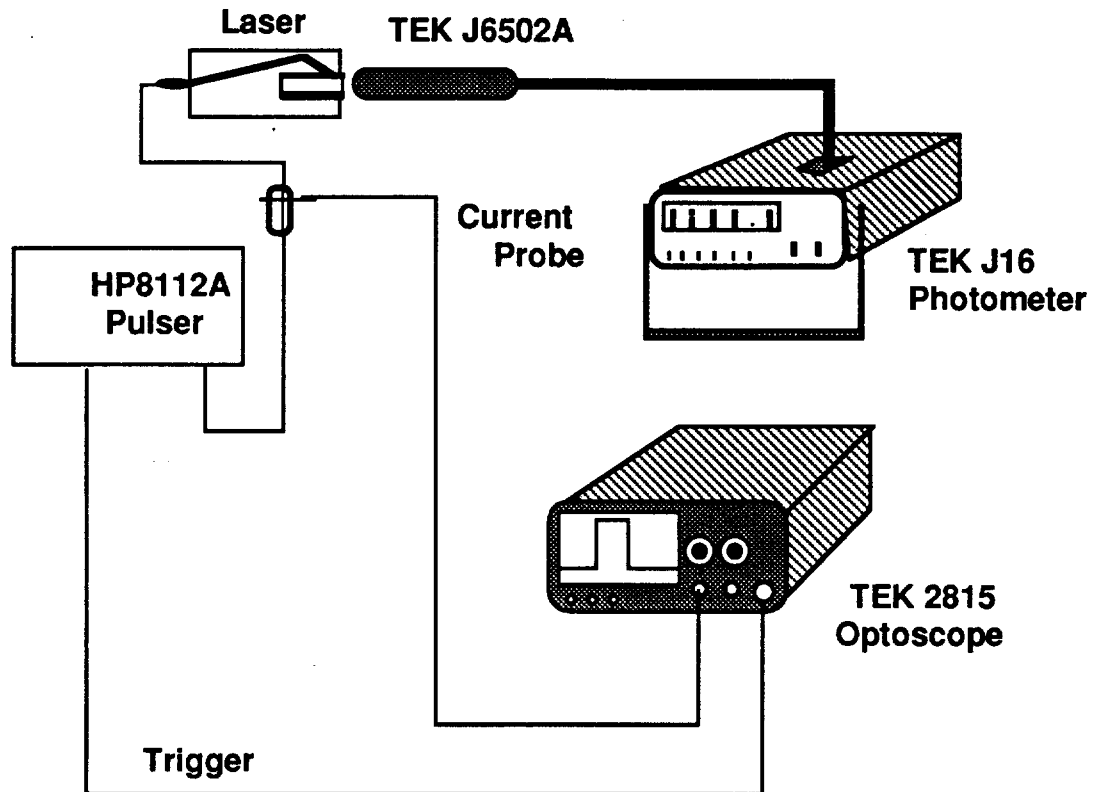

Figure 3.2 Schematic representation of the measurement set up for average power output of laser using Tektronix digital photometer.

for the thermoelectric cooler with the relevant adjustable parameters is provided in Appendix B.

The devices were operated under pulsed operation with pulse widths of 100 ns and 10 kHz repetition rate giving a duty cycle of 0.1% to avoid heating during operation. The drive current was provided by HP214B analog current source (rise and fall times of ≈ 10 ns) for most experiments and by HP8112A digital current source (rise and fall times of 4.5 ns) when low drive currents (< 280 mA) were required. The current pulse was monitored using a Model 711 miniature wideband current probe (American Laser systems Inc., CA) and terminated in a 50Ω input impedance at the oscilloscope to provide a 1 mV/mA sensitivity. The light emission from the laser chip was directly coupled to the detector (Tektronix J16/J502 digital photometer) for light-current data. Care was taken to have the detector area to be larger than the incident area for the light at the detector surface. The peak power was then evaluated by scaling the average power with the duty cycle of the pulsed drive current.

3.3.1 Light current characteristic

The light-current curve, a key characteristic for evaluating the efficiency of the laser and also to determine it's operating point and threshold current, is commonly used to provide the power output at the drive level of interest that is applied to the laser. The slope efficiency of the diode can then be derived from the light-current curve, and is most commonly expressed in units of mW/mA.

The peak light output power for several broad area devices (stripe width of 50 μm) with varying cavity length are shown in Fig. 3.3 (cavity length of 865 μm), Fig. 3.4 (cavity length of 400 μm), and Fig. 3.5 (cavity length of 200 μm). The broad area devices can be assumed to have negligible lateral losses. With increasing mirror losses, viz., smaller cavity length, the threshold first reduces (from 300 mA to 240 mA) and subsequently increases to 300 mA for the 200 μm device. Small kinks in the light-current characteristic were seen to appear (Fig. 3.4 and Fig. 3.5). In a typical gain-guided laser such kinks in the light-current characteristic are usually associated with lateral mode shifts in the junction plane, the appearance of higher order lateral modes, or a change from TE to TM polarization or possibly a shift in lasing wavelength with increasing drive level.

In the broad area devices (50 μm) the continued rise in output power at the longer wavelength was accompanied with the appearance of lateral modes of increasing higher order (Fig. 3.6). As shown in Fig. 3.6a&b, at lower currents the device lased in the fundamental and the first lateral order. When lasing emission is detected from the n=2 level (I = 400 mA: Fig. 3.6c) the lateral mode order is already high (4th order) exhibiting an asymmetric intensity profile. At I = 610 mA, higher order modes appeared at 959 nm in addition to lasing from the n=2 level and the barrier (see also Fig. 3.5). The asymmetry of the lateral mode pattern as evident in Fig. 3.6c is already beginning to appear in Fig. 3.6b for the first order mode and is also evident for the 4th order mode in Fig. 3.6d . The presence of the higher order modes, in addition to switching in lasing wavelength, results in the observed kinks in the light-current characteristic.

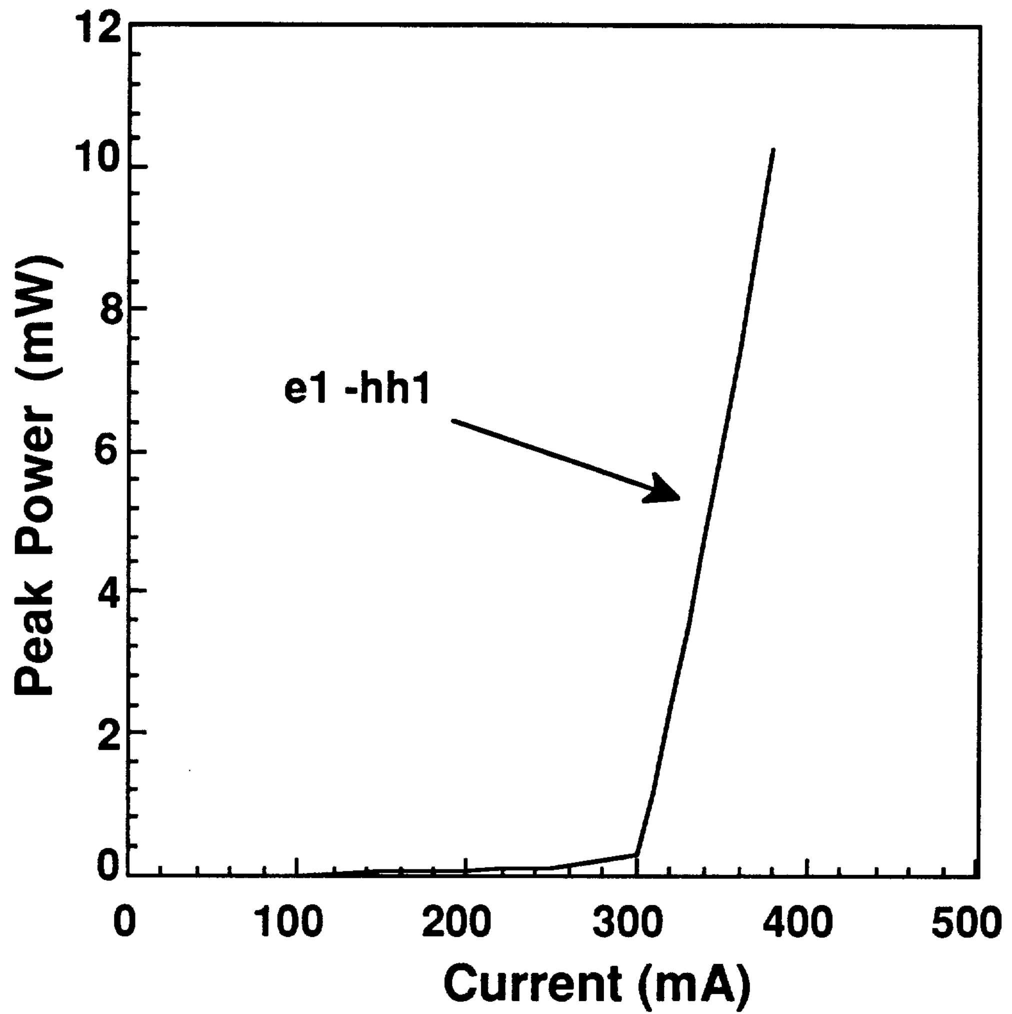

Figure 3.3. The light-current characteristic for 50 μm × 865 μm sample (2A_13) in pulsed operation; arrows indicate the observed transition: n=1 (986 nm)

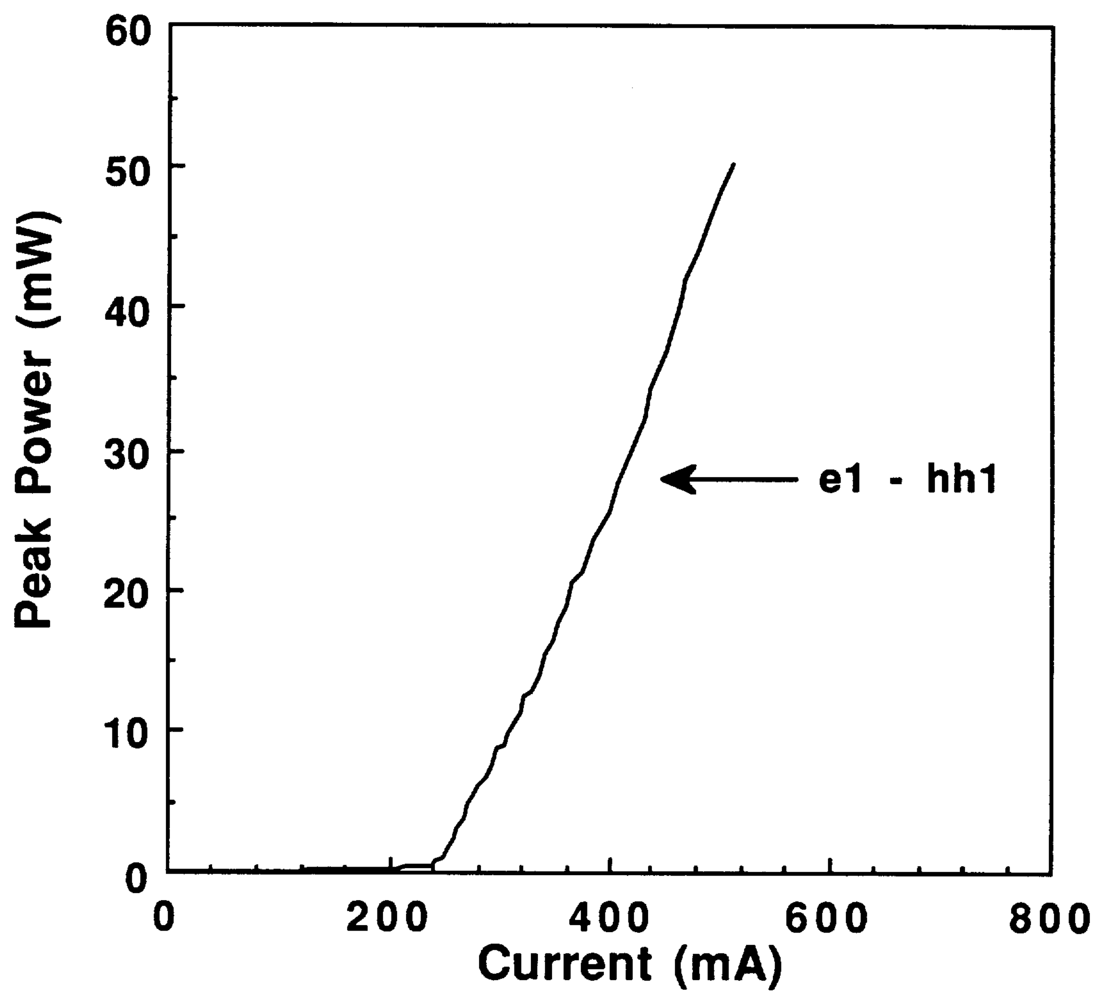

Figure 3.4. The light-current characteristic for 50 μm × 400 μm sample (2B_2) in pulsed operation; arrows indicate the observed transition: n=1 (990 nm)

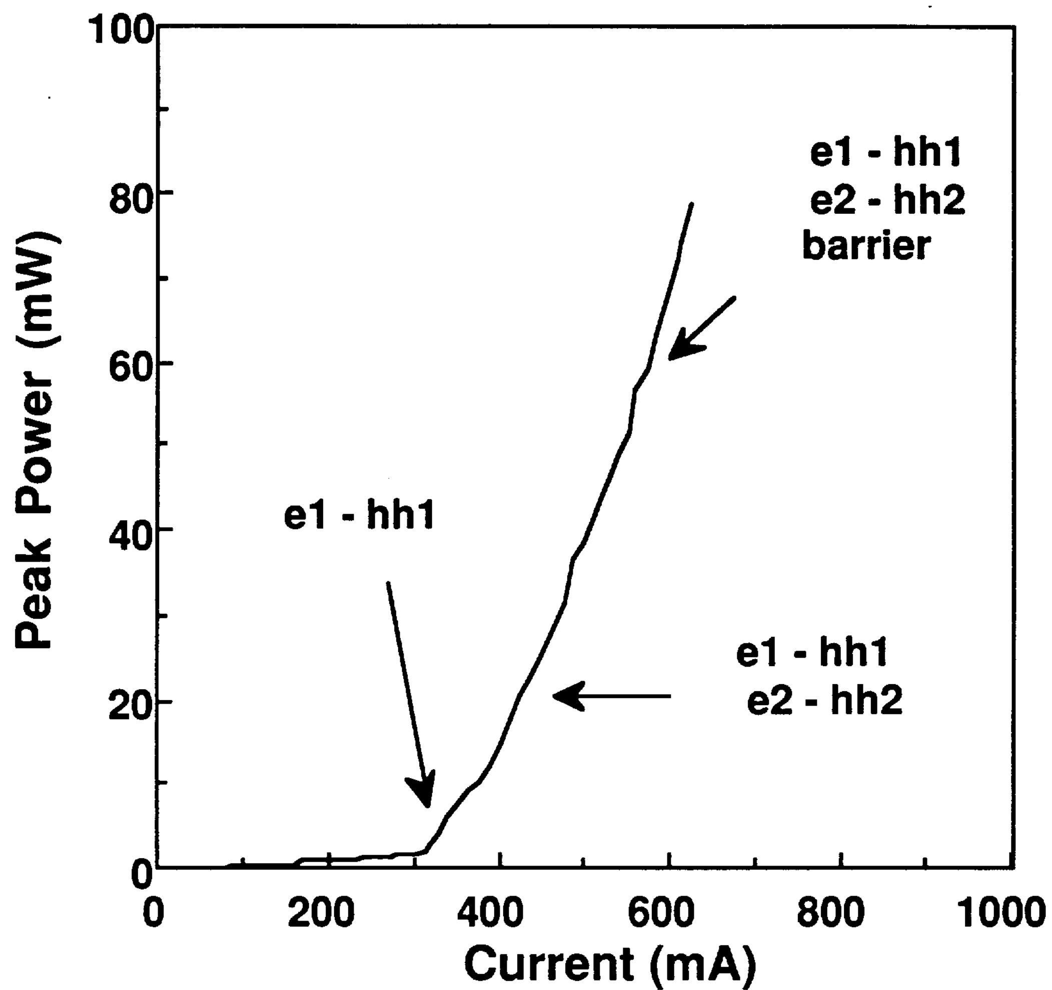

Figure 3.5. The light-current characteristic for 50 μm × 200 μm sample (2B_1) in pulsed operation; arrows indicate observed transitions: n=1 (957 nm), n=2 (913 nm) and barrier (887 nm).

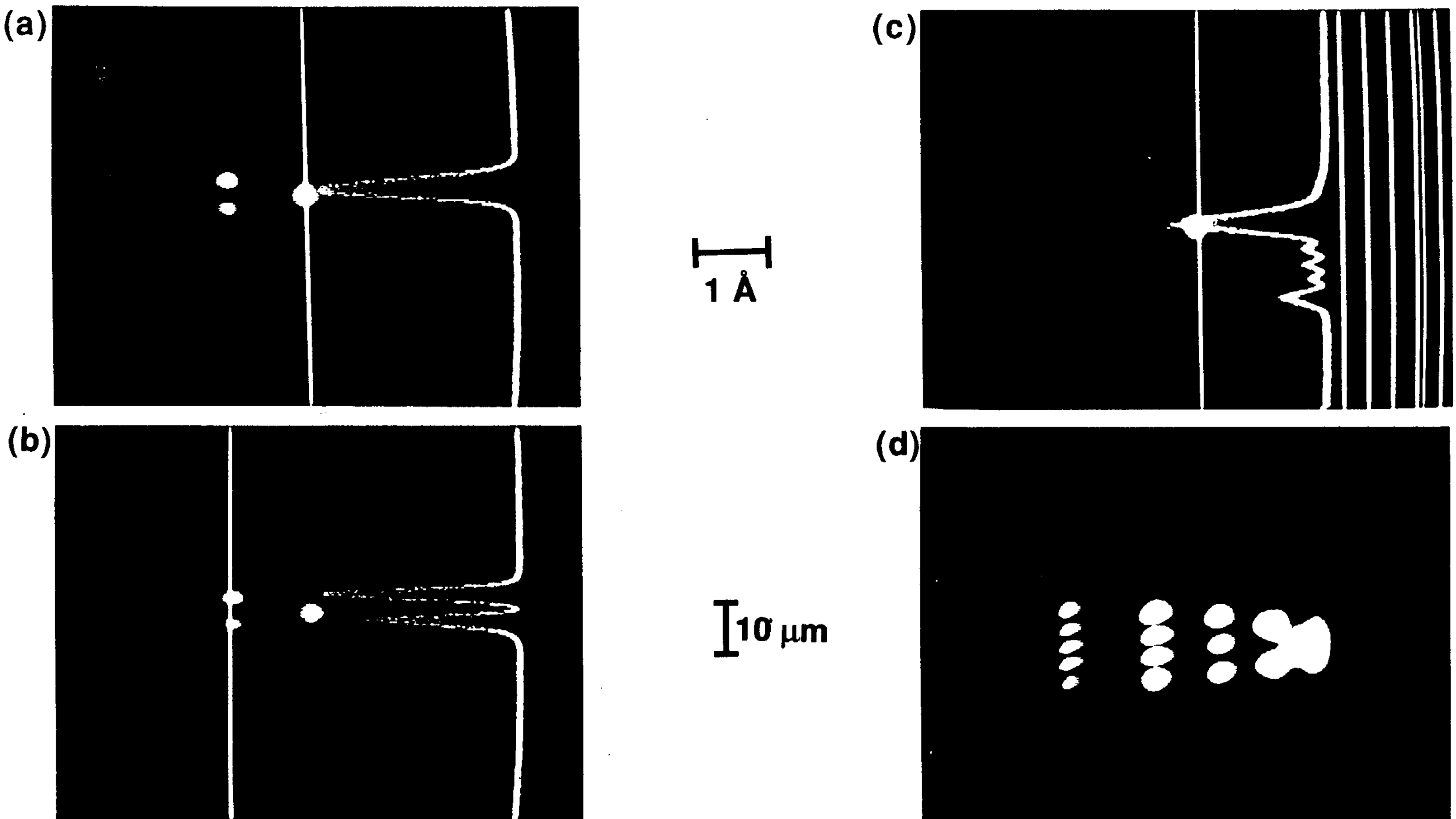

Figure 3.6. Lateral mode structure in 50 μm × 200 μm (2B_1) sample in pulsed operation: (a) & (b) Intensity profile of fundamental and first order modes at 959 nm (n=1) just beyond threshold (I_{th} = 300 mA), (c) Intensity profile of lasing mode at 913 nm for I = 400 mA, and (d) lateral modes (upto 4th order) at 959 nm (n=1) for I = 610 mA.

Two samples with narrower stripe width (15 μm) and a cavity length of 400 μm showed strikingly different behavior in terms of their light-current characteristics, possibly due to different total cavity losses, as seen in Figs. 3.7 and 3.8 . With a smaller stripe width the lateral losses also become important in addition to mirror losses. For the selected cavity length (400 μm) one device showed a pronounced output power saturation and shifts in lasing transitions (Fig. 3.7) while the other (Fig. 3.8) lased only from the barrier transition after threshold but had a pronounced kink with the wavelength of the lasing mode shifting slightly. Whereas such pronounced nonlinearities in the light-current curves were observed for the narrow stripe (15 μm) devices, relatively smaller or no kinks were seen for the broad area device (50 μm) in spite of shifts in lasing towards higher energies with higher mirror loss.

A phenomenon that was widely observed with the narrow stripe devices (15 μm) was the saturation of the optical power for a range of currents with longer cavity devices remaining in saturation for a larger range of currents. Because of the step-like density of states in a quantum well, marked saturation of the optical gain is possible at higher injected carrier densities. With the reduced density of valence states in the strained-layer system the linear gain saturation is further enhanced resulting in output power saturation more easily. In addition, all devices exhibited considerably low values for the slope efficiencies, which is a measure of the change in output power to incremental change in the input drive current level. It is known that "true" gain clamping beyond threshold does not occur since with increase in laser power, other nonlinear mechanisms, such as spectral hole burning, begin to influence the lasing characteristics. This leads to nonlinear

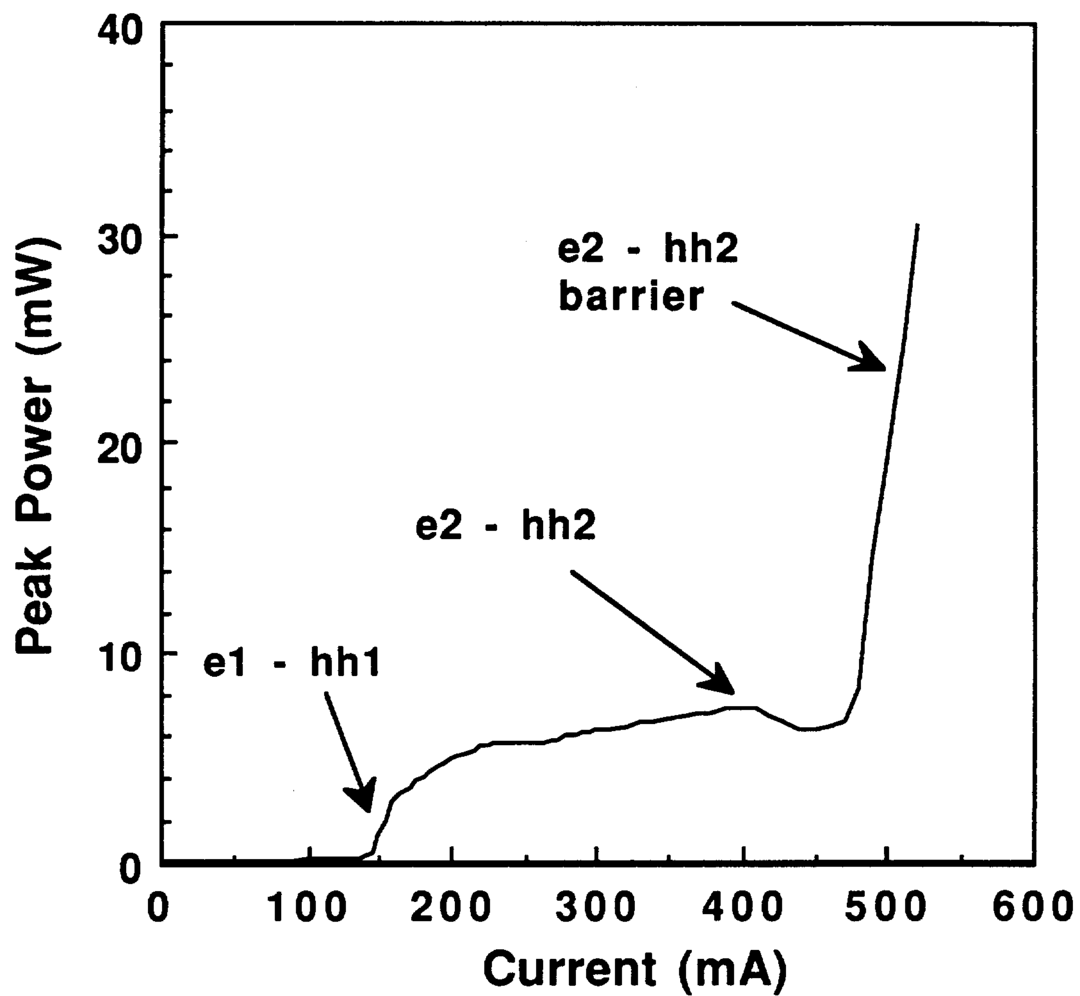

Figure 3.7. The light-current characteristic for 15 μm × 400 μm sample (2A_26) in pulsed operation; arrows indicate the observed transitions; n=1 (975 nm), n=2 (909 nm) and barrier (885 nm).

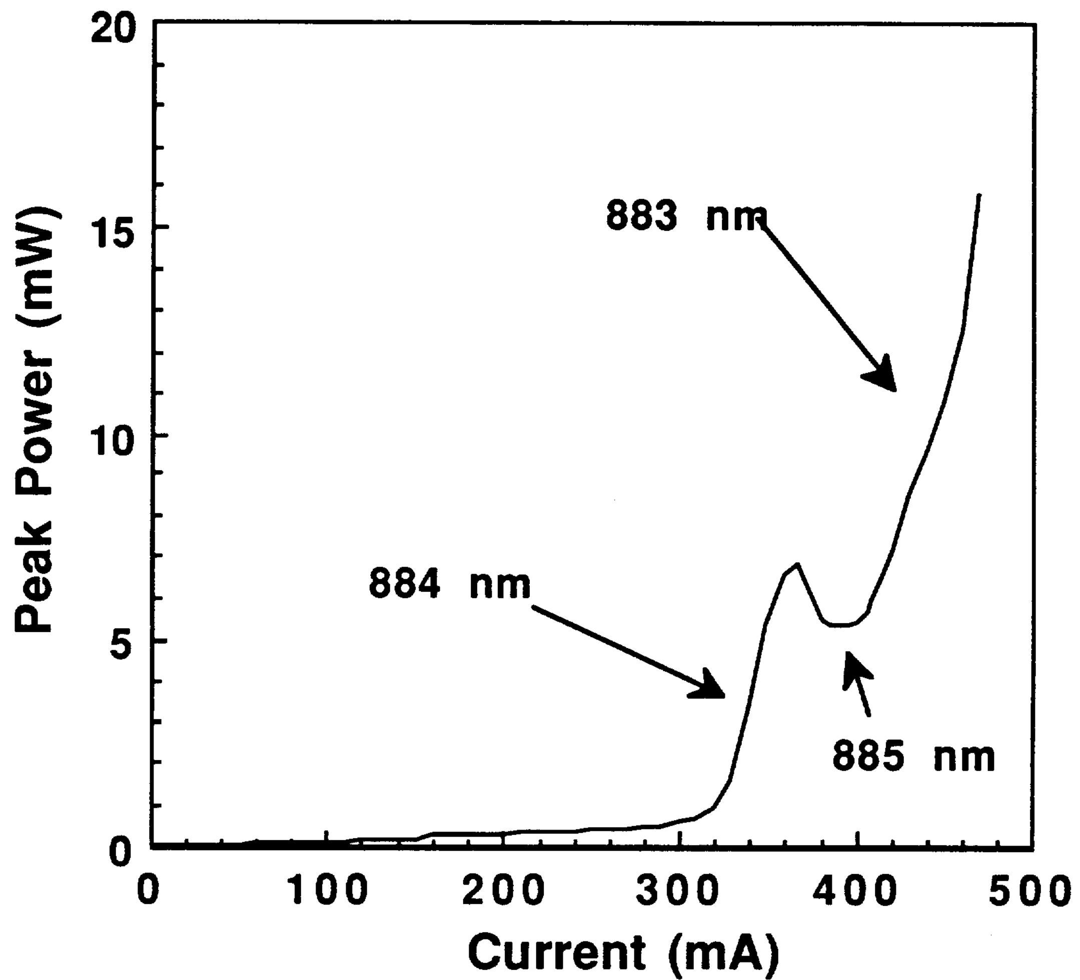

Figure 3.8. The light current characteristic for 15 μm × 400 μm sample (2A_24) in pulsed operation; shown is the small shift in peak lasing wavelength with the device operating in the barrier transition from threshold.

gain compression and the resulting observed lower slope efficiencies and pronounced output power saturation. The slope efficiency sometimes improved when the device operating point crossed the kink/saturation region since at the shorter wavelength (e.g. lasing from the barrier) the nonlinearities do not yet influence the lasing characteristics.

3.3.2 Threshold current

Table 3.1 lists the basic parameters from optical and electrical characteristics measured in detail for a number of device chips. For comparison purposes we normalized threshold current to laser stripe area for obtaining a threshold current density. It should be noted, however, that due to lateral current spreading actual current densities are smaller, particularly for the narrow stripes. Table 3.1a and Table 3.1b consist of results on devices processed on two different pieces but from the same wafer and identified as 2A and 2B.

Considerable variation in the threshold current was observed among the devices tested. It was therefore difficult to come to definite conclusions on the trend due to the fact that the devices lased at substantially different wavelengths. This behavior will be analyzed in more detail in Sec. 3.3.3 .

The threshold currents were found to be rather high, in general. Contributions to the total current (measured) from unavoidable non-radiative and leakage currents are known to possibly result in higher injection current requirements. Such contributions have been explained in the literature via a number of mechanisms[46,49,57] : (1) bulk and interface

Table 3.1a: Characteristic parameters of measured laser samples (Wafer : 2A/1-17-12-90)

Sample	Cavity Dimension W L ($\mu m \times \mu m$)	I_{th} (mA)	$J_{th} = I_{th}/(W\ L)$ (A/cm^2)	Slope efficiency (mW/mA)	Wavelength (nm)
2A_11	50×930	580	1247	0.0753	988
2A_13	50×865	300	693	0.13	986
2A_1	50×575	320	1113	0.257	988
2A_6	50×355	400	2253	0.115	986
2A_34	15×600	245 650 770	2720 7330 8560	245 - 285 mA : 0.2	980 910 885
2A_8	15×575	135 500 625	1565 5797 7246	135-200 mA: 0.236	980 910 887
2A_26	15×400	150 400 475	2500 6670 7920	150-165mA: 0.128 490-520mA: 0.533	975 909 885
2A_24	15×400	315	5250	315-350mA: 0.125	884
2A_5	15×355	230 330	4319 6197	230-260 mA : 0.115 330-350mA : 0.24	914 885
2A_9	15×200	260	8667	0.05	885
2A_4	10×355	230	6478	0.107	885
2A_3	5×355	230	12957	0.259	884

Table 3.1b: Characteristic parameters of measured laser samples (Wafer: 2B/1-17-12-90)

Sample	Cavity Dimension W L (μmxμm)	I_{th} (mA)	$J_{th} = I_{th}/(W\ L)$ (A/cm^2)	Slope efficiency (mW/mA)	Wavelength (nm)
2B_4	50x800	240	600	0.25	990
2B_3	50x600	450	1500	0.11	992
2B_2	50x400	250	1250	0.188	990
2B_1	50x200	300	2500	300-350 mA : 0.155	957
		400	4000	400-500 mA : 0.24	913
		595	5950	600-625 mA : 0.4	887
2B_7	15x200	155	5166	150-160mA: >1	974
		162	5400		911
		189	6333		886

recombination via defect states in the band gap; (2) Auger recombination which include band to band processes, phonon assisted processes and trap assisted processes; (3) carrier loss or spill-over into the adjoining layers, over the top of the quantum well, including the cladding layers resulting in possible recombination from the higher lying conduction band valleys. Since the recombination in the first mechanism is mostly indirect, the carriers have longer lifetimes and thus contributions to the total current would be small in spite of the larger density of states. However, with a potential step of only ≈ 150 meV (at 300 °K and using a 60:40 band offset) for the Γ levels at the cladding/guide interface (with only 20% Al concentration in the AlGaAs layer : see Fig. 3.1), direct recombination from the cladding cannot be ruled out and hence can become a dominant contribution with increasing leakage of carriers from the active layer to the surrounding barrier/cladding regions. The lower potential step could also result in large leakage as a result of a combination of the relatively large spill-over volume for the cladding layers and the carrier sinks located at the ohmic contacts to the claddings[68]. The third mechanism involving the occupancy of higher energy levels is thus more probable as the quasi-Fermi levels are pushed higher with increasing drive level.

Considering the general expression for the threshold current density, J_{th} (A/cm^2), in the low current range where the gain can still be related to the current density with a linear relationship, { $g = \beta (J_n - J_1)$ where β is the nominal gain coefficient (cm^2/A), J_1 is the transparency current density and the nominal current density is given as $J_n = (J \eta_i / d)$, η_i the internal quantum efficiency and d is the active layer thickness, $d = L_z$ for quantum well }, we have[69]

$$J_{th} = \frac{J_o}{\eta_i} + \frac{d}{\Gamma}\left\{\left(\frac{1}{\eta_i \beta}\right)\left[\frac{1}{L}\ln\frac{1}{R} + \alpha_i\right]\right\} \tag{3.1}$$

where J_o is the radiative current density (A/cm^2) for transparency, L is the cavity length, R the facet reflectivity and α_i the internal optical loss (cm^{-1}) including the lateral loss. It is evident that apart from the internal efficiency, η_i, which is a measure of the fraction of the injected carriers that is useful for generating photons through radiative recombination, the internal loss, α_i, which includes the lateral loss, and the mirror loss, determined by the cavity length and facet reflectivity, are the other components that determine the threshold of a laser. The nonradiative mechanisms (first two mechanisms : recombination at defects and Auger), when present, can be expected to deteriorate the internal quantum efficiency in the lasing mode thus increasing threshold. Higher optical losses (mirror or lateral) translates to higher thresholds thus leading to pronounced bandfilling, including carrier spill-over (third mechanism : carrier leakage), for increasing carrier injection levels and consequently a shift in the laser transition energy from the lowest energy bound state of the quantum well to higher subbands or even to the energy levels in the barrier. It is thus possible to use α_i and L to control the optical losses in the cavity and hence J_{th}, given that the facets are uncoated. It is important to note that with the shifts in lasing wavelength, J_o, α_i, η_i, and β are strictly not constant with current. β actually changes abruptly when wavelength switches from the n=1 to the n=2 and to the barrier. Optical mode size, d/Γ, however, should not change much.

In Table 3.1, in addition to the initial or "ordinary" lasing threshold,

"higher-order" thresholds where the switching to shorter wavelength occurs, as well as the respective lasing wavelengths are listed. Note that these "higher-order" thresholds are only indicative of the onset of the particular transition in question when observed on the CCD camera (for description of set up see p. 53) and do not constitute a "true" threshold as is implied for the initial threshold.

3.3.3 Internal loss and quantum efficiency

With substantially high thresholds and low slope efficiencies observed for the devices (see Table 3.1), it is important to estimate the internal optical loss, α_i, and the stimulated internal quantum efficiency, $\eta_{i,st}$, which is the fraction of injected carriers converted into photons. The internal loss can be related to the external differential quantum efficiency, η_e, as[54]

$$\eta_e = \eta_{i,st} \frac{\alpha_m}{(\alpha_m + \alpha_i)} \tag{3.2}$$

where α_m is the mirror facet loss per unit length given by

$$\alpha_m = \frac{1}{2L} \ln \left(\frac{1}{R_1 R_2} \right) \tag{3.3}$$

where R_1 and R_2 are the facet reflectivities at the two ends and L is the length of the laser. The values of $\eta_{i,st}$ and α_i can be evaluated from the relationship between the measured slope of the light current characteristic and the mirror

loss for various cavity lengths. The external quantum efficiency, η_e, is directly proportional to the slope dP_{out}/dI of the light-current characteristic[54],

$$\eta_e = \frac{q}{2h\nu}\frac{dP_{out}}{dI} \tag{3.4}$$

where $h\nu$ is the photon energy and the factor (1/2) accounts for the power emitted by only the front facet with equal facet reflectivities, $R_1 = R_2$. [**Note :** in Reference 54, equation 2.6.12, pp. 57, should not contain $\eta_{i,st}$. The correct equation is obtained by noting that equation 2.6.8, pp. 56, from which equation 2.6.12 is derived, has to include $\eta_{i,st}$ to account for the fraction of carriers converted into photons]. Rewriting equation (3.2) we get,

$$\frac{1}{\eta_e} = \frac{1}{\alpha_m}\left(\frac{\alpha_i}{(\eta_{i,st})}\right) + \frac{1}{(\eta_{i,st})} \tag{3.5}$$

where by plotting $1/\eta_e$ against $1/\alpha_m$ gives $\eta_{i,st}$ from the Y-axis intercept and α_i from the slope of a linear fit of the data. Fig. 3.9 shows such a plot for the broad area (50 μm) devices (see Table 3.1a and 3.1b) where the straight line shown is a linear fit. The scatter in the data is an indication of the nonuniformity in the wafer from which these devices were fabricated. From the Y-axis intercept, $\eta_{i,st}$ is found to be 31% and from the slope, α_i to be 8.9 cm^{-1} . The low value for internal stimulated efficiency confirms our earlier speculation on excessive nonradiative recombination mechanisms and/or carrier leakage out of the active layer for the observed higher threshold currents for lasing.

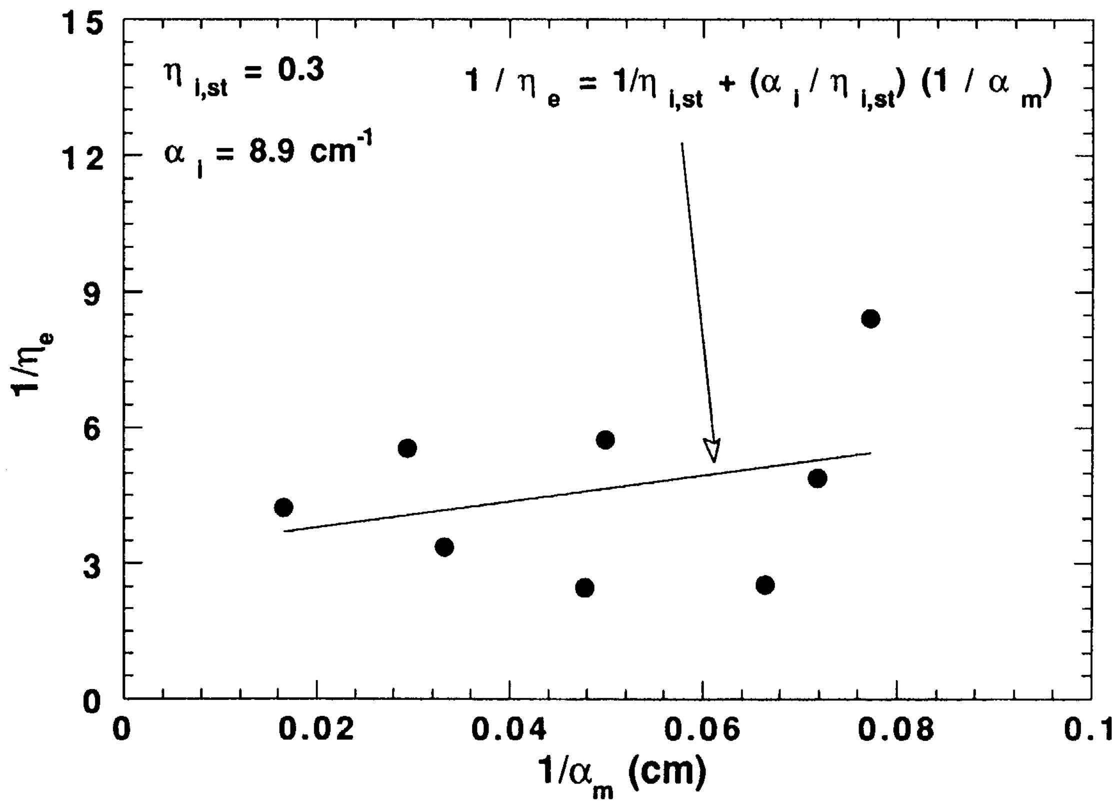

Figure 3.9. Estimation of the internal loss and the internal quantum efficiency from the relationship between the external differential efficiency and the mirror loss. The linear relationship used to fit the data is indicated with an arrow.

3.3.4 Wavelength shifts in the emission spectrum

Fig. 3.10 shows the measured dependence of the threshold current density as a function of the cavity length for broad area devices (stripe width = 50 µm). For most cavity lengths studied, lasing was found to occur at the n=1 transition, corresponding to the e1-hh1 transition, due to insignificant lateral losses. At cavity lengths below 600 µm the expected short cavity effect of increasing threshold current as a direct consequence of the gain saturation at high injection for thin single quantum well structures[14,70] was observed. However, at the shortest cavity length of 200 µm, we noticed that lasing started at a somewhat shorter wavelength of about 958 nm (blue-shifted e1 - hh1[33]), and with increased drive level, the device also operated at higher energy levels corresponding to the n=2 transition of 913 nm (e2 - hh2) and the barrier transition of 885 nm. This is attributed to the increase in the mirror loss which forces more carriers to be pumped into the second quantum level and eventually to the barrier, due to poor confinement in the quantum well. Fig. 3.11 plots the light-current curve for this device (Fig. 3.5 is repeated in Fig. 3.11a) and its wavelength of operation as a function of the drive current (Fig. 3.11b). In the present device, in addition to the onset of higher order lateral modes at the longer wavelength of 958 nm (n=1) (see for example Fig. 3.6), the shift of the lasing wavelength to higher energy levels with increasing drive level resulting in the observed kinks in the light output characteristic (Fig. 3.11b). Wavelength separations were as wide as 70 nm (97 meV) for n=1 (≈ 980 nm) to n=2 (≈ 910 nm) and about 25 nm (38 meV) for n=2 to barrier (≈ 885 nm). Lasing wavelengths for various drive levels were observed by imaging

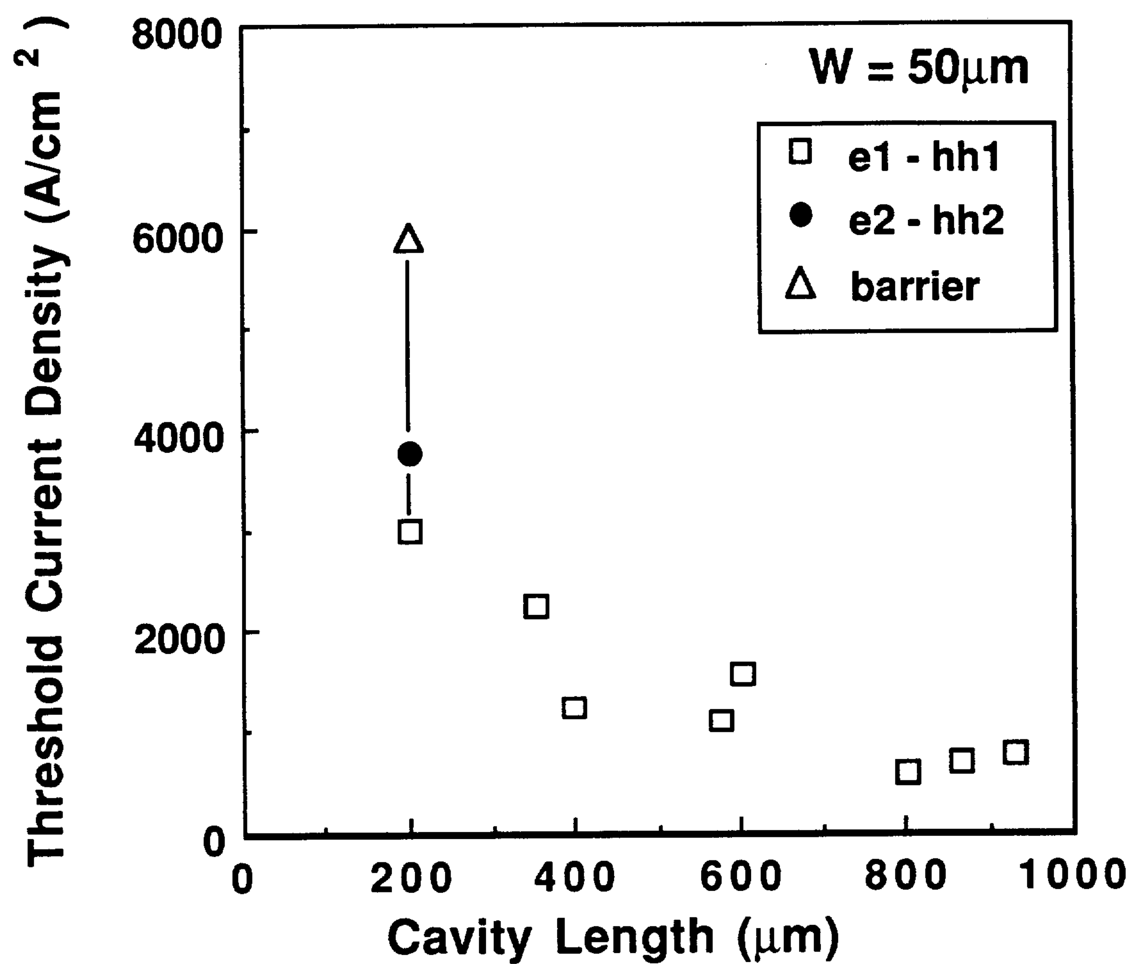

Figure 3.10. Cavity length dependence of threshold current density for broad area (50 µm) stripe devices. Note that for the shortest cavity length (200 µm) additional transitions are indicated with vertical lines.

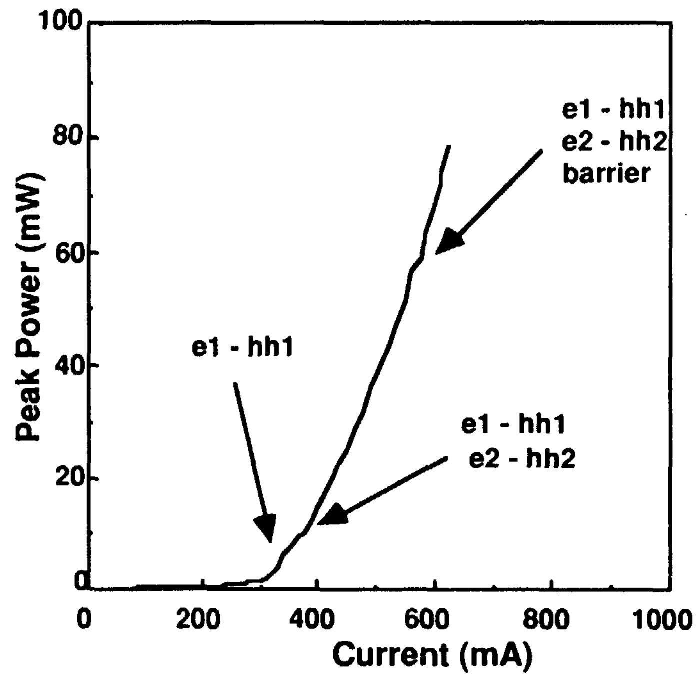

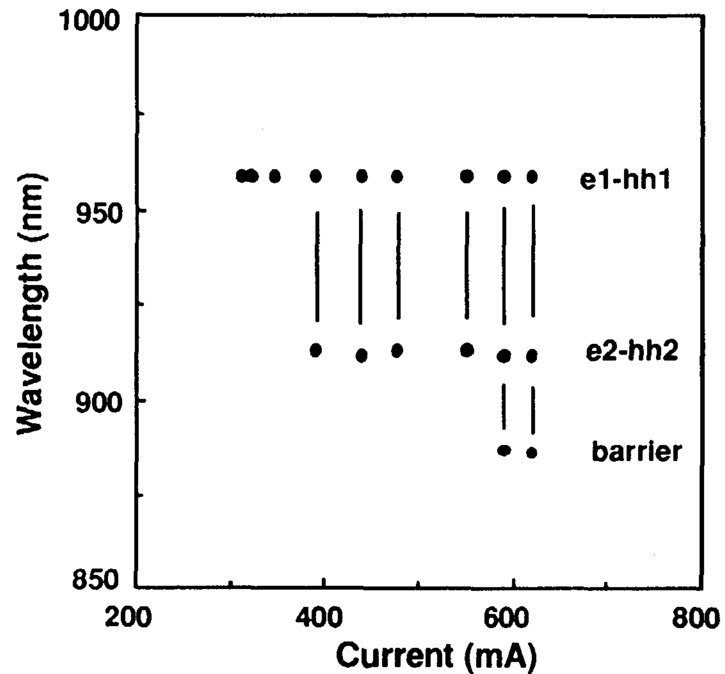

Figure 3.11. (a) The light-current characteristic and (b) the shift in lasing wavelength with drive current for 50 μm x 200 μm (2B_1 in Table 3.1b) sample in pulsed operation; the observed transitions are indicated : n=1 (953 nm), n=2 (913 nm) and barrier (885 nm) and simultaneous transitions are indicated by vertical lines.

the light output into a SPEX (Model 1704) 1-m grating spectrometer and a CCD camera (see section 3.4). The wavelengths of operation were identified by the strong intensity mode at the wavelength range of interest corresponding to the available transitions in the quantum well or the barrier. Note also that in Fig 3.10b vertical lines are used to indicate "simultaneous" lasing in different wavelengths at the same drive level. It is necessary to realize that such an observation is in a "time-integrated" sense and a true picture can be obtained by investigating the temporal behavior at these drive levels.

Devices with a 15 μm stripe width (Fig. 3.12) more consistently exhibited a shift of the operating wavelength with increased drive level at any cavity length tested. In the case of a longer device (575 μm or 600 μm), when increasing drive level, switching was observed from 980 nm (e1 - hh1) to 910 nm (e2 - hh2) and eventually, to 887 nm (the barrier transition). At 400 μm one device with a lower threshold began lasing at the n=1 level and shifted to the shorter wavelengths while another lased exclusively from the barrier (see Fig. 3.7). For a shorter device (355 μm) lasing occurred initially at 910 nm (e2-hh2) and subsequently switched to 885 nm (the barrier transition) at higher drive levels (also see Fig 3.13). Decreasing the cavity length, for the shortest device tested (200 μm) results were mixed: one device, with a high threshold, lased at the barrier wavelength only; another with a substantially lower threshold (indicating a lower internal loss, α_i), showed wavelength switching like the longer devices.

Considering the stripe width dependence of threshold in Fig. 3.13 for one particular cavity length (355 μm) a shift from e1 - hh1 to the barrier transition is observed when the stripe width is reduced from 50 μm to 10 μm.

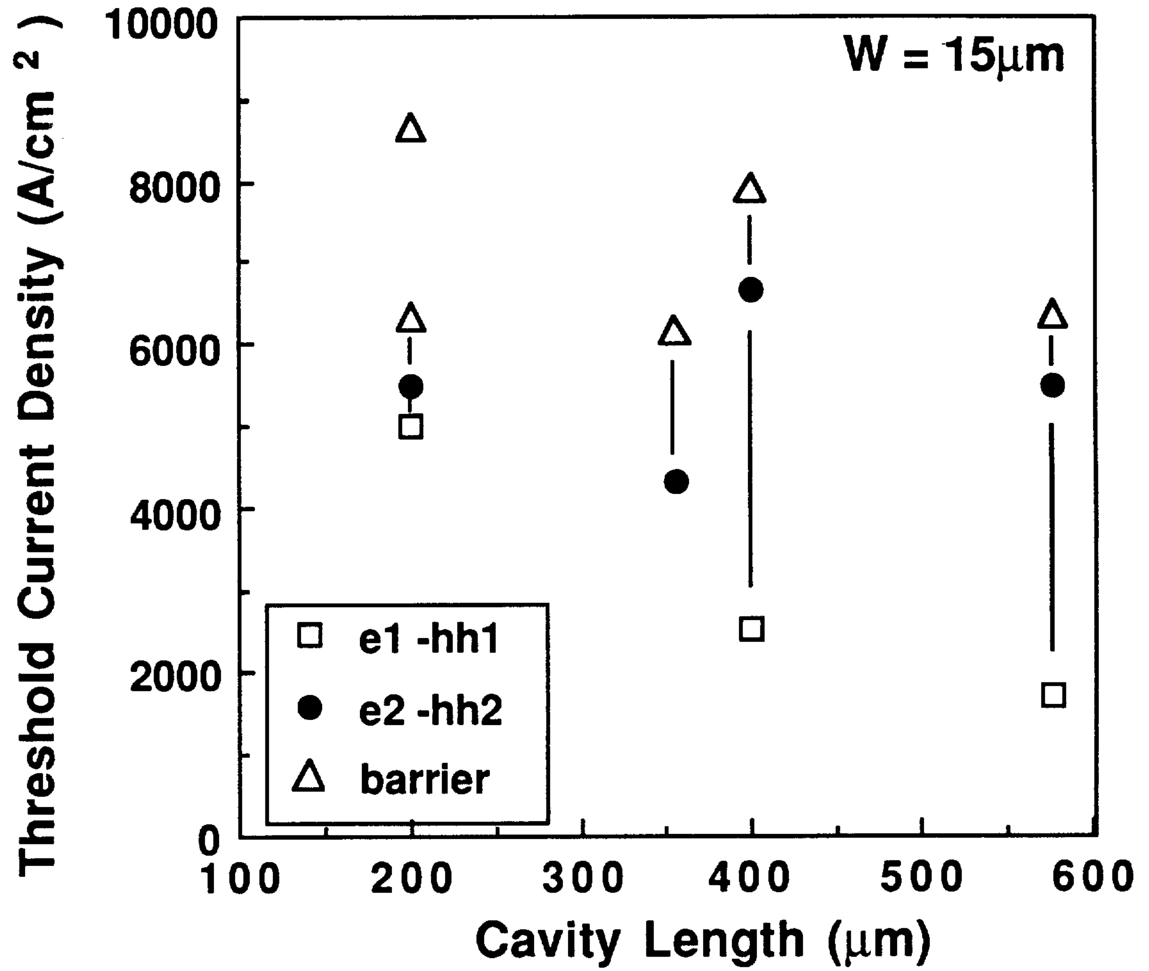

Figure 3.12. Cavity length dependence of threshold current density for narrow stripe (15 μm) devices. Available transitions in each device are shown connected with vertical lines.

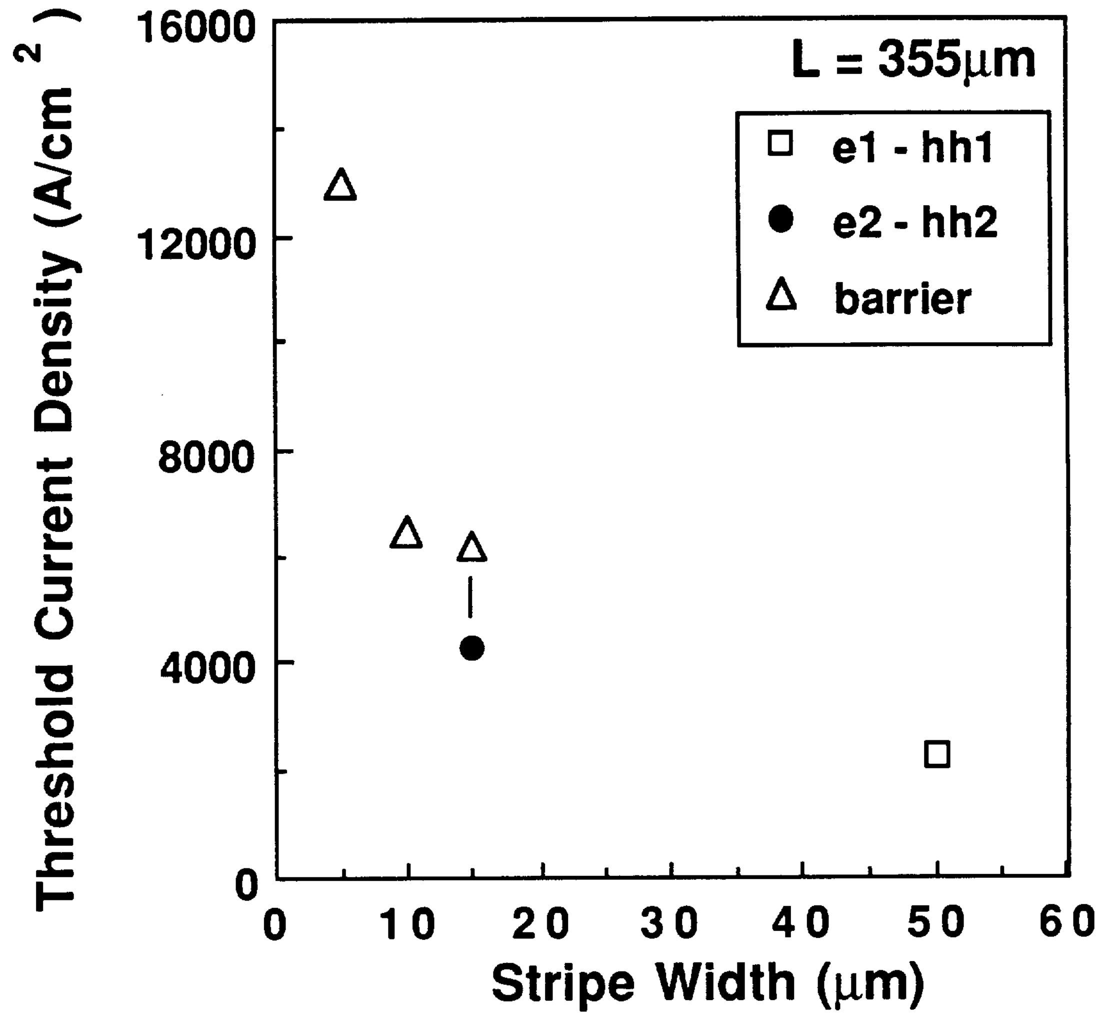

Figure 3.13. Stripe width dependence of threshold current density for devices with cavity length of 355 μm. Vertical line indicates one device with two available transitions.

At an intermediate 15 μm stripe width the additionally available e2 - hh2 transition appears, before the device switches finally to the shorter barrier wavelength at higher drive currents. The corresponding light output and lasing wavelengths as a function of the drive level for the 575 μm and 355 μm long lasers are indicated in Fig 3.14 and 3.15, respectively. The data clearly demonstrate the realization of discrete switching between two lasing wavelengths usually connected with severe non-linearities in the light-current characteristic as shown in Fig 3.14a and Fig. 3.15a. Once again, the vertical lines in Fig 3.14b and 3.15b indicate "simultaneous" lasing at two different wavelengths at the same drive level.

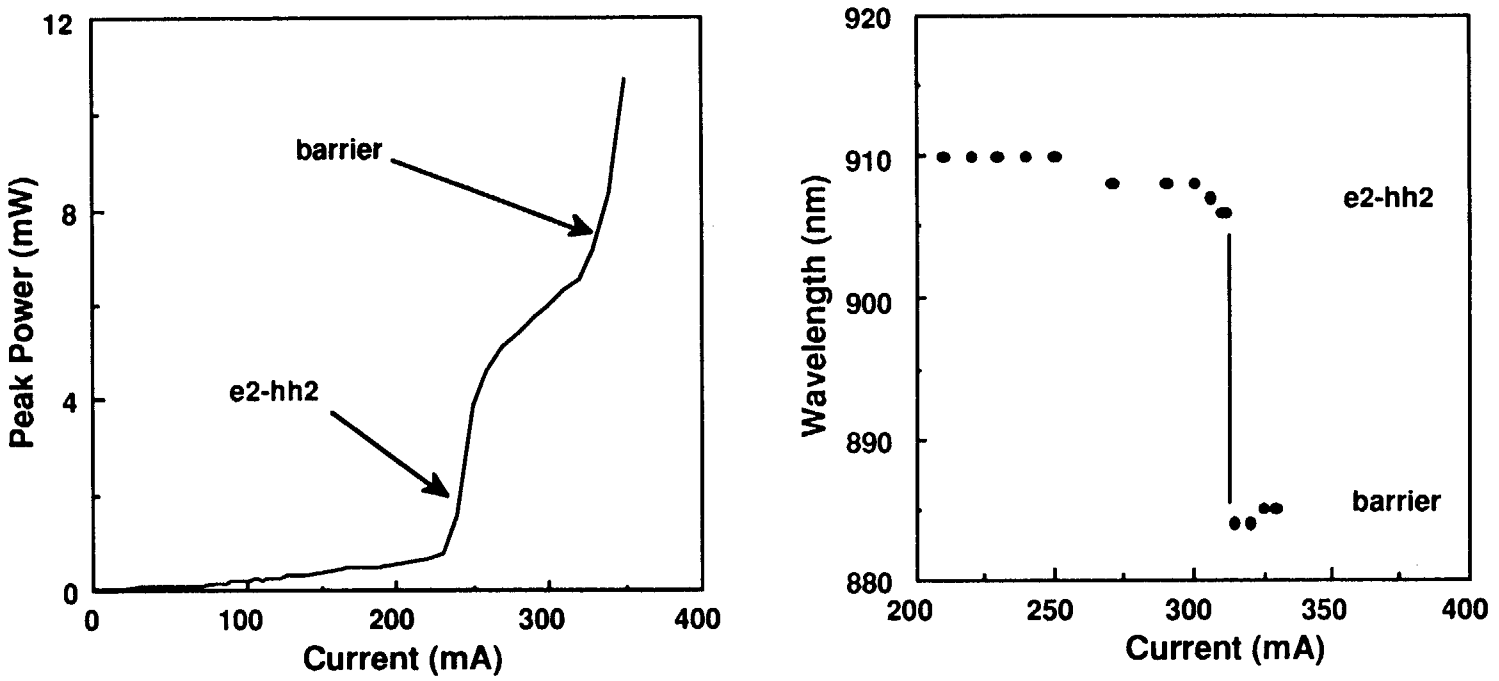

Figure 3.14. (a) The light-current characteristic and (b) the shift in lasing wavelength with drive current for 15 μm x 355 μm (2A_5 in Table 3.1a) sample in pulsed operation; the observed transitions are indicated : n=2 (910 nm) and barrier (885 nm) and simultaneous transition is indicated by a vertical line.

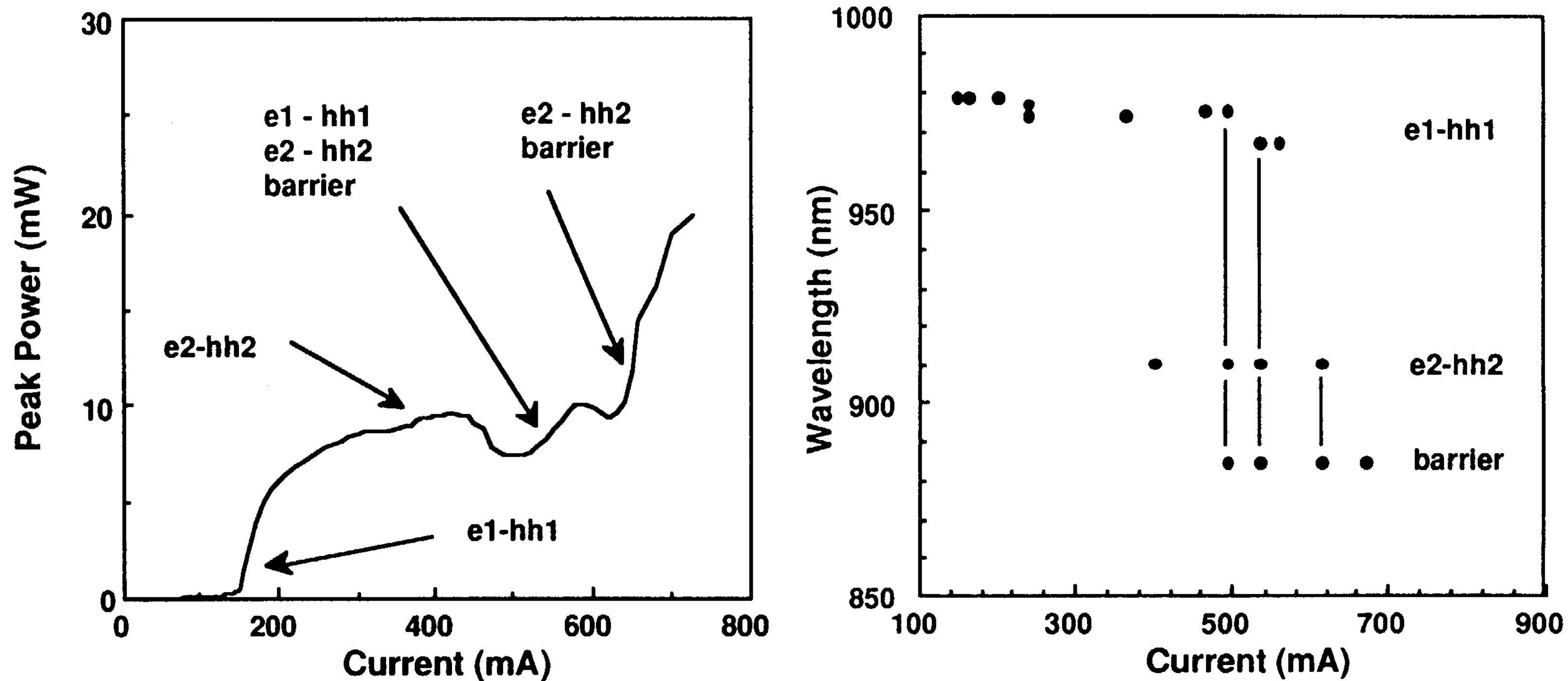

Figure 3.15. (a) The light-current characteristic and (b) the shift in lasing wavelength with drive current for 15 μm x 575 μm (2A_8 in Table 3.1a) sample in pulsed operation; the observed transitions are indicated : n=1 (980 nm), n=2 (910 nm) and barrier (887 nm) and simultaneous transition are indicated by vertical lines.

3.4 Spectral characteristics of wavelength switching devices

3.4.1 Experimental set up

Time-averaged spectra were measured, for lasers that exhibited wavelength shifts as a function of drive current, using the experimental set-up shown in Fig 3.16 . The temperature stabilized laser chip was pumped with the digital (HP8112A ; low drive currents) or the analog (HP214B ; high drive currents) pulse source. The near field was imaged on to the entrance slit of a SPEX 1m grating spectrometer (Model 1704) using a 40X (N.A. of 0.85) microscope objective. The exit port of the spectrometer had an adjustable mirror which could be used to deflect the beam to one of the two available ports. One port was used to image the spectrum on to a Tektronix C1002 video camera with its front lens removed to directly access the CCD detector and it's output signal was viewed on a standard 12 inch monitor. The other port was fixed with a liquid nitrogen cooled Photomultiplier (Products for Research). The temperature of the photomultiplier tube was maintained at -90 °C using a feedback loop consisting of a temperature controller (Products for research) and a control solenoid valve to regulate the flow of air into a 20 l liquid nitrogen dewar to force liquid nitrogen out of the dewar into the photomultiplier housing during ON cycles of the solenoid.

The photomultiplier was maintained at an optimum operating voltage of about -1100 V (Maximum 1500 V) applied at the cathode of the photomultiplier with the positive terminal of the power supply (HP6516A) grounded. The detected signal from the anode was fed into a gated integrator

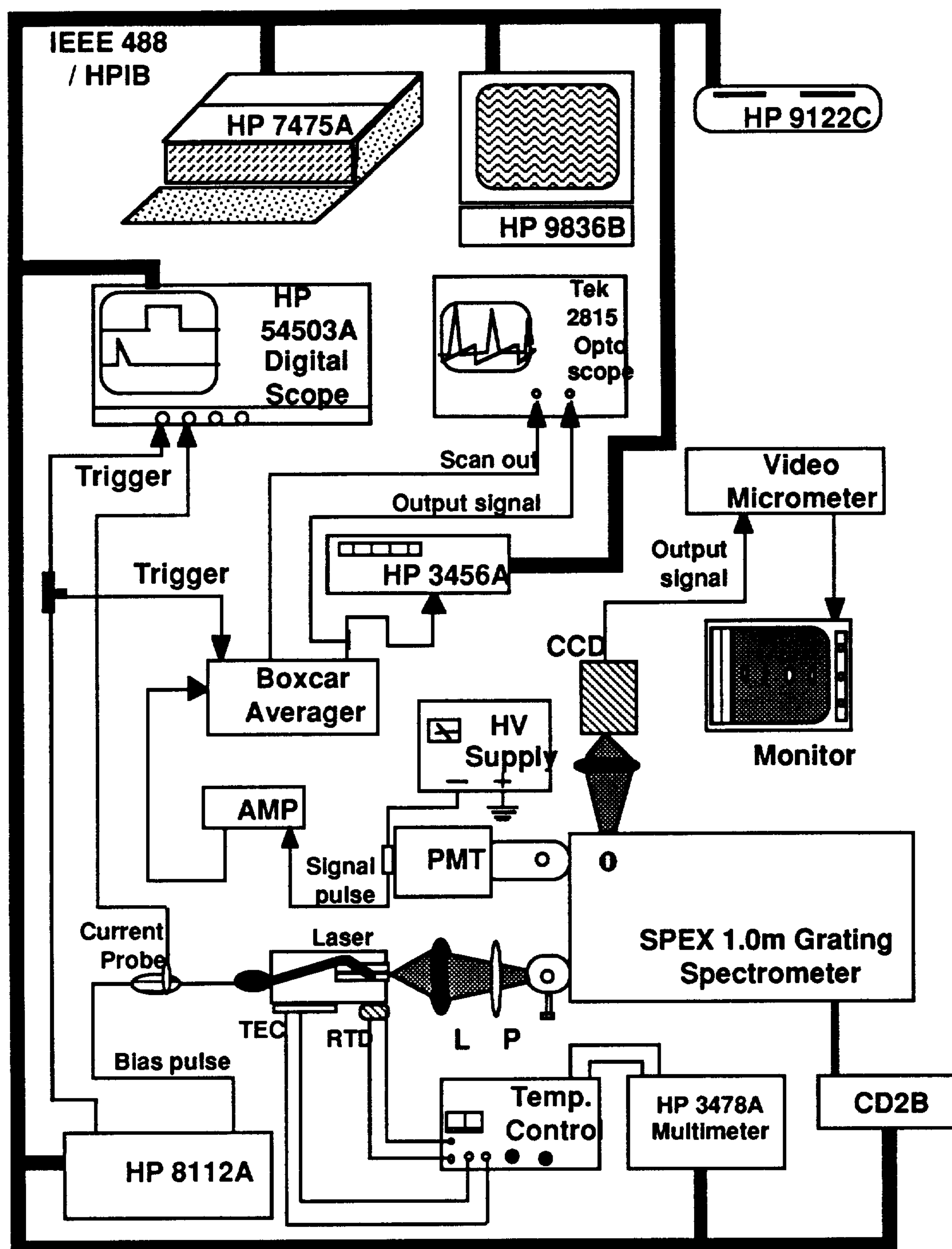

Figure 3.16 Computer controlled experimental set up for time-averaged spectrally resolved near field measurements: TEC-thermoelectric cooler, PMT-photomultiplier tube, RTD-thermistor, CCD-charge coupled device.

(EG&G Model 165) which was mounted in the boxcar averager (EG&G Model 162). The trigger signal from the pulse source was fed to the boxcar for timing control to properly position the gate for sampling the input signal. The current pulse monitored with a current probe close to the laser chip and the gate pulse of the boxcar (using the gate output) were observed using the HP54503A 4-channel 500 MHz digitizing oscilloscope. Adjusting the delay between the trigger and the current pulse and proper positioning of the sampling gate at the boxcar, using the "aperture delay" adjustment knobs, were done to sample the signal pulse at the required position (in time). This was necessary to compensate for internal delays in the current source between the trigger and the pulse, the "line" delay of propagation through the electrical cables, and the internal delay in triggering the gate of the boxcar. The DC (direct current) signal output of the boxcar, which is proportional to the input signal amplitude in the sampled region, is then connected to a digital voltmeter (HP 3456A) to digitize the analog signal. For observation of the input signal pulse fed into the boxcar, the analog signal output from the boxcar can be sent to an analog scope (TEK 2815 50MHZ) along with the scan signal provided by the boxcar and triggered externally from the current pulse source. With a narrow gate (≈ 5ns) and a suitable scantime (≈ 0.01 or 0.1s), the light pulse shape as detected by the photomultiplier, though limited by it's response time, can thus be obtained and is useful for preliminary adjustments of the gate position and maximizing the detected signal.

A HP 9000 series 200 computer HP9836B (now updated to series 300) was used to control and acquire data from the different instruments with the IEEE488 or RS232 interfaces: (i) spectrometer through the Compudrive (CD2B)

for controlling the grating position i.e., wavelength, (ii) injection current level adjusted by changing the output of HP 8112A after comparing the measured current with the required current value, (iii) signal output of the boxcar digitized using the digital voltmeter (HP 3456A), (iv) digitizing oscilloscope (HP 54503A) for current amplitude and if necessary, the gate position, (v) data storage using a flexible disk drive (HP9122C) or hard drive (HP9153C), (vi) plotting of acquired data using a plotter (HP 7475A) and (vii) monitoring temperature of the laser mount using a multimeter (HP 3478A) which is used to digitize the analog signal output (proportional to the voltage produced at the RTD element) of the temperature controller (OMEGA Model series 3N10 -P2 ; see also appendix B).

3.4.2 Devices

For purposes of investigating the spectral content as a function of the drive current and to observe the switching of lasing wavelength, devices that consistently showed such behavior were used. The devices reported in this section were hence chosen to be 15 μm stripe widths. The cavity lengths were chosen to be 355 μm (sample 2A_5 in Table 3.1a) and 575 μm (sample 2A_8 in Table 3.1a) to observe the shift from the n=2 to the barrier and the n=1 to the barrier, respectively. We had earlier presented the light current curves along with the lasing wavelength shifts at different drive levels for these two devices (Figs 3.14(a,b) & 3.15(a,b)), respectively.

3.4.3 Measurements

3.4.3.1. The 15 μm × 355 μm Device

Fig 3.17 shows the region of measurement of the 15 μm × 355 μm device, indicated by the two vertical lines, in the light current characteristic. The spectra were measured at various points below and beyond the first threshold (230 mA) into the kink region till *just beyond the second threshold* (325 mA). Spectra measured at three currents after the first threshold, i.e., 236 mA, 302 mA and 330 mA are shown in Figs. 3.18a, 3.19a and 3.20a . At the lower current the device is seen to lase at around 911 nm corresponding to the n=2 transition and switches to the barrier transition around 884 nm at the higher drive level of 330 mA. The modal net gain, G (G_i internal mode gain, α_i internal loss, R facet reflectivity), was obtained from the depth of modulation in the emission intensity using the relation[71]

$$GL = (G_i - \alpha_i L) + \ln(R) = \ln\left(\frac{r^{1/2} - 1}{r^{1/2} + 1}\right) \quad (3.1)$$

where $r = P_{max}/P_{min}$; P_{max} and P_{min} being the intensities at each adjacent peak and valley in the emission spectra, respectively. Note that this relation is true for current levels below threshold of a laser when the device is not lasing. However, beyond the "first" threshold (≈ 236 mA) the laser clearly begins to have a steeper increase in light output indicative of onset of lasing. But beyond 260 mA the device enters into a saturation region for the power output and has a transition from n=2 (e2-hh2) to the barrier wavelength. In this regime, the device could be considered to be in a super-radiance mode with no "true" lasing thus enabling the use of the above relation to evaluate

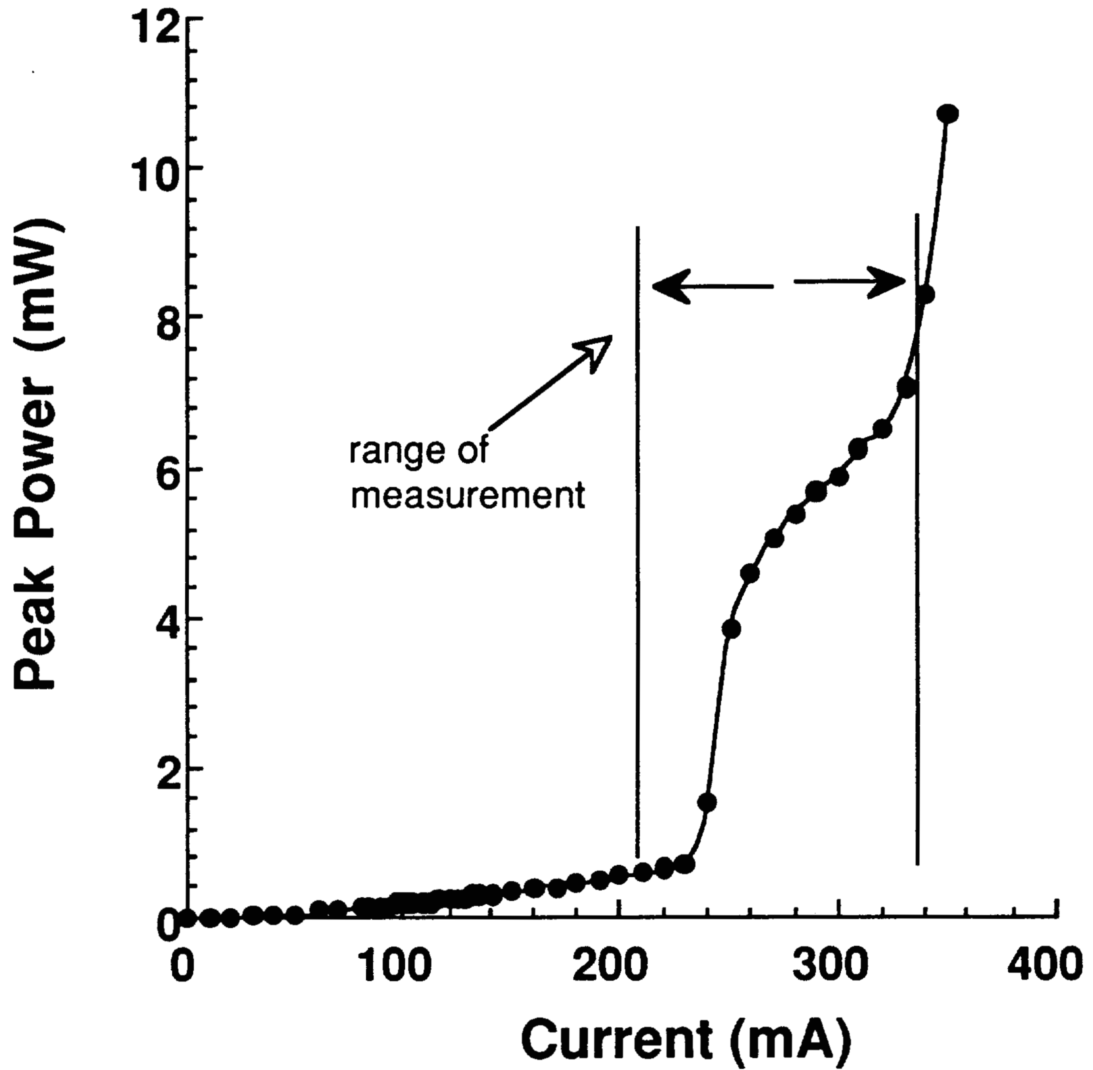

Figure 3.17 Range of measurement, as indicated in the light-current curve, chosen for spectral measurements on 15 μm × 355 μm device.

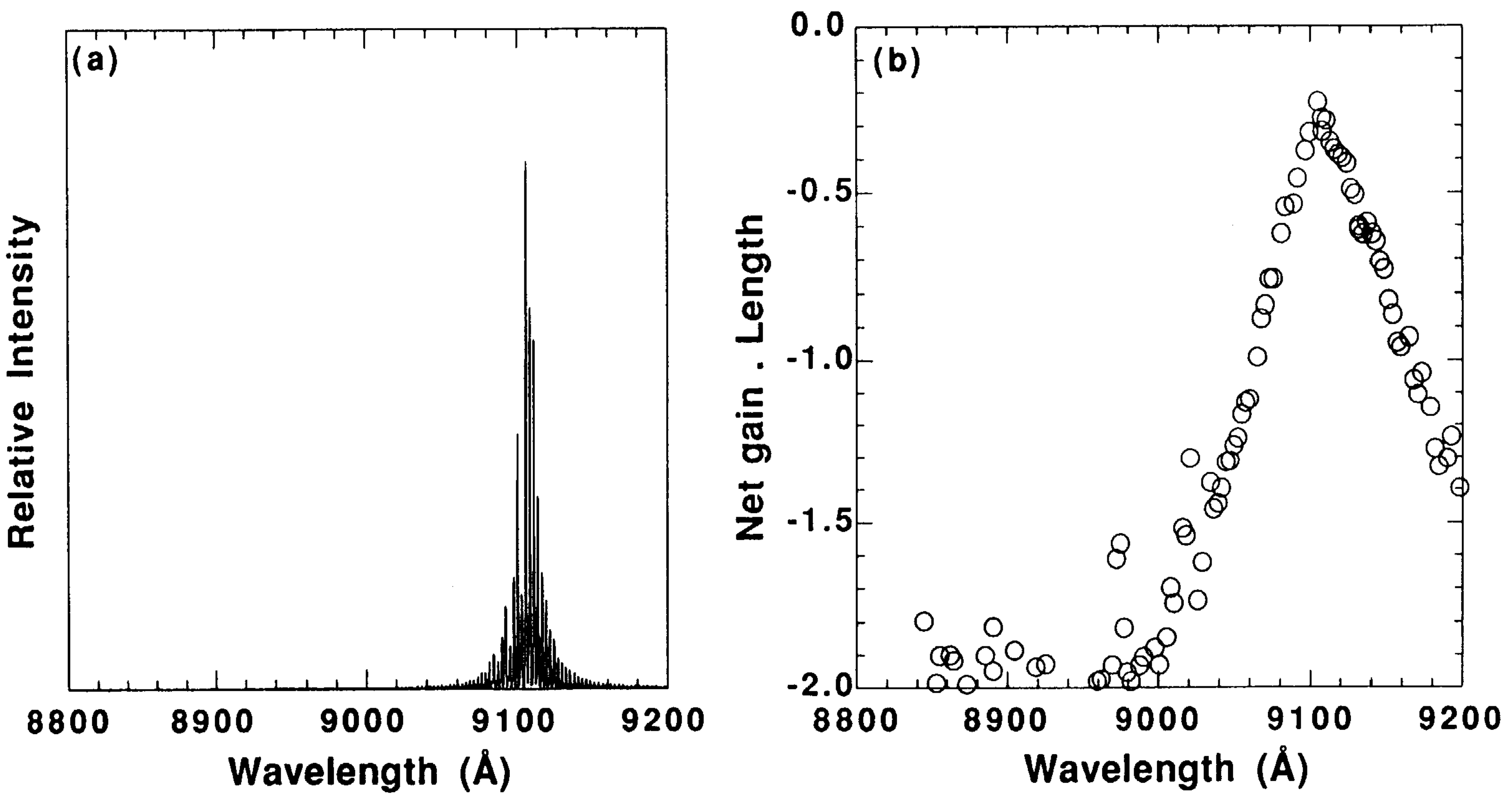

Figure 3.18. (a) Intensity spectrum and (b) (netgain.length) at I = 236 mA for 15 μm x 355 μm.

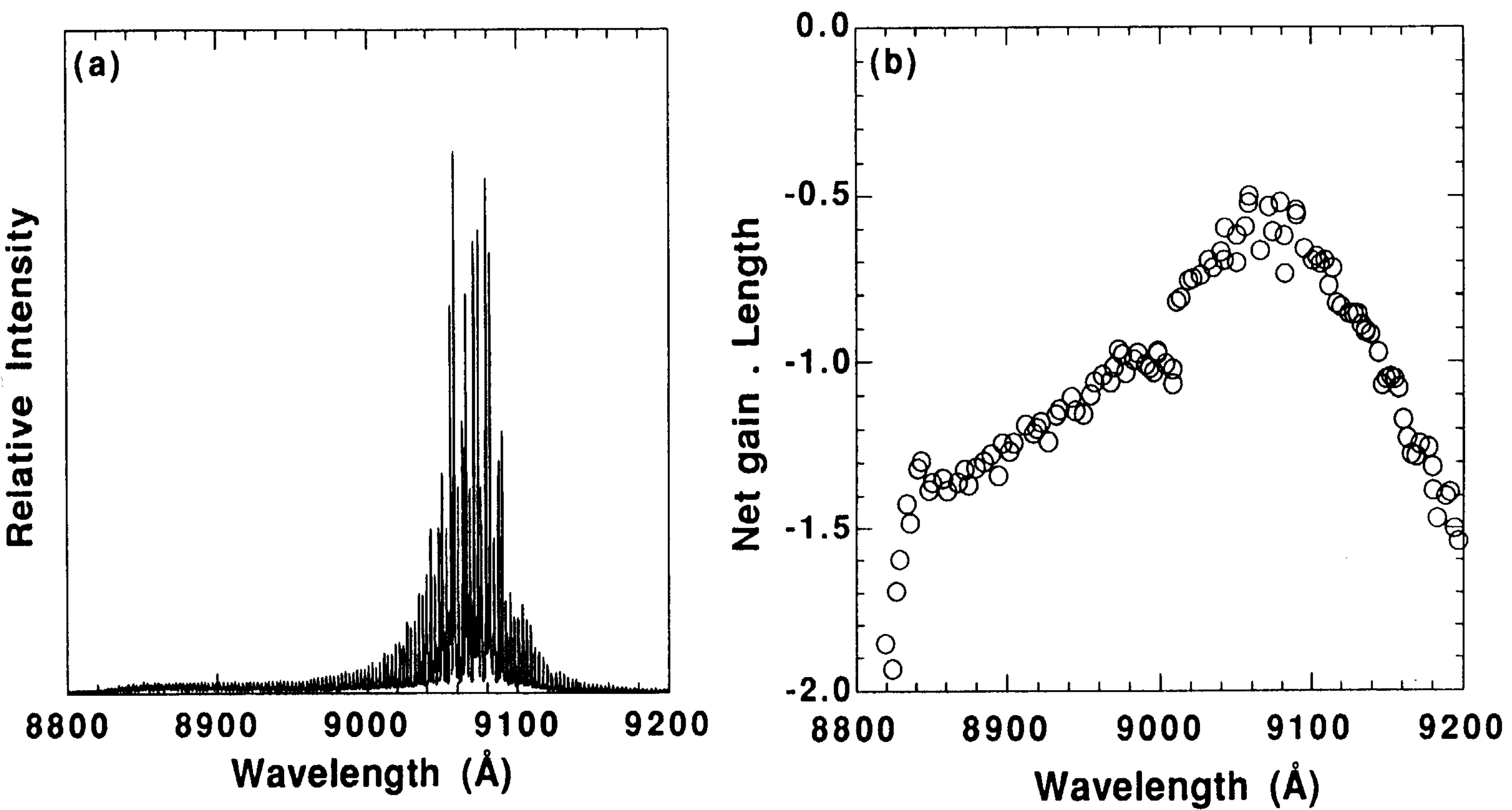

Figure 3.19. (a) Intensity spectrum and (b) (netgain.length) at I= 302 mA for 15 μm x 355 μm

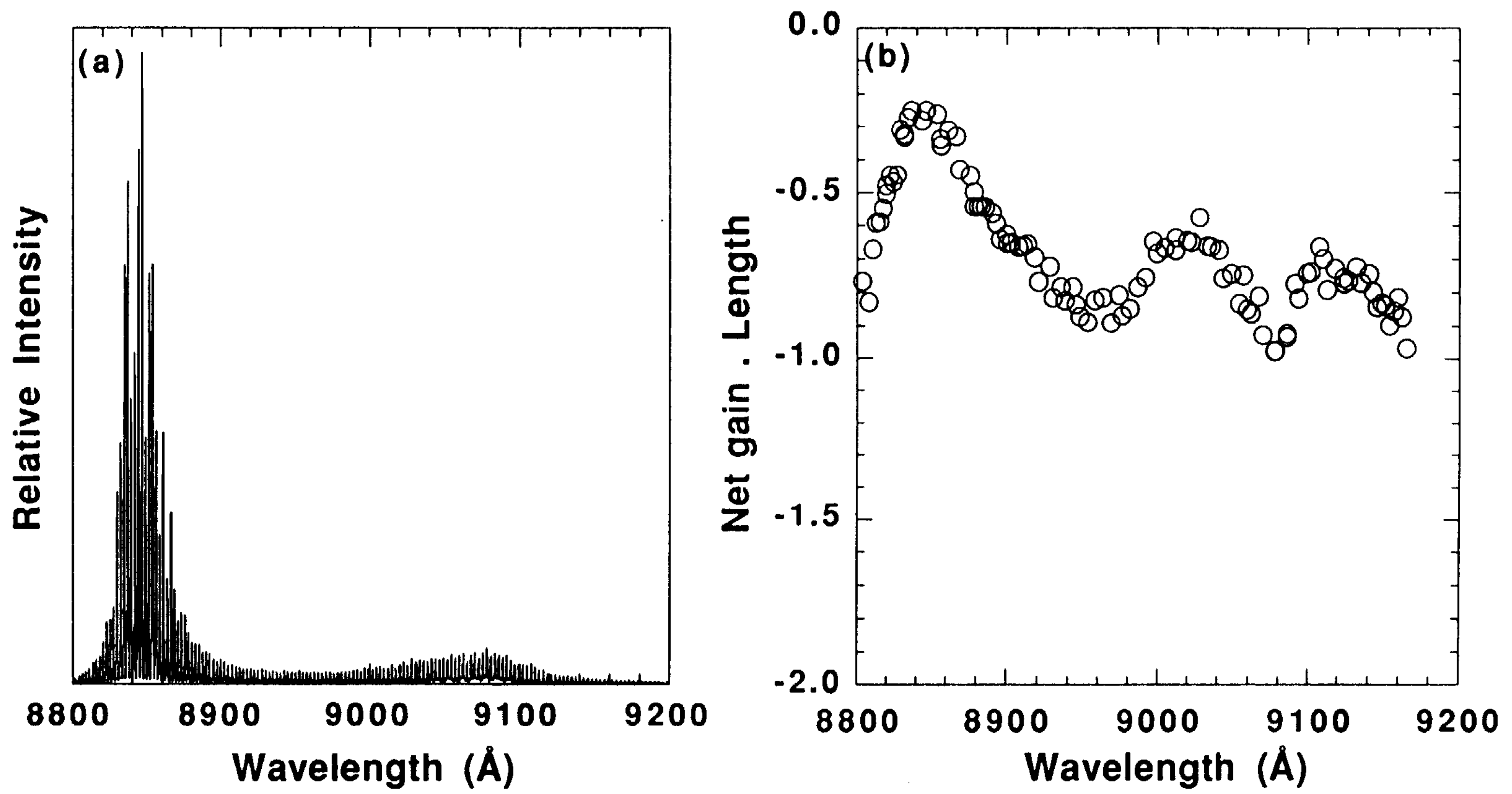

Figure 3.20. (a) Intensity spectrum and (b) (netgain.length) at I = 330 mA for 15 μm x 355 μm.

the gain at current levels beyond 260 mA. The respective net gain curves obtained using the above relation for the spectra of Figs. 3.18a, 3.19a, and 3.20a is shown in Fig 3.18b, 3.19b and 3.20b. As a result of a residual background signal in the boxcar (± 2 mV r.m.s.) contributing to a baseline error, the maximum net gain calculated does not reach zero at threshold (≈ 236 mA). For the current level of 236 mA, where the laser lases only at the n=2 level, a clear gain narrowing near 910 nm is seen. Note that this current is beyond the first threshold and hence would be consistent with the onset of lasing. However, with increasing drive level, the gain near 910 nm is reduced coupled with gain broadening towards shorter wavelengths due to bandfilling of higher energy levels. A noticeable gain peak is seen to appear near 884 nm wavelength. At 330 mA, the gain increases to its maximum near 884 nm wavelength with a spectral "hole" burnt in the gain profile at the longer wavelength near 908 nm, possibly due to onset of nonlinear gain saturation there. The spectral hole burning and the associated bandfilling leading to a broadening of the gain profile towards shorter wavelengths (higher energies) facilitates the onset of lasing at the shorter wavelength of the barrier (885 nm).

A plot of the netgain-length product at different drive levels for the two transitions, i.e., 911 nm and 884 nm, is shown in Fig 3.21 . The gain at the longer wavelength does rise rapidly then saturates around threshold (236 mA) but is soon suppressed beyond and settles to a relatively constant value beyond 270 mA. The reason for the observed abrupt changes in the value for the peak gain for currents even below threshold is not clear but could possibly indicate to the existence of gain nonlinearities, enabling increased bandfilling towards higher energy levels, and spectral hole burning effects at higher drive

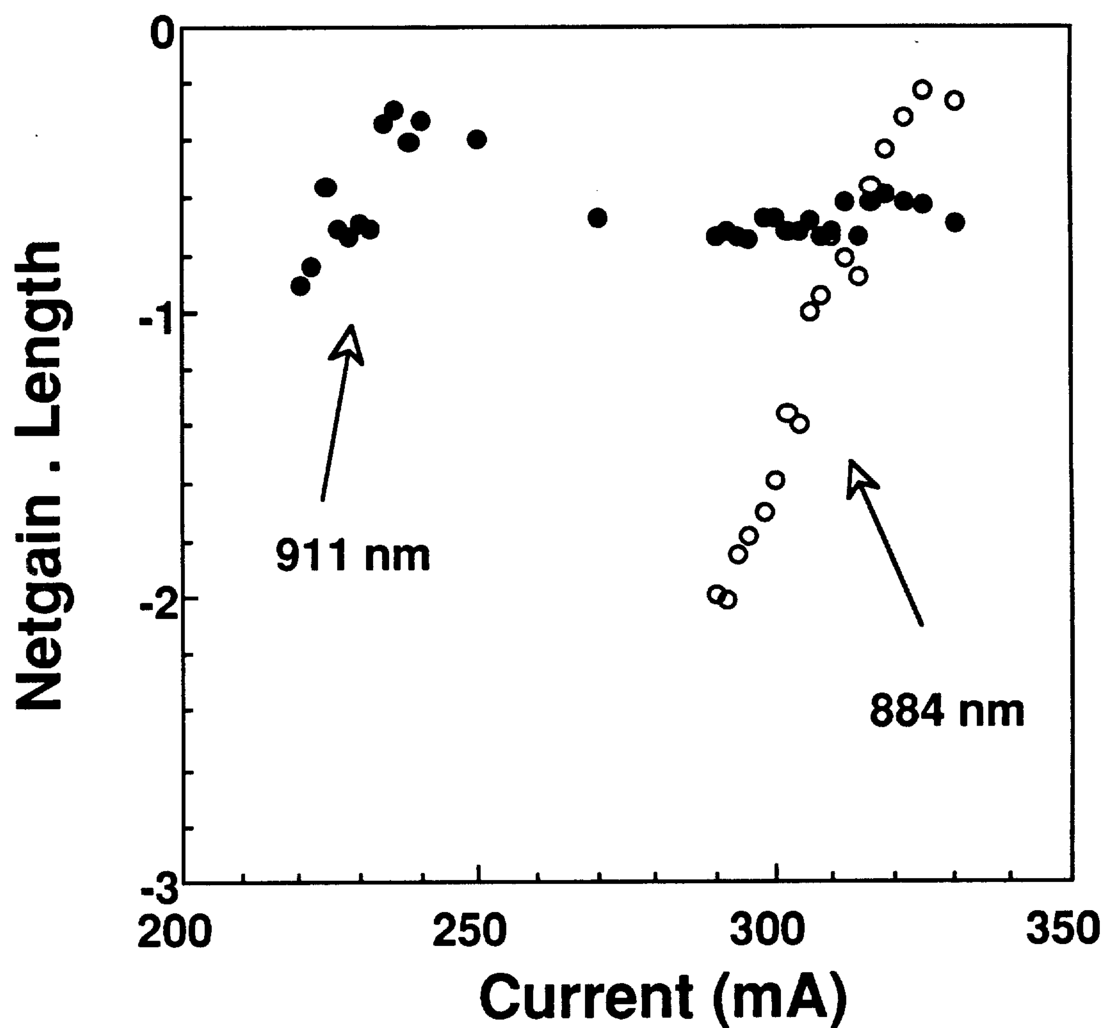

Figure 3.21. Netgain-Length product at various injection levels for modes at 911 nm (n=2 transition) and 884 nm (barrier transition), corresponding to the gain peaks of both transitions.

current levels. However, at the shorter wavelength transition, the gain increases linearly from about 290 mA to the second threshold of about 325 mA. A comparison of the slopes at the two wavelengths was not possible due to the substantial gain compression effects near 911 nm.

3.3.4.2. The 15 μm × 575 μm Device

The longer cavity length of 575 μm was selected to provide for a reduced mirror loss, thus making available the longer wavelength n=1 transition in addition to the n=2 and the barrier transition (see Fig. 3.15b). The severe kinks observed in the light-current curve (Fig. 3.15a) coincides with the appearance, but not yet lasing (at ≈ 400 mA), of the n=2 transition, and also eventually the appearance of modes corresponding to the barrier transition (at ≈ 450 mA). The device began to lase at the n=2 transition beyond 500 mA and at the barrier around 600 mA. A clear identification of the "thresholds" for the higher energy transitions is certainly not possible.

The time-averaged spectral measurements showed some interesting behavior. At around 285 mA the device was well into the saturation in power output and began to lase around 967 nm shifting from the initial operating wavelength of around 975 nm. Fig 3.22 is a plot of the spectral content at 285 mA. At 400 mA, the device switches to the n=2 transition (910 nm) with a large number of longitudinal modes present, as shown in Fig 3.23, but not yet lasing. At a slightly higher current level of around 453 mA, Fig 3.24, the device begins to show the barrier transition around 886 nm with the n=2 still present.

However, beyond 500 mA, the device began to exhibit broad spectral

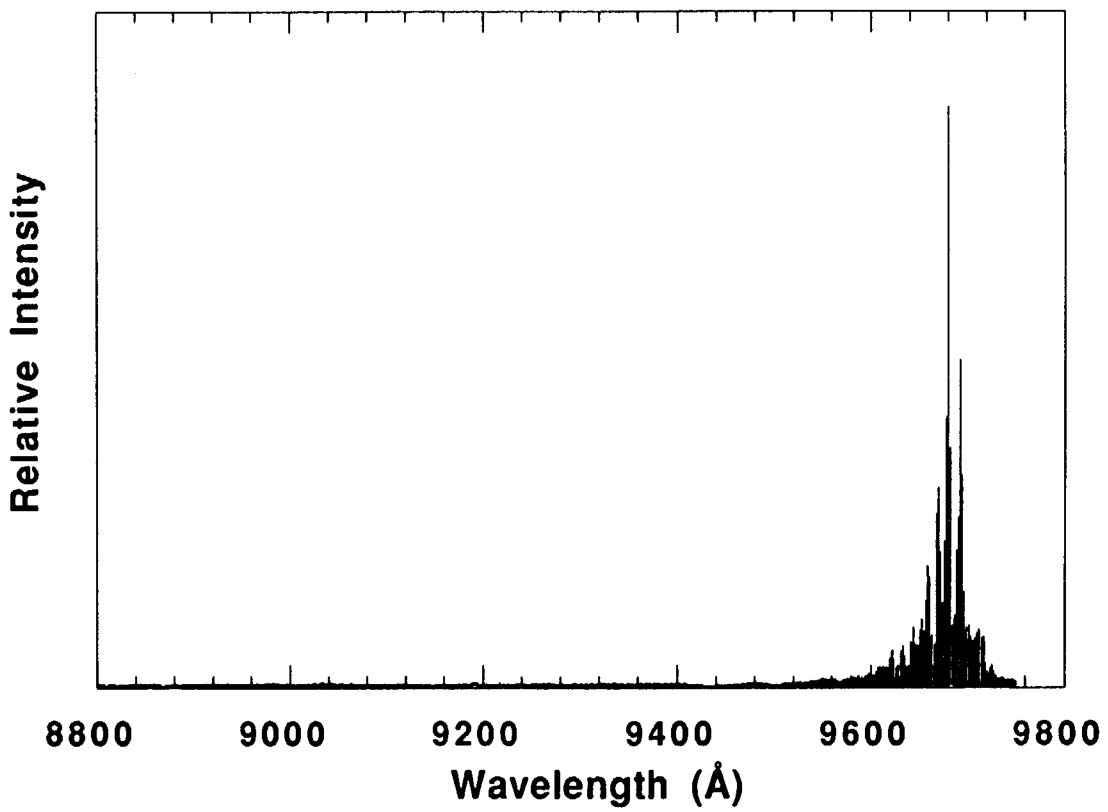

Figure 3.22. Intensity spectrum at I = 285 mA for the 15 μm x 575 μm device.

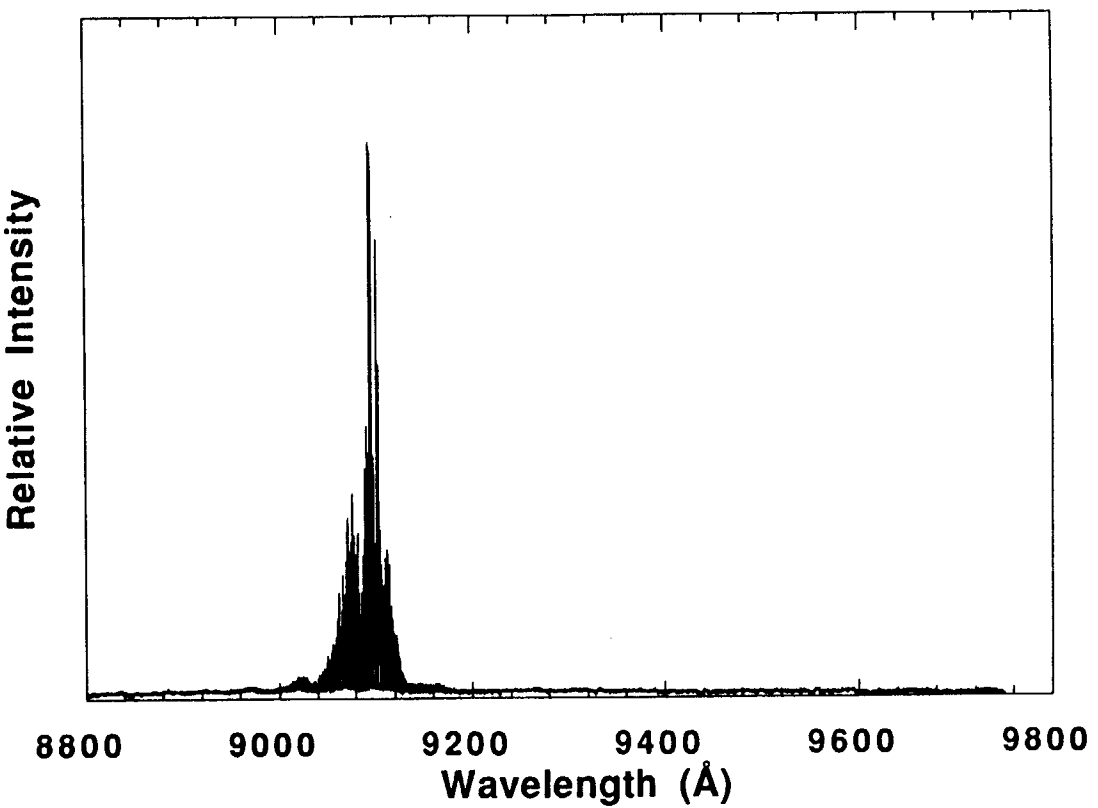

Figure 3.23. Intensity spectrum at I = 400 mA for the 15 μm x 575 μm device.

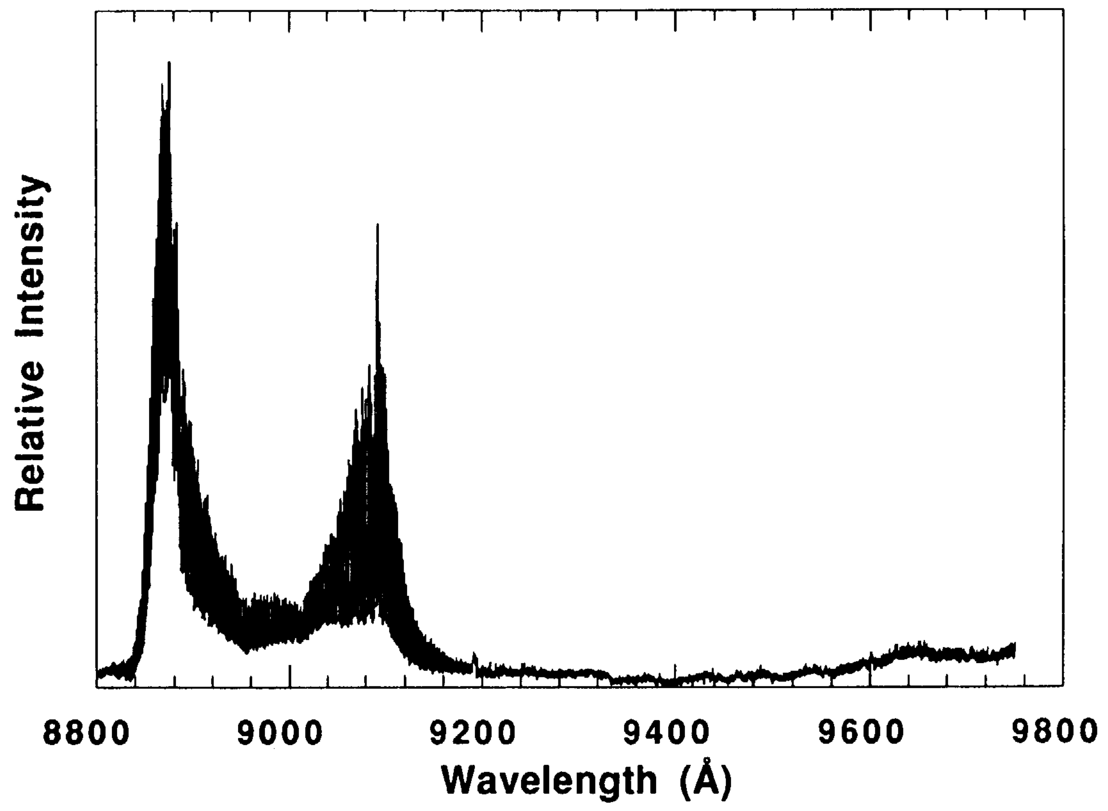

FIgure 3.24. Intensity spectrum at I = 453 mA for the 15 μm x 575 μm device.

bands instead of well defined longitudinal modes. Figs. 3.25, and 3.26 at the current levels of 500 mA and 550 mA clearly show the degradation of the spectrum from that of Fig 3.23 with modes beginning to disappear and leading to a certain "oscillatory" tendency. When observing the spectrally resolved near fields on the monitor using the CCD camera it was found that the modes at the shorter wavelength of the barrier regions tend to go into "self-oscillation" previously observed in stripe-geometry DH lasers[72] giving rise to a broad spectrum due to the frequency shifting during the pulses (chirping) i.e., the wavelength of any mode changes with time. Brouwer *et al.*[72] explained it by a nonuniform gain profile along the lateral dimension leading to the lateral instability. The "self-oscillation" observed is also consistent with the fact that a thicker active region (i.e. including the barrier) forms the waveguide in the transverse vertical dimension at the high injection levels and could thus influence the lateral gain profile due to the difference in the carrier density and the dielectric constant of the layers.

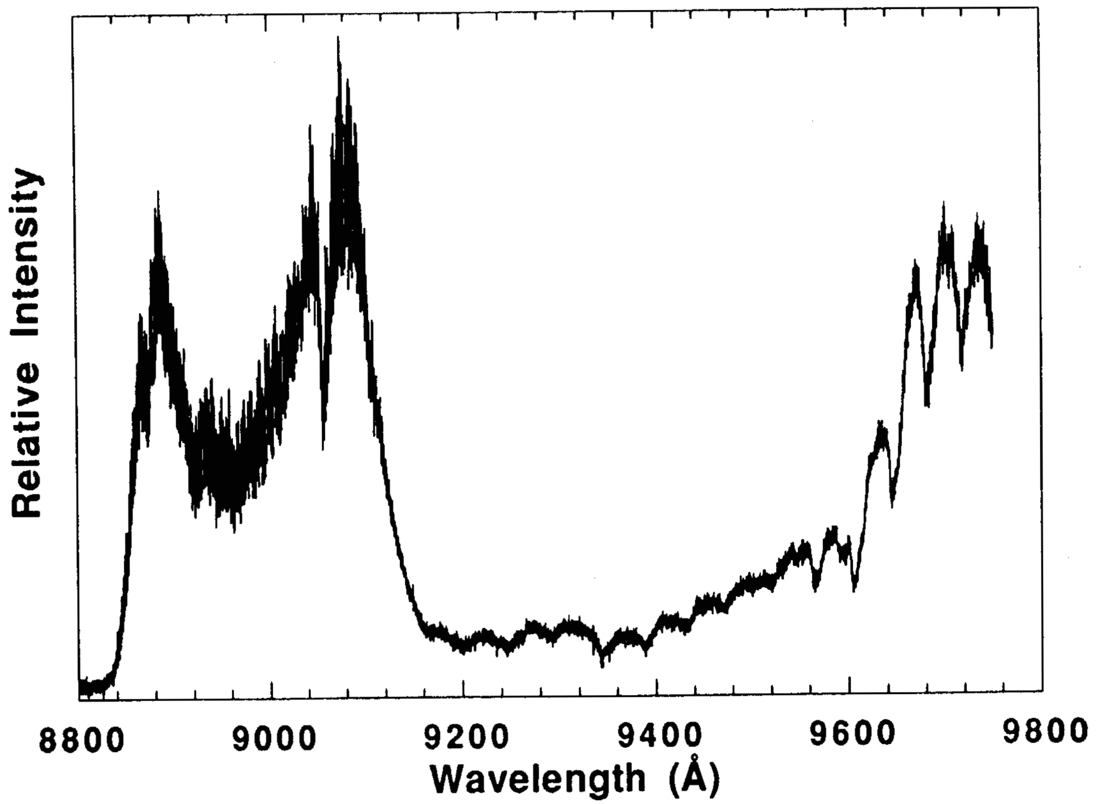

Figure 3.25. Intensity spectrum at I = 500 mA for the 15 μm x 575 μm device.

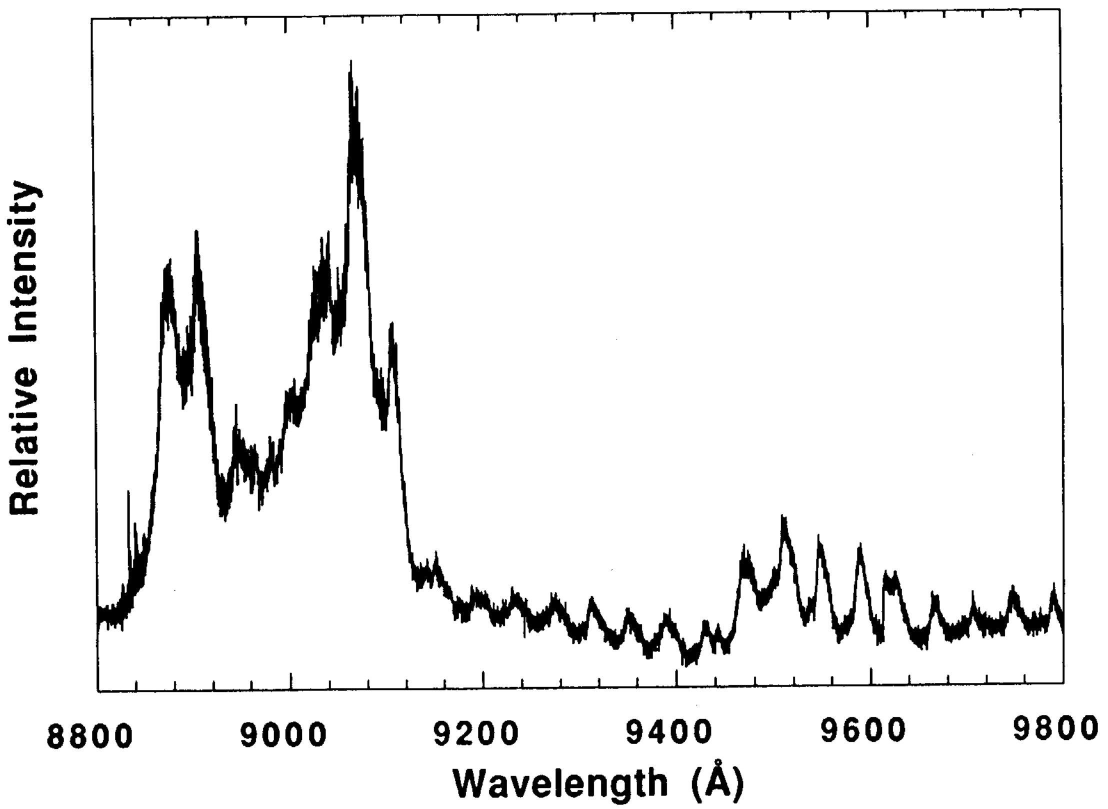

Figure 3.26. Intensity spectrum at I = 550 mA for the 15 μm x 575 μm device.

Chapter 4

TEMPORAL STUDIES OF WAVELENGTH SWITCHING

4.1 Introduction

The potential for use of strained-layer QW lasers for wavelength switching, arising from increased bandfilling of higher energy levels due to larger cavity losses was described in the previous chapters. Our investigations had shown explicit dependence on cavity dimensions for appropriate switching of lasing wavelengths with injection level. As discussed in Chapter 3, the systematic investigations of the spectral characteristics of such devices showed "simultaneous" (time-integrated sense) operation of two or more wavelengths (corresponding to n=1, n=2 or the barrier). In this chapter we present experimental investigations, of devices that exhibit such large shifts in lasing wavelengths, (i) into the time dependent spectral behavior, based on pulse gating techniques, as well as (ii) into the intrinsic frequency of relaxation oscillations based on sub-nanosecond resolved light pulse measurements.

4.2 Experiment

4.2.1 Devices

Two sets of experiments were performed to investigate the switching behavior on devices that exhibited change in lasing wavelength with increasing injection level. A 15 μm × 200 μm device was used for the spectral investigations and a 15 μm × 600 μm device was chosen for observation of the light pulse using a high speed signal analyzer and transient digitizer since the former (200 μm) device had a nonlinearity in the light-current characteristic due to a saturable absorber like behavior. The choice of 15 μm stripe widths was based on the cavity dependence studies which showed that devices in this class consistently exhibited injection level dependent operation, sometimes "simultaneously" (in a time integrated sense), in all three wavelengths of interest, viz., 980 nm, 910 nm and 885 nm corresponding to the n=1 (e1-hh1), n=2 (e2-hh2) and the barrier (GaAs) transitions.

4.2.2 Set up for spectral studies

As in the previous experiments discussed in Chapter 3, the 15 μm × 200 μm device was operated in pulsed mode with 10 kHz repetition rate and a 100 ns pulse width to avoid heating. The device mount was also actively cooled and maintained at a temperature of 20 °C. The spectrally resolved near fields as a function of the drive current were recorded using the set up described in section 3.4.2 . The gating scheme used will be described in section 4.3.2 .

4.2.3 Set up for dynamic studies

The 15 μm × 600 μm device was operated in pulsed mode with 10 kHz repetition rate and 30 ns pulse widths. The reduced pulse width was used since all switching behavior happened within the 30 ns and also reduced any heating effects or current pulse amplitude jitter that could corrupt the light pulse measurements. The experimental arrangement is as shown in Fig. 4.1. The laser output was coupled into a 100 μm multimode fiber using a 16X microscope objective. The other fiber end was connected to a 20 GHz (Tektronix SD-46) optical to electrical converter. The converter has an InGaAs photodetector with a relative responsivity of 1.0 at 1.3 μm and a maximum around 1.55 μm of 1.1 . The responsivity falls gradually towards 1.2μm and when extrapolated to 0.8μm is around 0.2. We did not correct the measured output for the difference in the responsivity at the different wavelengths of interest (0.98 μm and 0.88 μm). The electrical output of the SD-46 was fed into a fast (26 GHz) electrical sampling head (Tektronix SD-26). Both sampling heads were mounted in the Tektronix CSA 803 communication signal analyzer which was triggered from the current source. The current pulse was obtained with the current probe fixed close to the laser diode. The waveforms were displayed in an averaged mode to remove noise or random output. The signal analyzer displays a single trace by sampling over many pulses. The CSA 803 bases the sampling process on a trigger event. When the trigger event is detected the CSA 803 waits a specific period of time before sampling. After the first point is digitized, the CSA 803 waits for another trigger event before continuing to sample and digitizing the second point. The sampling interval

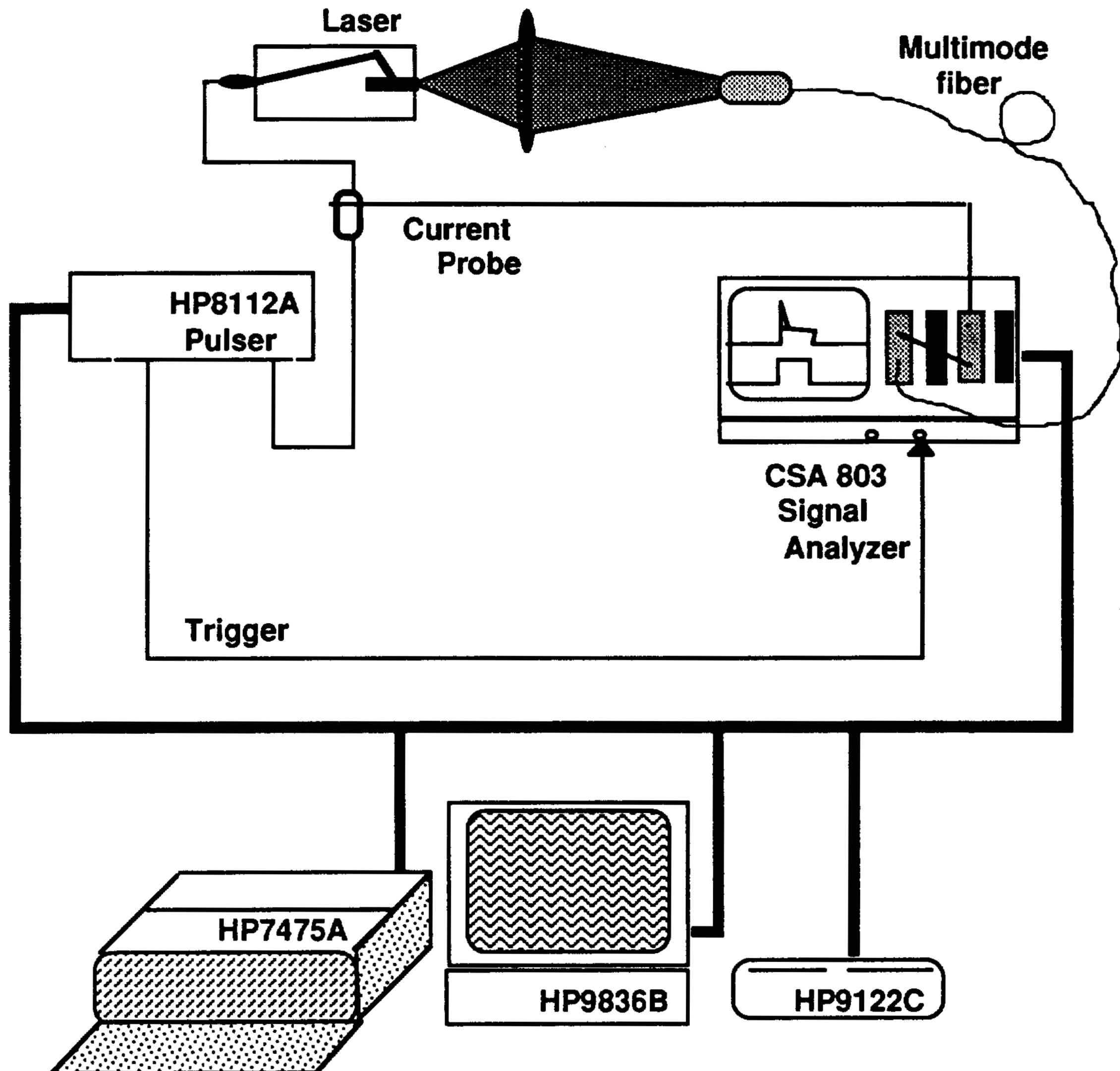

Figure 4.1. Picosecond resolved light pulse measurement set up using DC-20 GHz optical to electrical and DC-26 GHz electrical sampling heads with TEK CSA 803 Signal Analyzer.

which is the time difference between successive points on the pulse, depends on the settings for the displayed trace. With a display of 100 ns of time and if the trace has 2048 data points, then the sampling interval is 100 ns divided by 2048, or 48.8 ps. Since each data point is obtained from a separate trigger event, 2048 pulses would be sampled successively to obtain the above trace of 100ns of time. A 7 GHz Tektronix SCD 5000 transient waveform digitizer was therefore used to capture single light pulse sweep for each trigger to help investigate the switching. The output of the signal analyzer and the transient digitzer were recorded at different injection levels using a HP 9000 series 300 computer over the HPIB for further analysis.

4.3 Results and discussion

4.3.1 Spectral studies

4.3.1.1 Device characteristics (15 μm × 200 μm)

Fig. 4.2a shows the light - current curve for the 200 μm long device measured in the averaged mode using Tektronix digital photometer (J16/J502A). The threshold was 145 mA and had an abrupt jump in light intensity due to the presence of a saturable absorber in the cavity. This caused self-sustained pulsations in the light output. Basov[73] first related this behavior to such saturable absorber effects. Although the nature of the centers for such absorption is not well known, some of the reasons that have been put forth are deep level traps[74,75], microdegradation distributed throughout

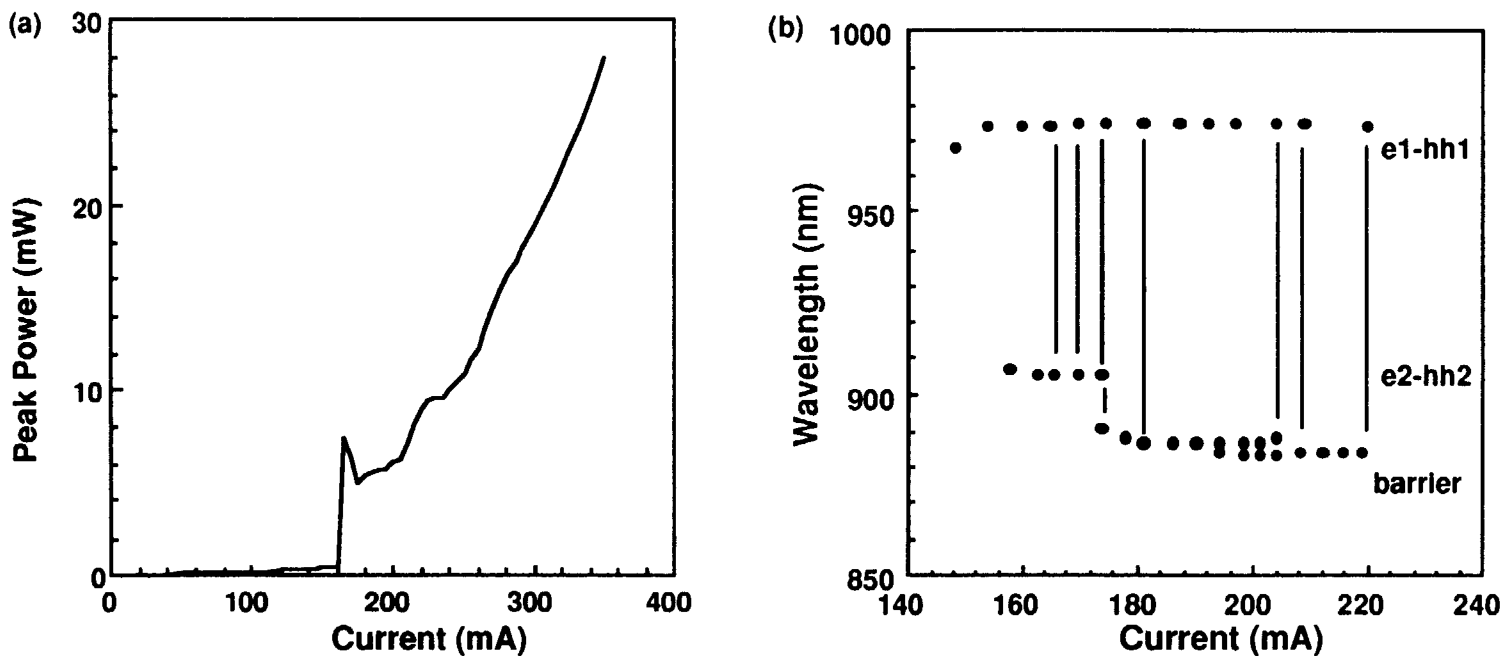

Figure 4.2. (a) Light-current characteristic and (b) lasing wavelength for 15 μm × 200 μm sample in pulsed operation. Observed transitions are n=1 (975 nm), n=2 (912 nm) and barrier (886 nm). Vertical lines in (b) indicate "simultaneous" transitions.

the active region[76], mirror facet degradation[77], or proton induced damage[78,79]. Saturable absorption is induced by most of these mechanisms[80] and more than one mechanism may be involved simultaneously. Stripe-geometry gain guided devices patterned by proton bombardment often exhibit such self-pulsations[72,78,81,82]. Though not very well understood, it is possible that the defects, introduced by this technique and subsequent annealing, act as centers of nonradiative recombination, resulting in an increase in the optical absorption and a consequent decrease in the radiative efficiency.

The laser initially lased around 975 nm (n=1) and subsequently shifted to shorter wavelengths (886 nm). A plot of the wavelength shift with injected current is shown in Fig. 4.2b . Although not indicated in the plot, the device was indeed found to lase at two or all three wavelengths "simultaneously" as mentioned before for other devices. The light pulse as detected with a 200 MHz (Judson Si diode FFD-200) photodetector was observed using the set up shown in Fig. 4.3 . The electrical output was viewed using the 500 MHz HP digitizing oscilloscope and used to investigate if the laser lased at the different portions of the pulse at different injection levels. Fig. 4.4(a,b) show the display of the oscilloscope traces for the current and the light pulse at two drive levels. The lower trace in both plots is the input current pulse and the upper trace of the inverted pulse is the light pulse as detected with the photodetector. The delay between the light pulse and the current pulse includes the inherent delay in onset of lasing and the "line" delay of the electrical cables. A 100 ns current pulse was used. The horizontal cursor bars indicate the amplitude of the current and the vertical cursor bars indicate the time duration of the light pulse. At the input current level of 166 mA, there is

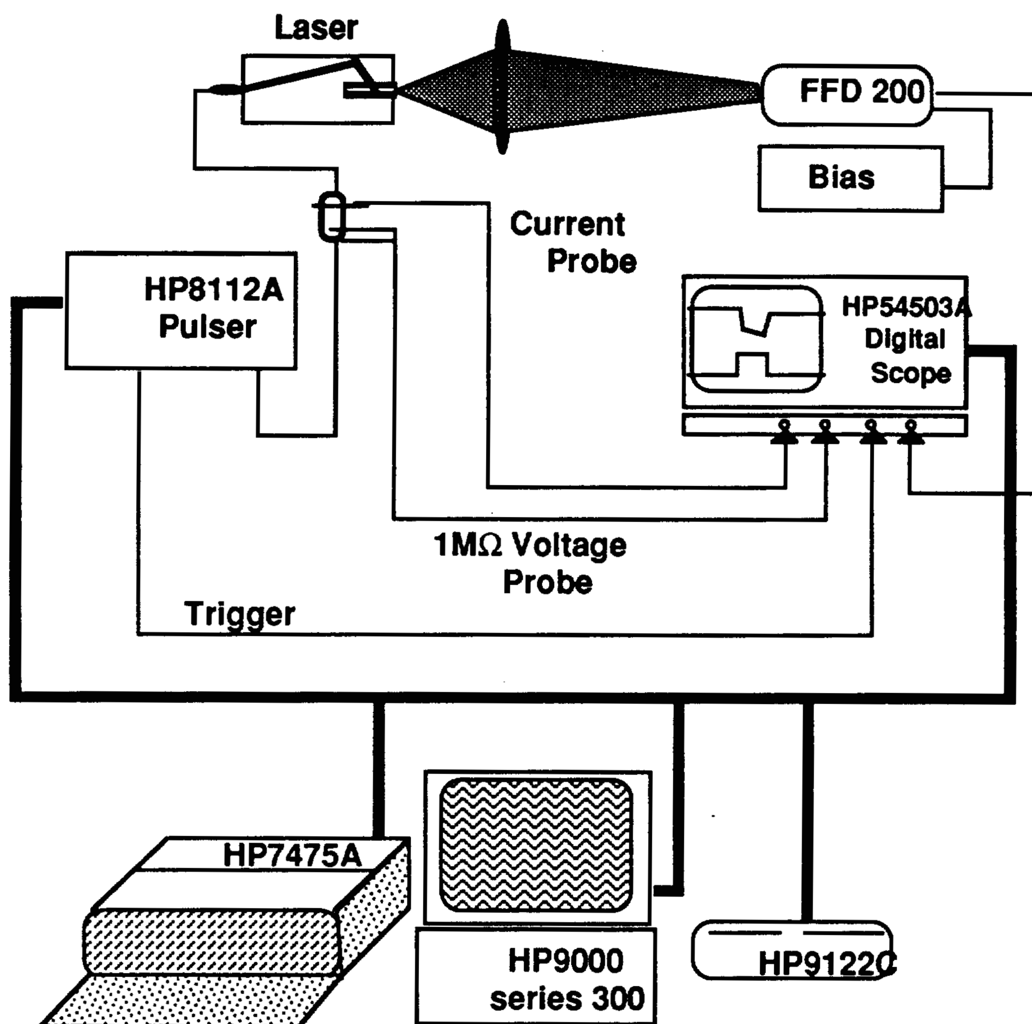

Figure 4.3. Set up using 200 MHz EG&G Judson photodetector to monitor light pulse on digitizing oscilloscope and to measure pulsed light-current.

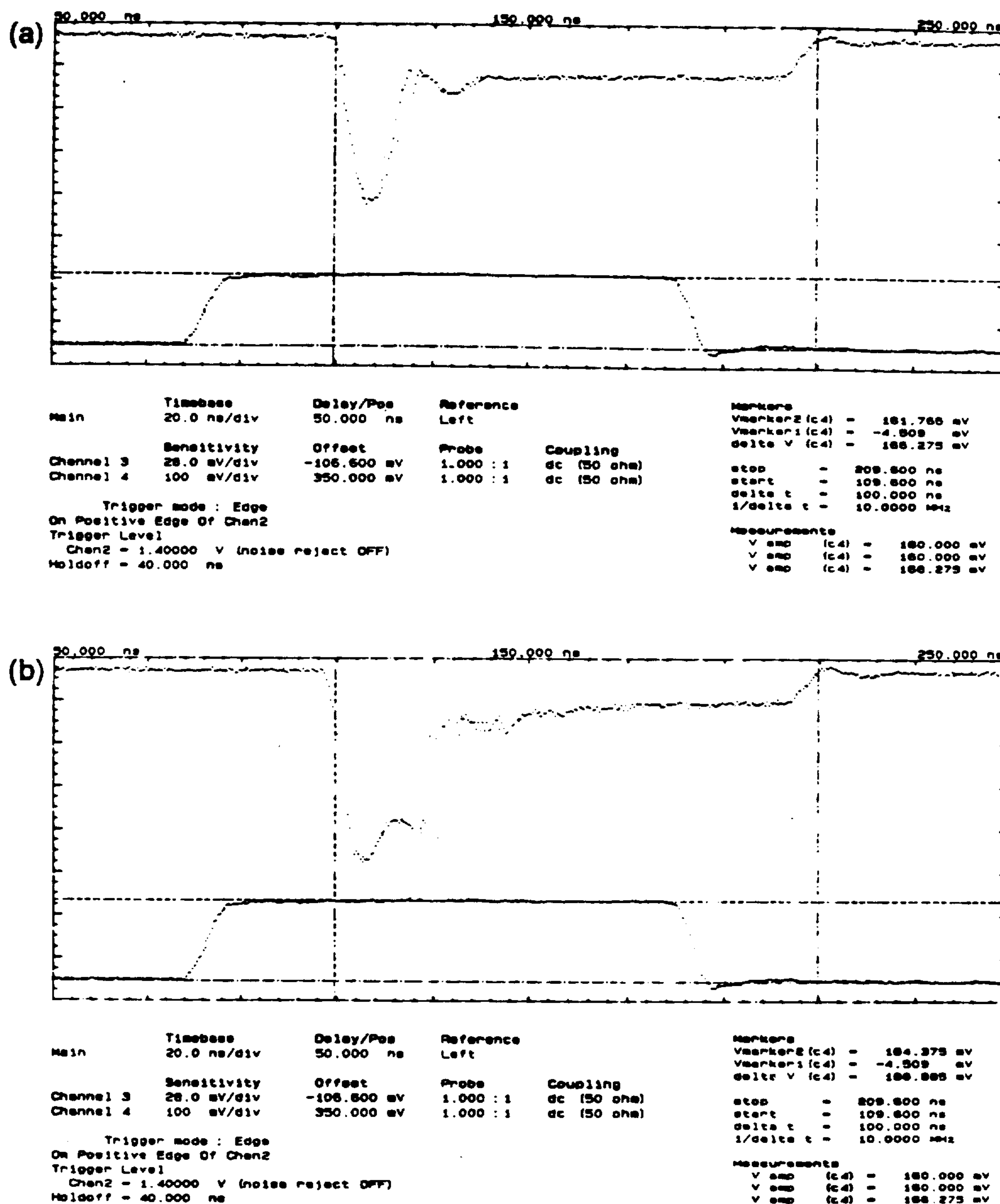

Figure 4.4. Light pulses (inverted top traces) as detected by the reverse biased FFD-200 detector for 15 μm x 200 μm device at (a) I = 166 mA and (b) I = 188 mA. Input current pulses are the lower traces in both figures.

a clear peak in the first 25 ns of the light pulse and remains flat for the rest of it's duration, possibly continuing to lase. When the drive level is increased to 188 mA, there is a second peak immediately after the first peak and a relatively flat portion for the remainder of the pulse. It is also somewhat clear that there is a switching in the pulse amplitude around the second peak indicating that the device could possibly be operating in a different mode from that of the first peak. Since the selected device also operated at different wavelengths (Fig 4.2b), the spectrometer was used to resolve the different wavelength regions at the peak intensity of the longitudinal mode in the wavelength region of interest, i.e., n=1 : 975 nm, n=2 : 906 nm, and barrier: 884 nm. Although ideally speaking it would be better to choose a current level and show that the device lased at two different wavelengths at different portions of the light pulse, the presence of electrical noise and the lack of sufficient light signal prevented such a measurement. Nevertheless, to show clearly that the device indeed lased at different portions, different current levels were chosen for observing the light at the three wavelengths of interest. To collect sufficient signal to overcome the noise floor in the detected signal, the current level chosen was 188 mA for the longest wavelength (Fig. 4.5a, cf Fig. 4.4b) : the 975 nm signal showed a clear peak in the first 20 ns and dropped below the noise level afterwards. For the signal at 906 nm the current level of 167 mA was chosen (Fig. 4.5b) and for the signal at 884 nm a current level of 220 mA (Fig. 4.5c). In both cases there was no light detected in the first 15 ns and signal was present after that. Since a mode in the wavelength of interest was being detected, the light output at the longer wavelength (n=1) for the current levels of 167 mA and 220 mA was not

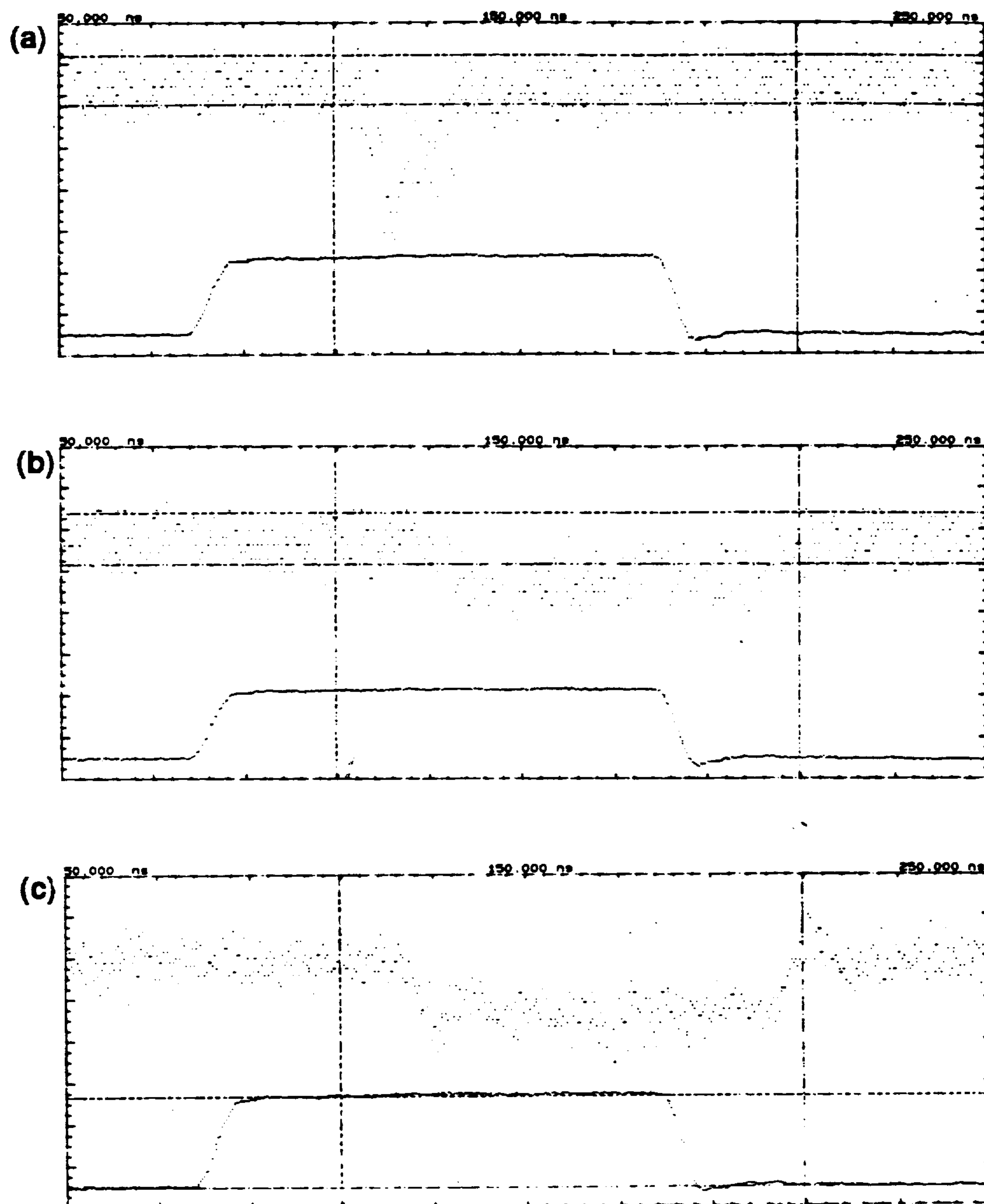

Figure 4.5. Spectrally resolved light pulses (upper inverted traces) for modes located at (a) 975 nm (I = 188 mA), (b) 906 nm (I = 166 mA), and (c) 884 nm (I = 220 mA). The horizontal cursors in (a) and (b) are shown to distinguish the signal from the noise background. The vertical cursor separation is 100 ns.

sufficient to cross the noise floor. The horizontal cursors in the first two cases indicate clearly the noise floor in the detected signal and the light signal over and above this noise floor. Note that in all these figures the vertical cursor position was not changed with respect to Fig. 4.4 . It is evident that the device initially lased at the longer wavelength (n=1) and subsequently switched to the shorter wavelength (n=2 or barrier) depending on the injection level. However this does not prove conclusively that the longer wavelength ceases to exist beyond the first 15 ns of the light pulse.

4.3.1.2 Spectral characteristics (gated measurements)

In view of these results extensive spectral investigations were done at various injection levels to understand in a systematic manner the wavelength switching process. The objective of the spectral measurements was two fold: to evaluate the spectral content at various injection levels and to determine if indeed there was a time dependence in the spectral content. Having observed the behavior of the light pulse with the photodetector, it was decided to use 50 ns gates to have sufficient signal for the detection system. The measurements were done with gates positioned so as to sample the first or the second half of the 100 ns pulse.

Figs. 4.6a - 4.9a and 4.6b - 4.9b show the spectra measured at four different current levels gated in the first half and the second half of the 100 ns pulse, respectively. In each of the figures the current pulse with a shaded region indicates the gated portion used for the spectral measurements. At 155 mA (Fig. 4.6), the n=1 transition is observed in the first 50 ns with

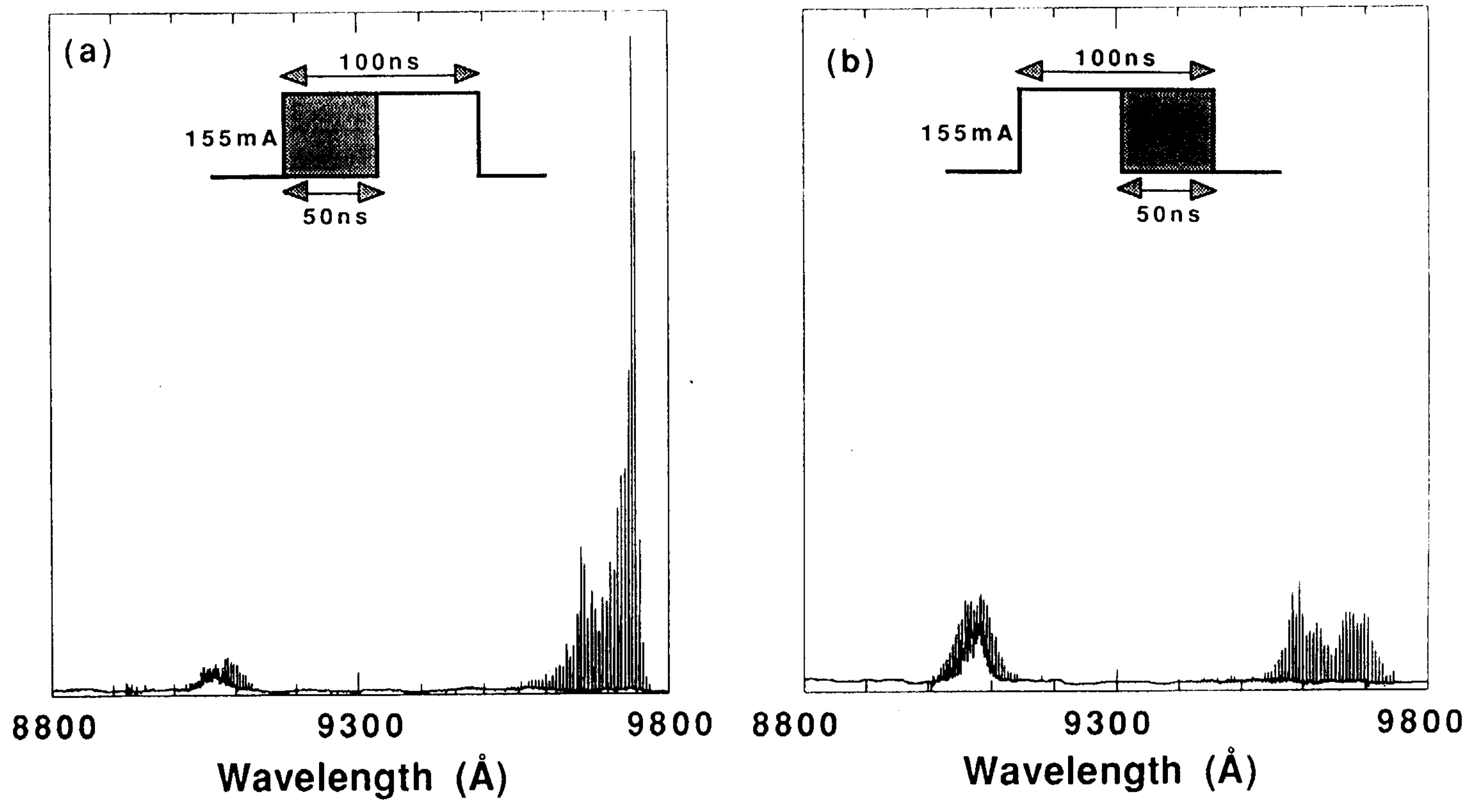

Figure 4.6. Intensity spectra at I = 155 mA for 15 μm x 200 μm sample. (a) 50 ns gate positioned in the first 50 ns of the 100 ns current pulse and (b) 50 ns gate positioned in the second 50 ns of the 100 ns pulse.

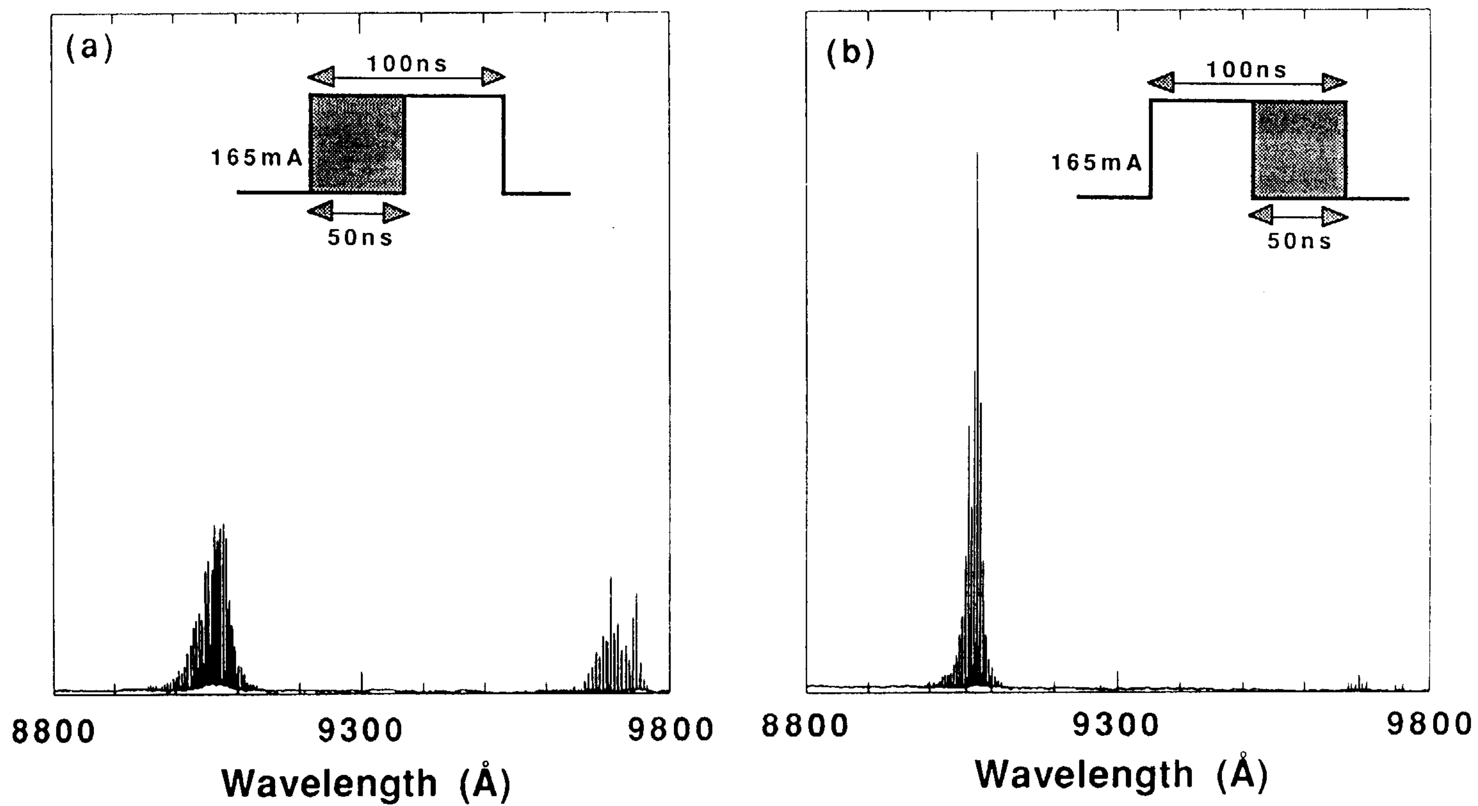

Figure 4.7. Intensity spectra at I = 165 mA for 15 μm x 200 μm sample. (a) 50 ns gate positioned in the first 50 ns of the 100 ns current pulse and (b) 50 ns gate positioned in the second 50 ns of the 100 ns pulse.

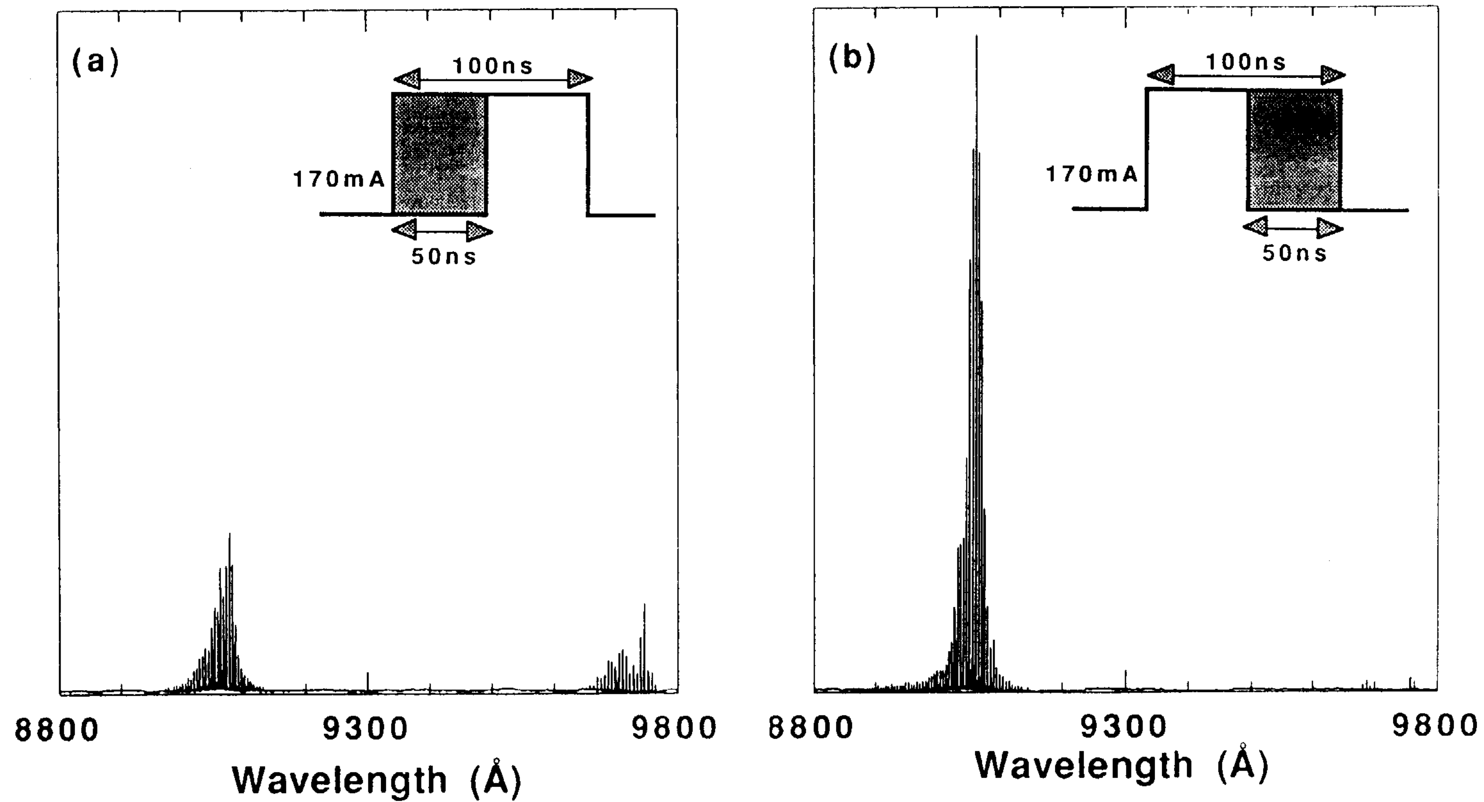

Figure 4.8. Intensity spectra at I = 170 mA for 15 μm x 200 μm sample. (a) 50 ns gate positioned in the first 50 ns of the 100 ns current pulse and (b) 50 ns gate positioned in the second 50 ns of the 100 ns pulse.

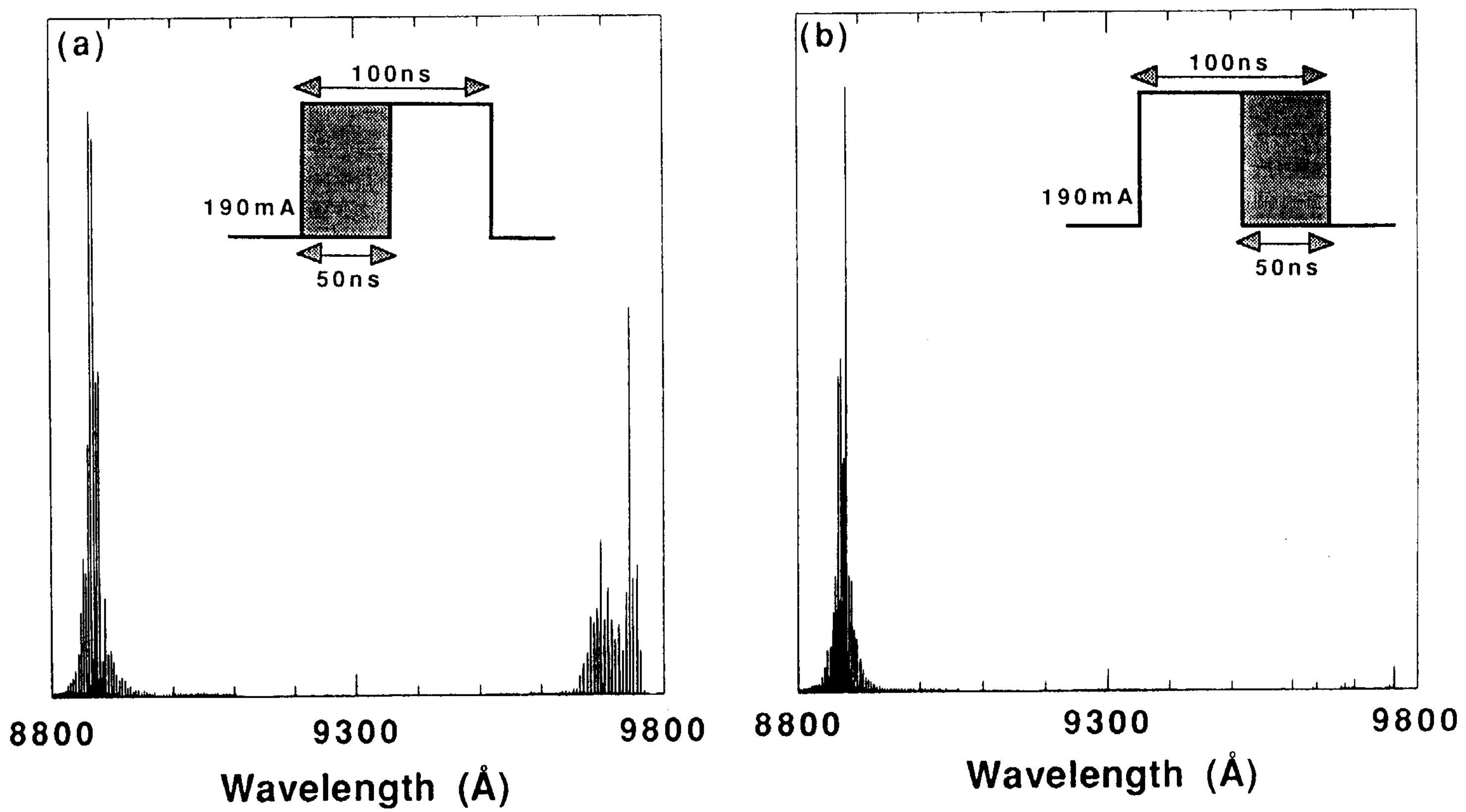

Figure 4.9. Intensity spectra at I = 190 mA for 15 μm x 200 μm sample. (a) 50 ns gate positioned in the first 50 ns of the 100 ns current pulse and (b) 50 ns gate positioned in the second 50 ns of the 100 ns pulse.

spontaneous emission at the n=2 and a reduced n=1 during the second 50 ns. At 165 mA (Fig. 4.7), the n=2 transition becomes dominant in both 50 ns portions growing stronger in the second half where the n=1 almost disappears. With just a 5 mA increase to 170 mA (Fig. 4.8a) the n=2 builds up even stronger during the second 50 ns, but otherwise the situation essentially remains the same as for 165 mA. When the injection level is increased to 190 mA (Fig. 4.9) the laser has switched to the barrier transition (887 nm) being dominant both in the first and second 50 ns portions. However, the n=1 transition which had been diminished at 170 mA (Fig. 4.8) has reappeared more strongly during the initial 50 ns but remains barely evident in the second 50 ns.

A double pulse measurement was used to investigate further this time-dependent spectral behavior. Two current levels were chosen: 167 mA and 185 mA, based on the fact that switching between the n=1 and n=2 levels and the n=1 and the barrier were observed between the two halves of a 100 ns pulse as shown in Fig 4.10 and Fig 4.11 . In the double pulse experiment the separation between the two 50 ns pulses, with rise and fall times of ≈ 4.5 ns, was changed to 5 ns, 15 ns and 25 ns at each current level. Only the second pulse was gated in each case. It is found that the shorter wavelength reduces in intensity and the n=1 transition becomes stronger as the separation increases to 25 ns in both current levels as shown in Fig 4.12 and 4.13 . From the double pulse experiment we can conclude that the switching from the n=1 to the n=2 or the barrier starts earlier in the second pulse when the separation between the two pulses is small. Comparing these results with the earlier light pulse measurement we see that the laser indeed lased at the longer n=1

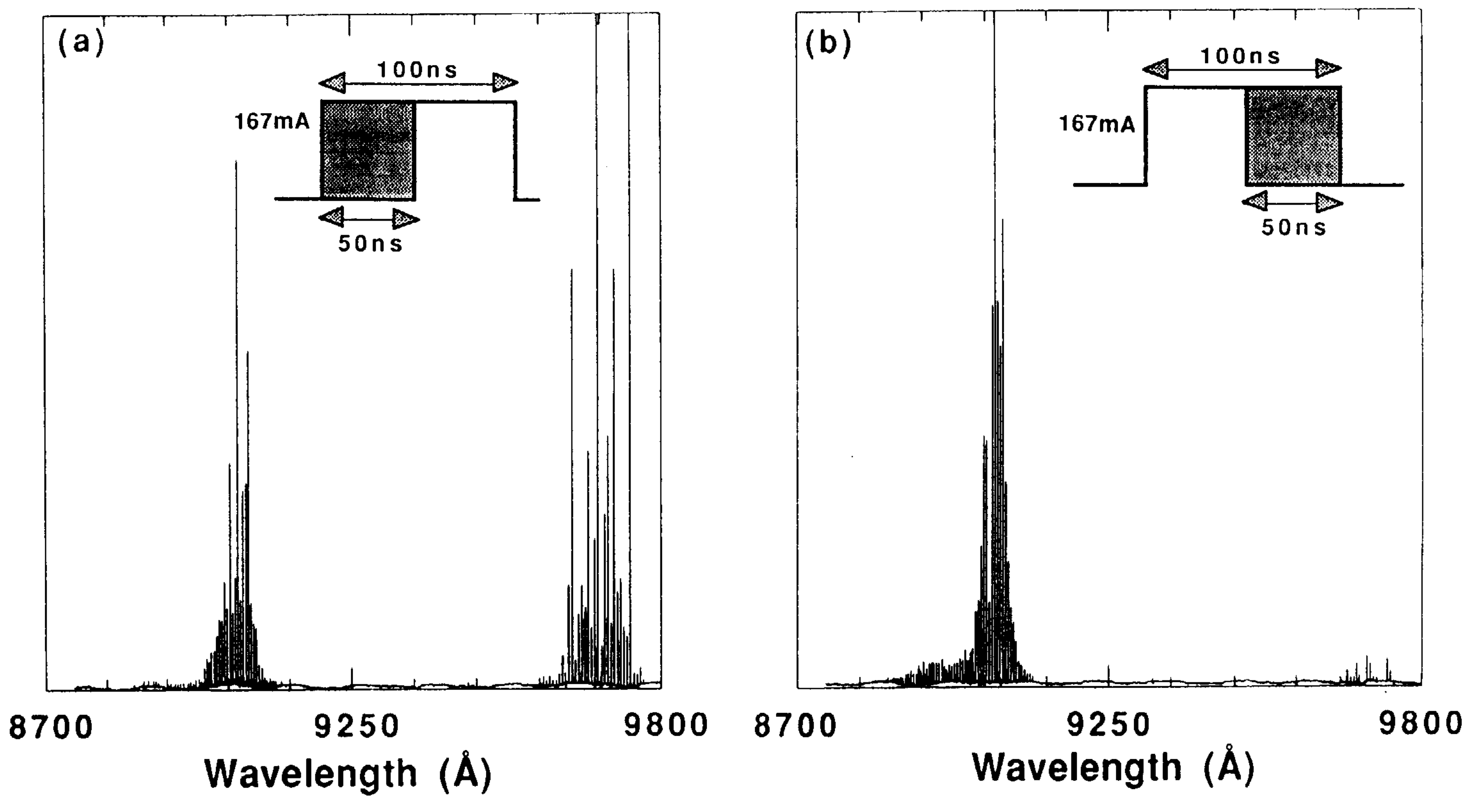

Figure 4.10. Intensity spectra at I = 167 mA for 15 μm x 200 μm sample. (a) 50 ns gate positioned in the first 50 ns of a 100 ns pulse and (b) 50 ns gate positioned in the second 50 ns of the pulse.

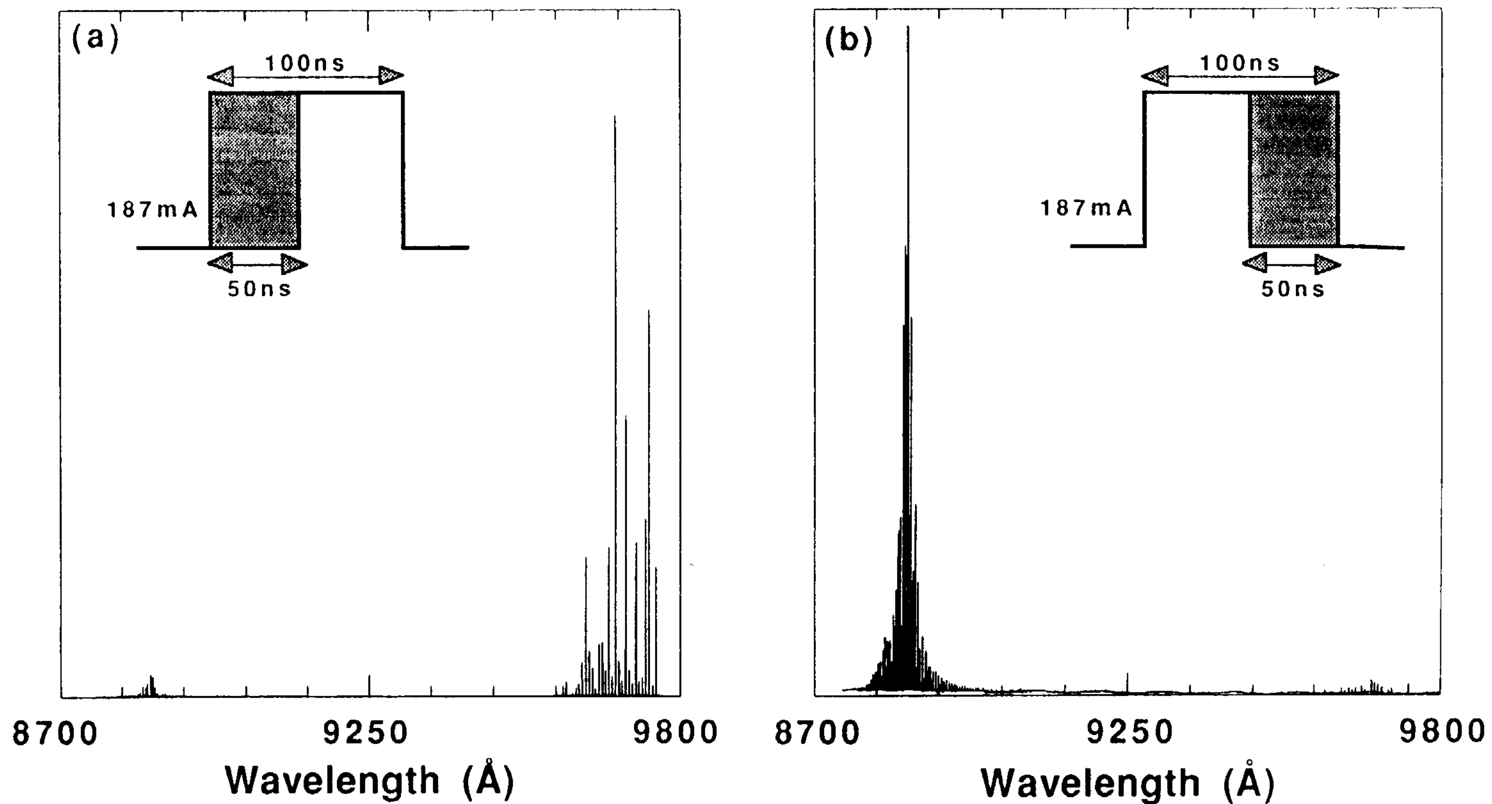

Figure 4.11. Intensity spectra at I = 185 mA for 15 μm x 200 μm sample. (a) 50 ns gate positioned in the first 50 ns of a 100 ns pulse and (b) 50 ns gate positioned in the second 50 ns of the pulse.

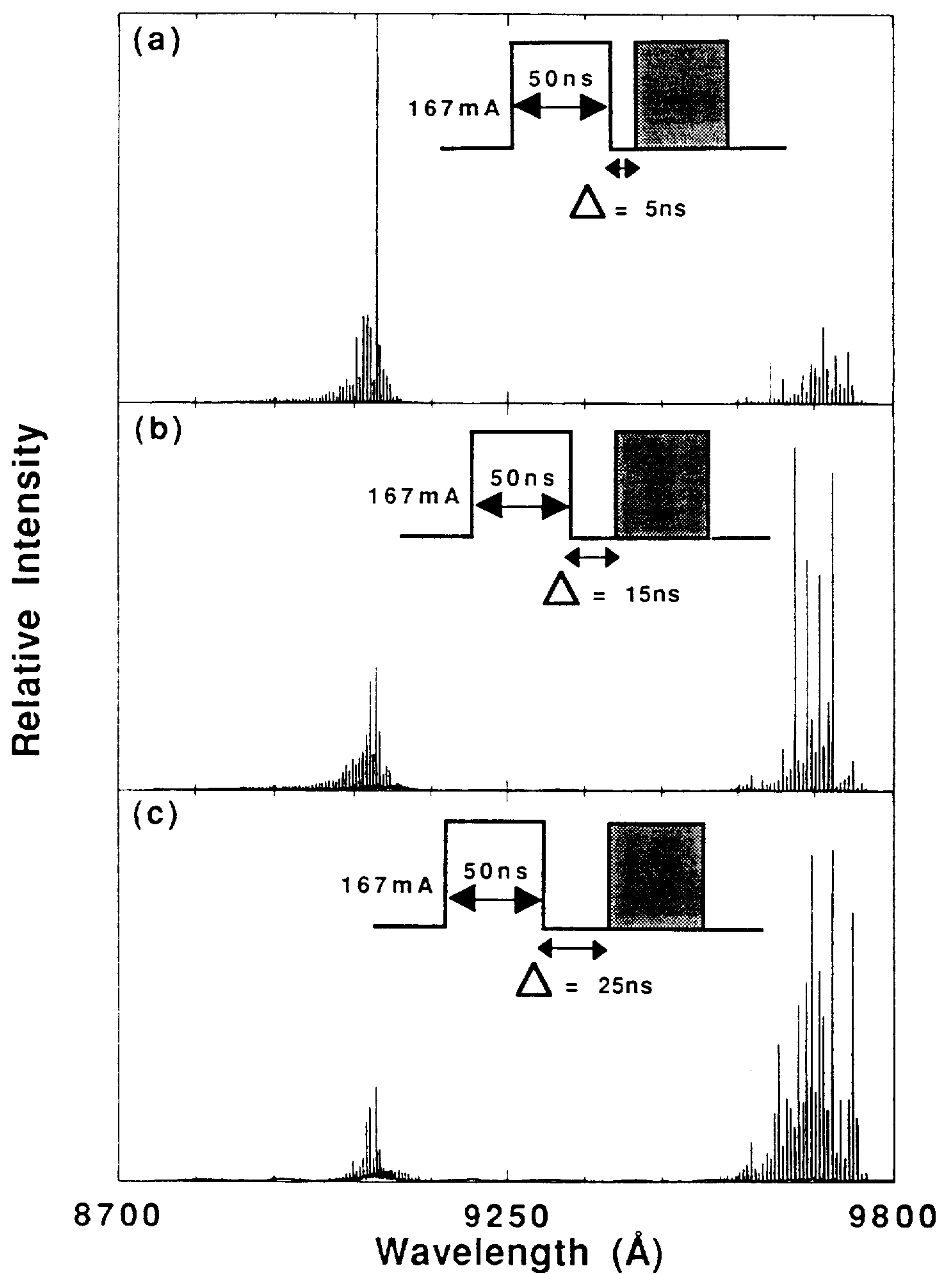

Figure 4.12. Intensity spectra at I = 167 mA for 15 μm x 200 μm sample with 50 ns gate positioned in the second 50 ns of a double pulse, with the separation between the two 50 ns pulses being (a) 5ns, (b) 15 ns and (c) 25 ns.

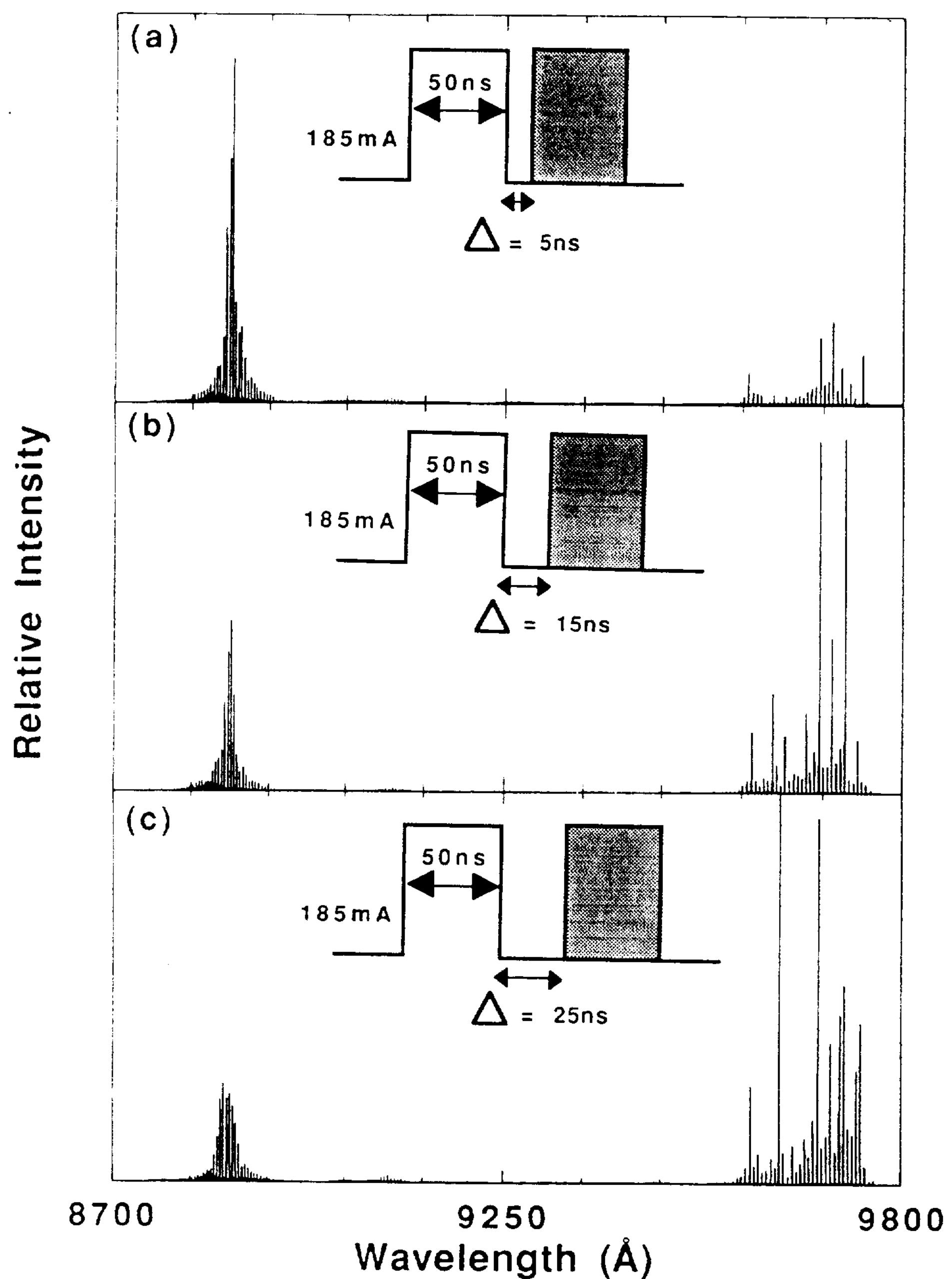

Figure 4.13. Intensity spectra at I = 185 mA for 15 μm x 200 μm sample with 50 ns gate positioned in the second 50 ns of a double pulse, with the separation between the two 50 ns pulses being (a) 5ns, (b) 15 ns and (c) 25 ns.

transition during the first 15 ns of the 100 ns (<25 ns since the shorter wavelength is still present) and then switches to the shorter wavelength (n=2 or barrier) beyond that time.

Earlier works on time-dependent switching of lasing wavelength from the n=1 and n=2 level in the QW in strained-layer InGaAs/GaAs systems[62] and from the n=2 to the n=1 level has been reported in GaAs-AlGaAs[83]. It was observed that the order of switching in the *strained system was opposite* to that of the unstrained system which was explained in terms of the stronger antiguiding behavior[35,36] in the strained system. The carrier induced antiguiding was found to be stronger in the strained system than the thermal waveguide that is a result of thermally induced index increase in the unstrained system. This aspect coupled with an overall temperature rise helps in going from a lower energy transition to a higher energy transition. Note that the pulse widths used in those[62,83] investigations were fairly long ($\approx$ 1.5 μs) and hence it is necessary to include the temperature effects during the pulse to explain the lasing shift in the gain spectrum. The small pulse width (100 ns) and a very low duty cycle (0.1%) employed for the present investigations could preclude such heating effects to influence the switching in our devices. We had earlier seen in Chapter 3 how substantial spectral hole burning inhibited lasing at the longer wavelength and facilitated lasing at the shorter wavelength (device 2A_5). In addition, the spill-over of carriers, with increasing injection level, leads to lateral spatial hole burning (device 2A_8) and contributes to gain nonlinearity by influencing the dielectric constant of the medium. The strength of the antiguiding coupled with nonlinear gain compression mechanisms could thus influence the switching

of lasing wavelength.

4.3.2 Dynamic studies

The spectral investigation (time resolved) showed that the switching of lasing wavelength is a function of time in addition to being a function of the drive level. The bandfilling process is influenced not only by the total number of carriers injected but also by the presence of nonlinearities. To evaluate the extent of such nonlinearities present in the tested devices we investigated the dynamic characteristics on a sub-nanosecond time scale and understand better the observed switching behavior.

4.3.2.1 Device characteristics (15 μm × 600 μm)

Fig 4.14(a) shows the light - current characteristic of the 15 μm × 600 μm device measured in the averaged mode using Tektronix digital photometer. The lasing wavelengths at different injection levels are shown in Fig 4.14(b) Spectrally resolved near field spectra were observed on the TV monitor using the CCD to confirm the presence of longitudinal modes corresponding to wavelength regions of the n=1 (980 nm), n=2 (910 nm) and barrier (885 nm). The device had a threshold of 245 mA (n=1 transition) and saturated in output power fairly quickly and remained so until about 650mA when pronounced kinks were observed coinciding with the appearance and disappearance of n=2 transition as the current was increased. At around 770 mA the barrier transition appeared. At currents above 950 mA the n=2

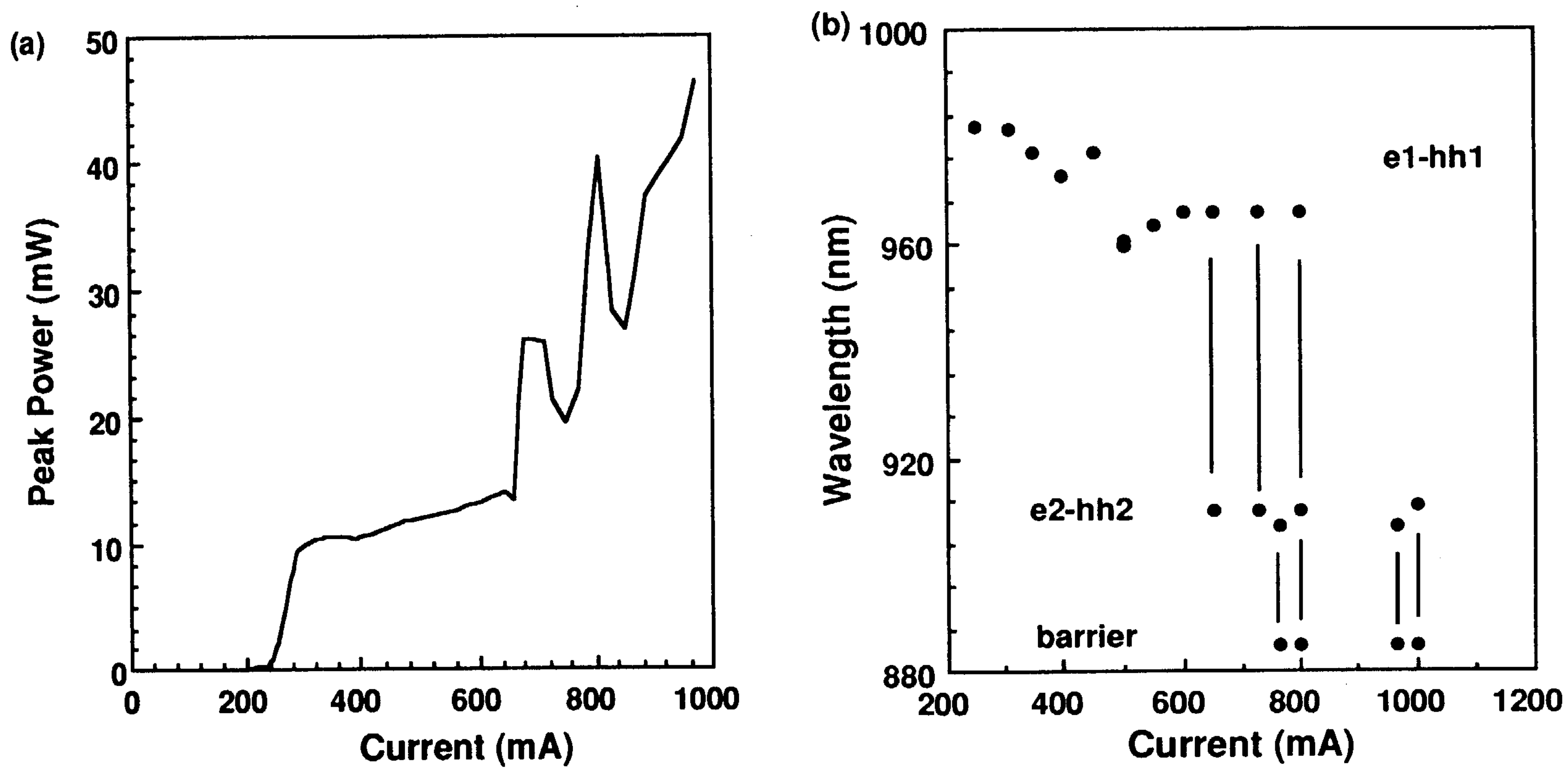

Figure 4.14. (a) The light-current characteristic, and (b) lasing wavelength with drive current for 15 μm × 600 μm sample in pulsed operation. Observed transitions are n=1 (980 nm), n=2 (910 nm) and barrier (885 nm). Vertical lines in (b) indicate "simultaneous" transitions.

transition reappeared and the device also continued to lase in the barrier with the n=1 transition still present.

4.3.2.2 Sub-nanosecond resolved light pulse

Fig 4.15 shows the light pulse recorded with the CSA 803 at the injection levels shown. The laser began to lase with a sequence of pulses separated by about 3 ns. If the current pulse width were to be increased, the light pulse would consist of a train of pulse spikes. The last spike in that train was found to be shifting with time and was also confirmed using the transient digitizer and is probably due to small fluctuations in the current pulse shape. As the current was increased a well defined relaxation damped oscillation (RO) peak began to form with the amplitude of subsequent cycles being successively damped to a larger extent. In addition to the shift of the turn-on delay, the width of the light pulse was found to increase with increase in drive level. This is a consequence of the relatively slow rise and fall times (about <15 ns) of the current pulse (HP214B). It was realized that not only did the current pulse change its width to account for the increase in the width of the light pulse, but also in rise time to give an apparent larger shift of the turn on point.

At higher drive levels (> 760 mA) a new set of seemingly random spikes separated from the first relaxation peak by about 15 ns is observed. In addition to shifting towards the first RO peak by about 8 ns with increased current level, the set of spikes also spreads towards the tail of the pulse. However at 966 mA the spikes disappeared with a small increase in the light

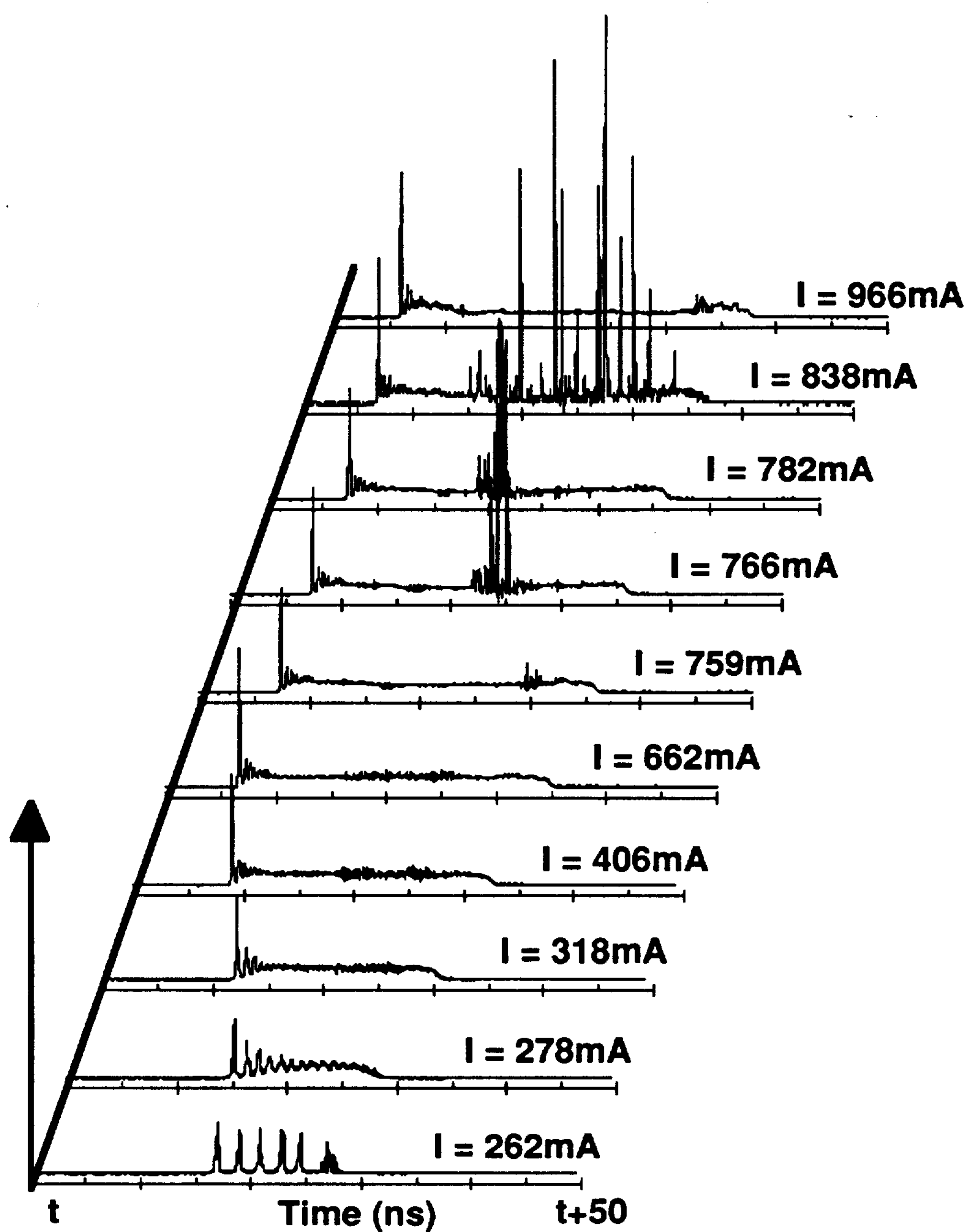

Figure 4.15. Average light pulse traces at different current levels for 15 μm × 600 μm device. Above 759 mA the onset of random lasing spikes is observed clearly separated by about 10 ns or more from the first relaxation oscillation peak.

intensity only at the tail of the light pulse. Comparing with the light-current characteristic (Fig. 4.14) it is possible that the spikes seen at current levels of 766 mA, 782 mA and 838 mA a could correspond to the onset of lasing from the barrier. At around 660 mA the expected changes in the light pulse due to the onset of n=2 transition was not observed. In evaluating the experimental set up, it was noted that with a 15 μm stripe and a 16X microscope objective, the magnified nearfield at the fiber tip exceeds the 125 μm core size by a factor of two. With the modes at this wavelength (910 nm) being higher order lateral modes, very little light could be coupled into the fiber and hence the absence of clearly defined change in the light pulse shape. Note that these waveforms were displayed after "averaging" by the signal analyzer which masks any random fluctuations in the output from pulse to pulse. In order to better understand the behavior on such a pulse to pulse basis, single-sweep waveforms (over a 40 ns interval) were recorded using the transient digitizer as shown for two current levels in Fig. 4.16 (782 mA) and Fig. 4.17 (838 mA) Each of those waveforms, at both current levels, was recorded with a separate trigger and is indicative of the behavior at the particular current level. A 30 ns pulse width for the current was used for these measurements. Some features appear more consistently from pulse to pulse than others. In all curves the first strongly damped RO remains well defined temporarily with not much change in intensity in each pulse as anticipated from Fig. 4.15 . However, the second set of spikes about 10-12 ns later are highly random and showed no phase conservation between pulses. In some traces they might not show up at all. On the other hand, within a single trace they form groups of relatively coherent RO's often building up in intensity and then decaying, sometimes

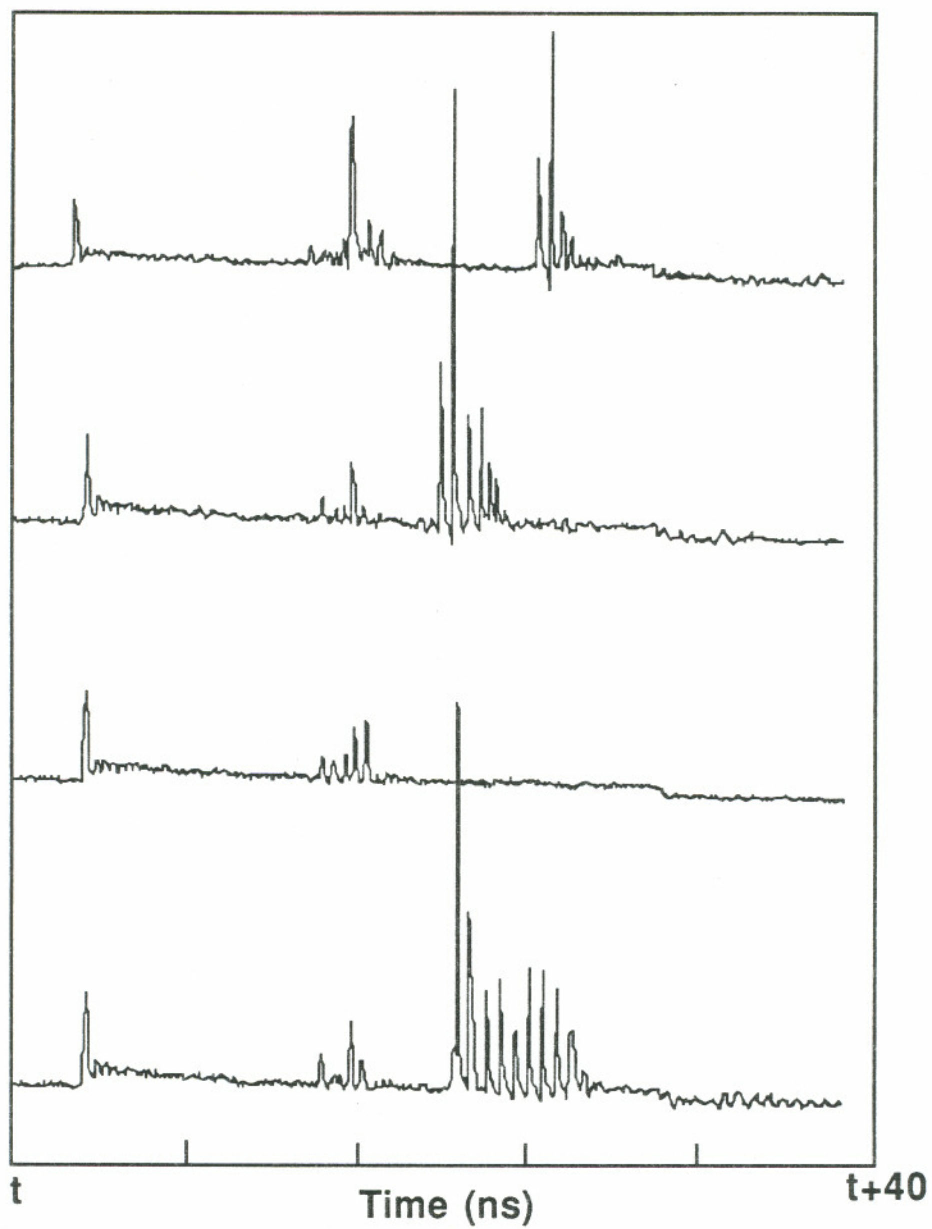

Figure 4.16. Single sweep traces of the light pulse at different triggers for the same current level (782 mA) for 15 μm × 600 μm.

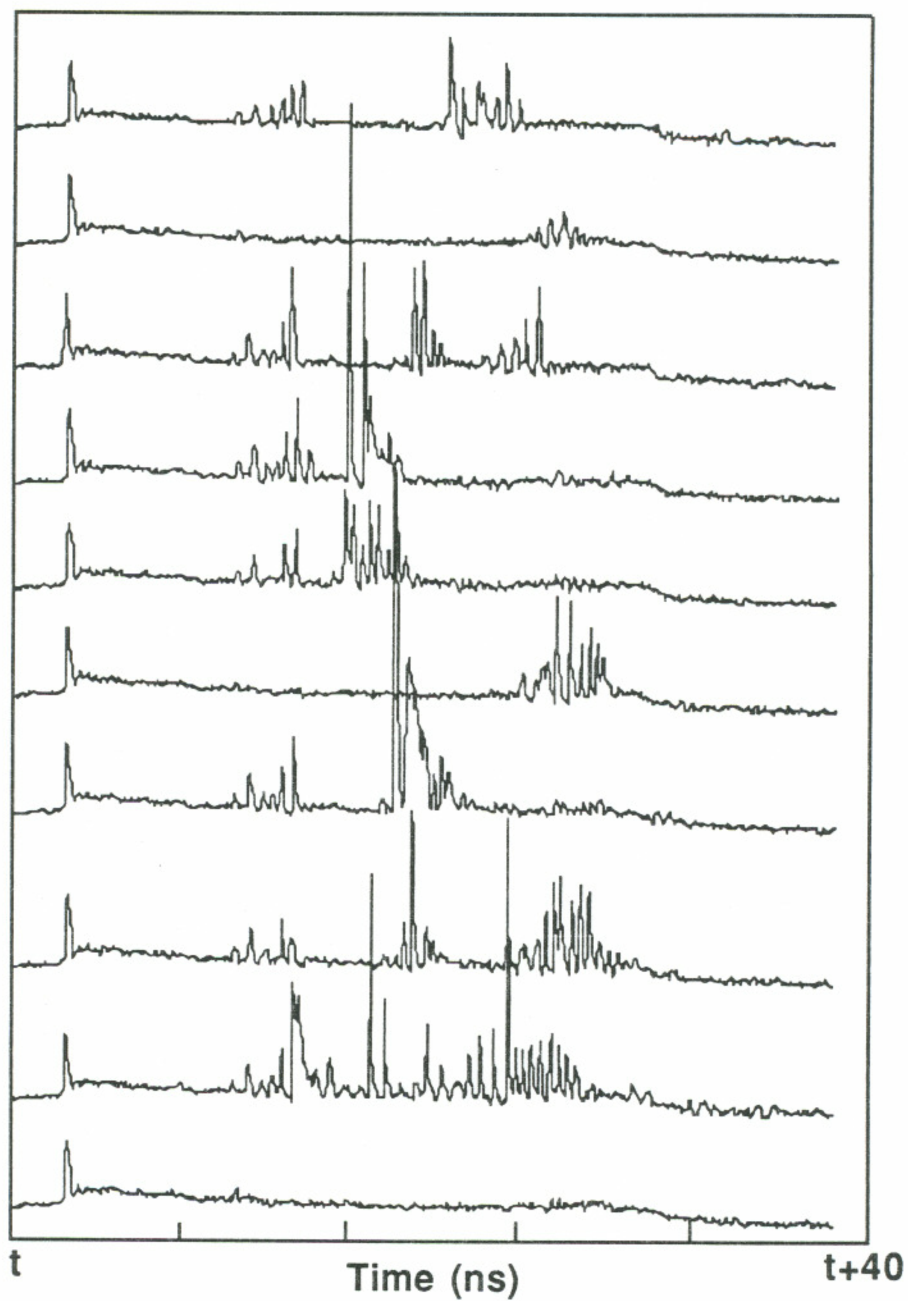

Figure 4.17. Single sweep traces of the light pulse at different triggers for the same current level (838 mA) for 15 μm × 600 μm device.

exhibiting obviously random phase changes. An exponential growth of RO has been attributed to a negative damping rate when there is positive change in net gain with optical intensity[78], leading to self pulsations which has been observed in AlGaAs lasers. The oscillatory spikes appearing in the second half of the light pulse are random in nature both with respect to intensity and temporal distribution. The randomness in the spikes is attributed to the "self-oscillation" that had been observed when the laser switches to the barrier emission (see section 3.4.3) and had been explained in terms of the nonlinear gain profiles in the lateral dimension[72]. The difference in the carrier density distribution and the dielectric constant results in random frequency shifting (chirping) of the modes from pulse to pulse. This frequency shifting between pulses is in a manner consonant with the random nature of the peaks observed in the time domain measurements. At the lower current level of 782 mA, even though the averaged waveform recorded from the CSA 803 did not show a second group of spikes towards the end of the pulse, the SCD 5000 single-sweep waveforms reveal that there indeed appears a second set of oscillation spikes but with a very small probability of occurrence. It is however important to point out that fluctuations in the current pulse shape, if sensitive to such changes, could also lead to the observed random fluctuations in the light waveform, though it did not seem to have affected the first RO peak implying that such variations were not at the beginning of the current pulse.

The spectral measurements (gated) showed that there indeed was a time dependent switching of the lasing wavelength from the longer to the shorter wavelength. The shorter wavelength (n=2 or barrier) appeared after

the first 15 to 20 ns of the 100 ns light pulse. The n=1 was present in the beginning 15 ns with varying intensities. Comparing the results of the spectral investigations to the present sub-nanosecond resolved light pulse measurements, though on different devices, we see a good correlation between the appearance of a second set of spikes clearly separated from the first RO and the onset of lasing at the shorter wavelength. It is of course difficult to pinpoint exactly the shorter wavelength since it is a combination of n=2 (if available) and the barrier transitions. Note also that the analysis is complicated with the randomness (in time) of the light pulse spikes.

4.3.2.3 Relaxation oscillation frequency

The relaxation oscillations (RO) due to the intrinsic resonance in the nonlinear laser system determines the theoretical maximum of the modulation bandwidth. The carrier lifetime at threshold and the photon lifetime[83] essentially determine the oscillation frequency in addition to the photon density beyond threshold. This frequency can be directly measured from the reciprocal of the period of oscillations observed at the beginning of the light pulse using the CSA 803. The Full Width at Half Maximum (FWHM) of the first RO peak as a function of the drive level is shown in Fig 4.18. With the 20 GHz optical sampling head (SD-46) the minimum half widths that can be measured is about 25 ps. The FWHM reduces from 360 ps at around threshold (I_{th} = 245 mA) to around 122 ps at about $2I_{th}$ and remains fairly constant beyond.

For a preliminary understanding of the behavior of the relaxation

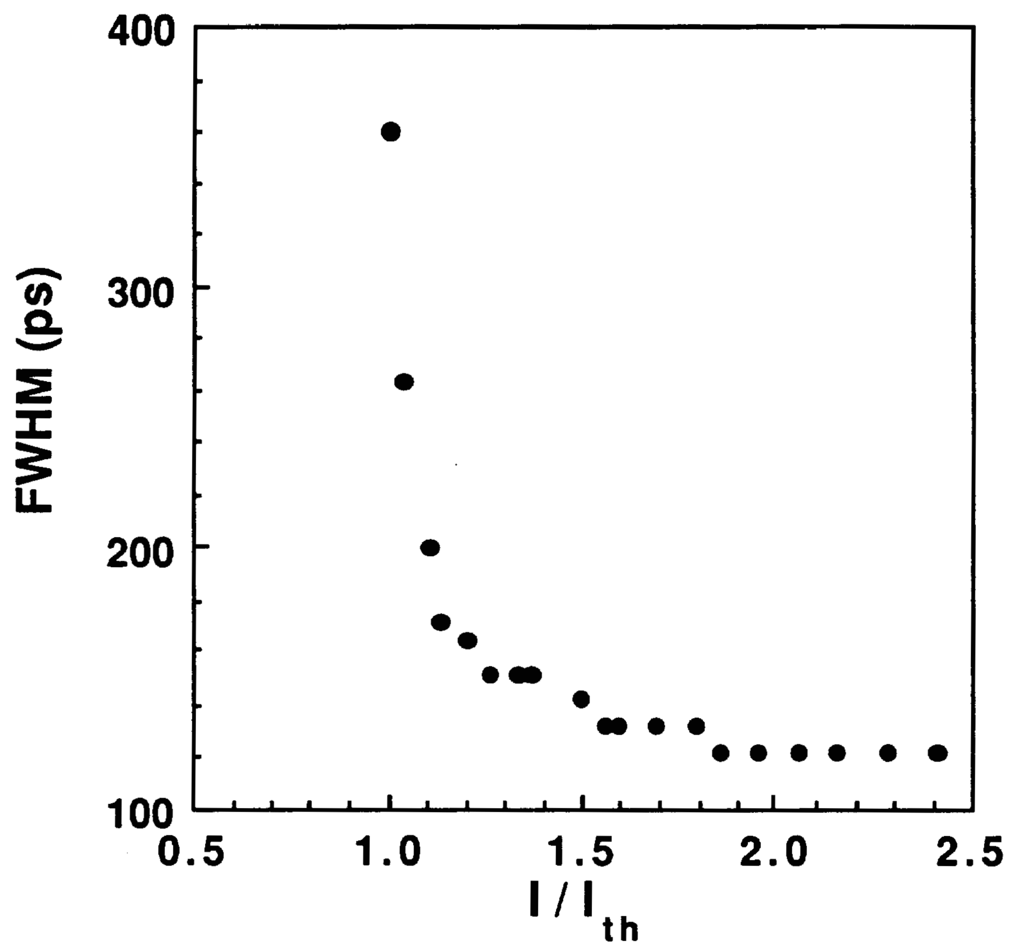

Figure 4.18. The Full Width Half Maximum (FWHM) of the first relaxation oscillation peak (minimum FWHM that can be measured is 25 ps with the 20 GHz SD-46 sampling head; I_{th} = 245 mA, see Fig. 4.14).

oscillation frequency with injected current, a small signal analysis model is used to compare with the experimental results. A more accurate analysis requires a complex large signal model. In the small signal analysis, the frequency of oscillations, f_r, can be relatedto the photon number, S, by the following relation[54] allowing for nonlinear gain:

$$4\pi^2 f_r^2 = \frac{\Gamma^2 v_g^2 g}{V} \frac{dg}{dN} S \left(1 + \frac{S}{g}\frac{dg}{dS}\right) \tag{4.1}$$

where Γ, v_g, V, g, dg/dN, dg/dS are the mode confinement factor, group velocity for the mode, active volume, local gain, local differential gain coefficient with respect to injected carrier density, N, and local differential gain with respect to photon number, S, in the cavity (nonlinear gain contribution). In the above equation the terms containing the difference between the decay rates of the carrier and the photon populations and the change in the spontaneous emission rate with carrier density have been neglected. The gain is allowed to vary with photon number to account for nonlinear effects which can occur due to mechanisms like spectral and spatial hole burning. The photon number is related to the output power, P, from one facet of the laser with equal facet reflectivities, as

$$P = \frac{1}{2} h\nu\, \alpha_m\, v_g\, S \tag{4.2}$$

where $h\nu$ is the energy of the photons and α_m is the mirror loss, from which we can see that

$$S \frac{d}{dS} = P \frac{d}{dP} \tag{4.3}$$

Also, the photon number S can be written in terms of the current beyond threshold as

$$S = \eta_{i,st}\, \tau_{ph} \frac{I - I_{th}}{q} \tag{4.4}$$

where $\eta_{i,st}$ is the stimulated internal quantum efficiency and τ_{ph} is the photon lifetime. However, one has to be cautious in applying this equation when power saturation effects are observed. Equation (4.4) would then lead to the situation of a "variable" I_{th}, $\eta_{i,st}$ or τ_{ph} to account for a constant S.

Equation (4.1), along with equations (4.3) and (4.4) can thus be rewritten in terms of the current as, noting that $\tau_{ph}^{-1} = v_g\, \Gamma\, g$,

$$f_r^2 = \frac{1}{4\pi^2} \left(\frac{\Gamma v_g}{qV} \frac{dg}{dN} \right) \eta_{i,st}\, (I - I_{th}) \left(1 + \varepsilon P \right) \tag{4.5}$$

or using equation (4.2) and (4.4) in terms of power as

$$f_r^2 = \frac{1}{4\pi^2} \left(\frac{2}{Vh\nu\, \tau_{ph}\, \alpha_m} \right) \Gamma \frac{dg}{dN} \left(1 + \varepsilon P \right) P \tag{4.6}$$

where, the nonlinear gain coefficient, ε, is

$$\varepsilon = \Gamma\, v_g\, \tau_{ph} \frac{dg}{dP} \tag{4.7}$$

Thus, the presence of non-linear gain could substantially modify f_r^2. Depending on the strength and sign of the gain nonlinearity and a possible associated change in the value for dg/dN there could be an increase or decrease in f_r^2 or, equivalently, a gain enhancement or gain suppression effect. Fig 4.19 shows the dependence of f_r^2 on the output power above threshold. The relaxation oscillation frequency as observed in the light pulse for currents where the device operates only from the n=1 level is considered. Up to power levels of about 10 mW there is a non-linear dependence as shown. Note also that the output power saturates in the light-current characteristic at this power (Fig. 4. 14a). Although the power increases more or less linearly with current in this range, f_r^2 does not. The observed behavior does imply that the gain varies with power, i.e., $\varepsilon \neq 0$, and in fact has to be > 0 according to equation (4.6) . With further increase in current only a small increase in power output is seen but there is a sudden drastic increase in f_r^2 (Fig. 4.19) indicating that the nonlinearity has suddenly increased even more. At large enough drive levels ($\approx$ twice threshold), the resonance frequency begins to roll over indicating substantial gain compression with an apparent change in sign for ε. The output power, though, has increased only to about 13 mW. This saturation behavior of the resonance frequency has been theoretically investigated by Arakawa *et al.*[85] to estimate the nonlinear gain that is enhanced in quantum well lasers due to the quantum confinement of carriers. The probable cause as suggested by them is the reduction in differential gain due to the gain compression.

Many aspects of the static and dynamic characteristics of semiconductor lasers are influenced by the differential gain. It is an important parameter in

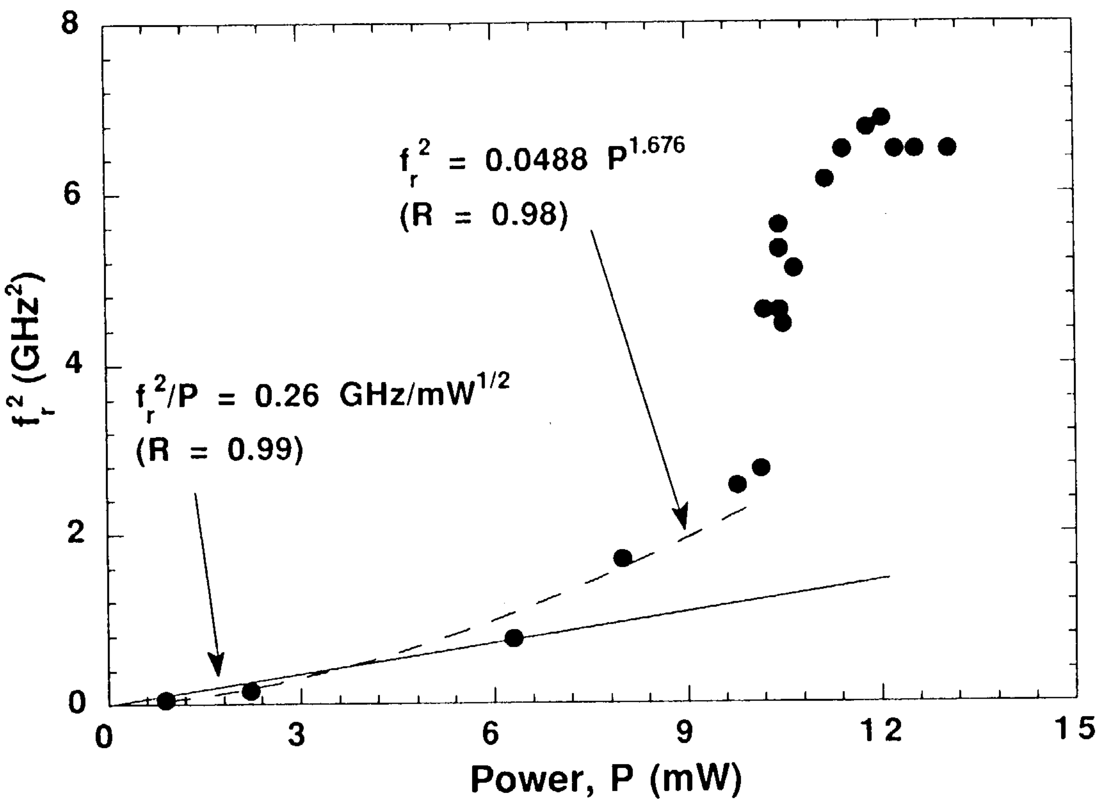

Figure. 4.19. Power dependence of f_r^2 for the 15 μm × 600 μm (2A_34 in Table 3.1a) device. The fit obtained at the different regions are shown (R is the correlation for the fit).

determining the resonance frequency, equation. (4.5). Thus the expected enhancement of the differential gain of strained-layer systems[37,38] should theoretically increase the modulation bandwidth. However, the population of higher subbands was found to offset the expected enhancement in differential gain in single QW lasers compared to Double-Heterostructure (DH) lasers[86]. In analyzing the effect on modulation dynamics due to this state filling[87], it was found that this bandfilling resulted in a lower differential gain and possibly a higher transparency current. It is well known that, in practice, the gain is not clamped beyond threshold since with increase in laser power, several other phenomena such as spatial (both laterally and longitudinally) and spectral hole burning begin to influence the lasing characteristics. These mechanisms result in contribution to the nonlinear gain in quantum well lasers and have been shown, theoretically, to be significant in quantum well lasers[85] because of the quantum confinement of carriers. Furthermore, in strained-layer systems operated at high injections, it has been theoretically shown[88] that the linear gain saturation due to the reduced density of valence states is enhanced resulting in a lower value for the differential gain when compared to the lattice matched case. The more pronounced saturation of the linear gain in these strained structures accounts for the enhanced reduction of the differential gain at increased injection and thus the reduced relaxation oscillation frequency which limits the maximum bandwidth attainable[89,90].

From Fig. 4.19, considering the initial linear dependence of f_r^2 on P (first three points and (0,0)) we get a slope of 0.26 GHz/mW$^{1/2}$. For the 15 μm × 600 μm device, Γ = 0.02, $v_g = 8 \times 10^9$ cm/s, active volume V = 6.75×10^{-11} cm^3 , λ =980 nm, α_m =20 cm^{-1} . We had earlier determined that the internal

loss, α_i, for the broad area devices (50 μm) with insignificant lateral losses to be 8.9 cm $^{-1}$ (section 3.3.3, page 41). Assuming α_i to be essentially determined by lateral loss thus allowing an inverse linear scaling with stripe width (similar to the inverse dependence of the mirror loss with cavity length), we get α_i for the 15 μm device to be 29.7 cm^{-1} . The total optical loss, α_t, is 49.7 cm^{-1} giving a photon lifetime, τ_{ph}, of 2.5 ps. Thus, from equation (4.6), neglecting the nonlinear coefficient ($\varepsilon = 0$), we get for dg/dN a value of 0.46 × 10^{-16} cm^2 which is an order of magnitude smaller than typically reported values[25] . This indicates that linear gain saturation is present when the device is still operating from the n=1 level in the quantum well at high injections.

To understand the observed behavior of f_r^2, the local differential gain with respect to carrier density, dg/dN, and with respect to power, dg/dP, need to be estimated at the various power levels using equation (4.6) from the measured resonance frequency. For convenience equation (4.6) can be written relating f_r^2 to the output power as:

$$f_r^2 = G_o P \tag{4.8}$$

where,

$$G_o = \frac{1}{4\pi^2}\left(\frac{2\,\Gamma}{V\, h\nu\, \tau_{ph}\, \alpha_m}\right)\frac{dg}{dN}(1+\varepsilon P) \tag{4.9}$$

The parameter G_o has units of $(s^2 mW)^{-1}$, where the power is in mW. As mentioned earlier, we should see the expected enhancement or suppression depending on the strength of the nonlinearity. Fig. 4.20 is a plot of this

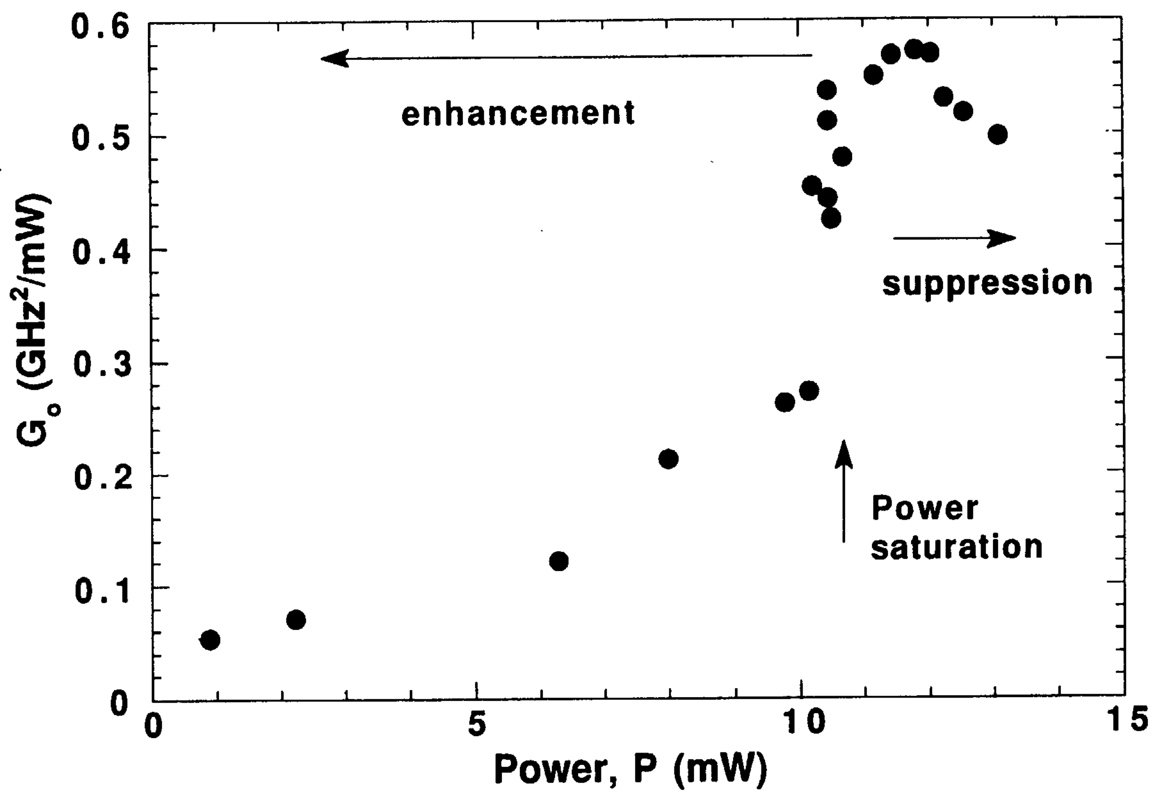

Figure 4.20. Variation of the parameter G_0 with power. Note that this parameter includes the gain dependence on power. Assuming a constant dg/dN, the observed behavior refers to gain enhancement when dg/dP >0, and gain suppression when dg/dP<0 .

parameter with output power as determined from the measured resonance frequency. G_0 starts to increase by a factor of 3 and further continues to increase rapidly before power saturation begins just beyond 10 mW. This is clearly indicative of gain enhancement rather than gain compression. This confirms our contention that ε is > 0, i.e., gain increases with power.

Mechanisms such as saturable absorption and lateral hole burning, with a shift to a higher order lateral mode, that have been suggested[77,78,80] lead to this instability condition of $\varepsilon > 0$. This has been observed in gain-guided AlGaAs lasers[78] which exhibited self pulsing. A change in the lateral waveguiding is the result of a change in the lateral refractive index distribution due, in turn, to a change in the lateral carrier distribution with increased power. This may eventually result in an increased modal gain with increasing power. Additionally, it is possible to have emission in higher order lateral modes. With good coupling to the injected carrier distribution the fundamental mode reaches threshold first and it's gain is then clamped at threshold. At higher drive levels, the gain depletion near the center of the stripe and a simultaneous enhancement near the stripe edges tries to maintain the overall gain constant. At some higher drive level when the higher order mode begins to couple effectively to the new gain distribution the mode(s) would now begin to share the power with the fundamental. Another possibility is when there is an axial inhomogeneity consisting of amplifying and absorbing sections, where again an increase in gain with power may result. Higher optical power results in reduced carrier density in the amplifying regions and larger carrier density in the absorbing regions due to generation of carriers by the photons. Thus, a simultaneous reduction in

gain in the amplifying regions and a loss reduction in the absorbing regions, with increased power, is possible. The net gain would then increase with increasing power for the case of the loss reduction being larger than the gain reduction.

With saturation of output power, G_0 reduces after reaching a maximum. Although the reduction is qualitatively in agreement with the theoretical analysis of Arakawa *et al.*[85] which showed that there is a drastic reduction in the differential gain with increasing intensities, G_0 maps a combination of $(1+\varepsilon P)$ and dg/dN. But with ouptut power saturation, εP would not change and hence the reduction could be attributed to a reduction only in dg/dN. Their calculation also showed that the quasi-Fermi levels for maximum differential gain vary with changes in the light intensity.

The observed tendency of the resonance frequency to attain a maximum due to the gain compression has been suggested in some phenomenological models of gain compression[91-93], although the predicted saturation behavior has not been explained through any physical mechanisms. Spectral hole burning mechanisms have been suggested as the dominant source of such gain suppression[94-96] though recent theoretical work has indicated that carrier heating effects are five times stronger than spectral hole burning[97]. As a result of the gain compression effects, increased lateral losses are observed in stripe-geometry strained layer lasers[35], forcing the quasi-Fermi levels to be pushed farther apart. Carrier spill-over effects eventually become dominant. Sharfin *et al* [90] have suggested the necessity of considering the spill-over and transport of carriers between the QW and the surrounding higher bandgap barrier and confinement layers. The lateral leaky

losses would also influence the lateral spatial hole burning mechanisms leading to higher nonlinear gain compression in such devices. The earlier mentioned nonuniform lateral gain profile, in addition to increasing nonlinearities, also influences the onset of "self-oscillation" observed in most of these devices.

From Fig. 4.19 we see that the RO frequency saturates completely beyond around 12 mW corresponding to a current level of $I-I_{th} = 0.3$ A, i.e., around I = 600 mA. Comparing with the light-current characteristic curve (Fig. 4.14) it is clear that just beyond this current, i.e., 660 mA, is the onset of lasing at the n = 2 transition. Due to the poor coupling of light into the fiber, as the device lases in a higher order lateral mode when lasing at n = 2, it is not possible to show a direct correlation between the onset of random lasing spikes in Fig. 4.15 and the roll off in the resonance frequency in Fig. 4.19 at this current level. Note also that we are now able to reconfirm the earlier results from our gain measurements obtained with device 2A_5 (15 μm × 355 μm : section 3.4.3.1 ; Fig. 3.20) that the onset of lasing at the shorter wavelength is induced by the presence of gain compression due to spectral hole burning at the longer wavelength which is also the very reason for the observed saturation in the resonance frequency in the 15 μm × 600 μm device.

4.3.2.4 Damping

The observed nonlinear relationship between f_r^2 and P indicated the existence of an instability condition of $\varepsilon > 0$ due to lateral hole burning or saturable absorption at power levels below 10 mW. This implies that the

damping of the relaxation oscillations is being compensated by a "de-damping" effect. This "de-damping" effect could eventually lead to an exponential growth in the relaxation oscillations leading to self pulsing. Fig 4.15 shows that at the lower current level (262 mA) the laser is indeed exhibiting such a pulsing behavior before settling into the damped relaxation oscillation at higher drive levels. The damping or the decay rate of the relaxation oscillations, Γ_r, can be evaluated by fitting the intensity of the peaks to an exponential function of the form $\exp(-\Gamma_r\ t)$. It was observed from the light pulse measurements that the first peak was unusually strong in intensity (Fig. 4.15) and the subsequent peaks were considerably smaller in amplitude making the fit difficult. It was then decided to fit the first two peaks and the subsequent peaks separately. The decay rate evaluated from the first two peaks at each current level is indicated by dark circles and the decay rate measured from the subsequent peaks is indicated by open circles in Fig. 4.21 . It should be pointed out that the f_r^2 value at each current that was used in Figs. 4.19 and 4.20 was determined from an average for the period of the peaks subsequent to the first strong spike in the relaxation oscillations. Hence a qualitative comparison can only be done between the behavior of f_r^2 with P in Fig 4.19 and that of Γ_r with P as represented by open circles in Fig. 4.21. In addition, while all points in Fig. 4.19 were obtained before the n=2 transition appeared, current levels beyond this has also been used in Fig. 4.21 where the power was evaluated from the average peak power in the light pulse.

Plotting the decay rate (dark circles) with output power shows that at power levels below 10 mW there is a nonlinear power dependence. At around 10 mW, where the output power saturates (see Fig. 4.14a), the

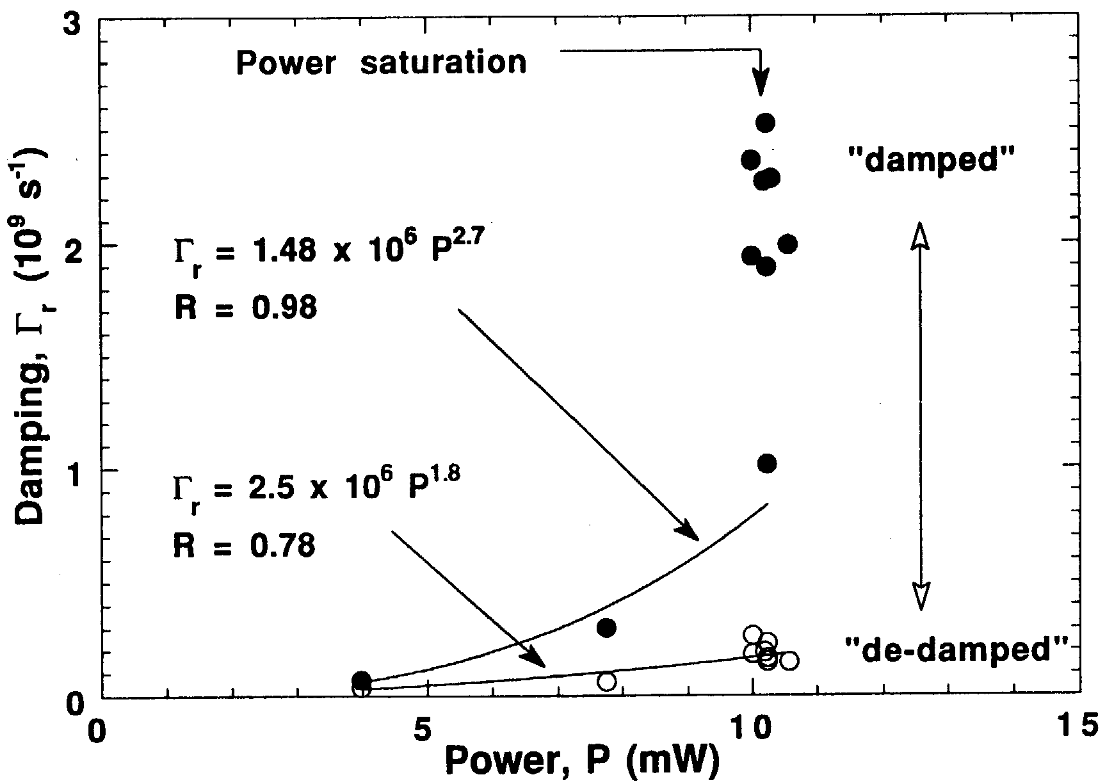

Figure 4.21. Power dependence of the damping, Γ_r , determined at current levels shown in Fig. 4.15 . The dark circles is the decay rate for the first two peaks and the open circles are for subsequent peaks of the RO, after turn on, at each current level.

damping increases drastically. The value for the power used in this plot is not the intensity in the spike but the average peak power in the light pulse immediately after the oscillations. From the light pulses shown in Fig. 4.15, it is also clear that the intensity of the spike does not increase much for currents beyond 662 mA. Hence there is only a small reduction of the "de-damping" effect.

From the small signal analysis the damping rate can be related to the power, neglecting the spontaneous emission term, as[54]

$$\Gamma_r = \frac{1}{2}\left(\frac{1}{\tau_e} + N\,\frac{d(1/\tau_e)}{dN} + \frac{\Gamma v_g}{V}\frac{dg}{dN}P - \Gamma\, v_g \frac{dg}{dP}P\right) \qquad (4.10)$$

where τ_e is the carrier lifetime. With increasing power, both dg/dN and dg/dP (and $d(1/\tau_e)/dN$ with increasing N) can vary, either enhanced or suppressed, and influence the damping rate, Γ_r. When $dg/dP > 0$ (gain enhancement) at lower power levels, this would reduce the overall damping rate (increase in f_r^2). At higher power levels, when power saturation sets in, gain compression ($dg/dP < 0$) effects are present. This increases Γ_r (would eventually result in saturation of f_r^2). Such a behavior is clearly observed for the dark circles

For the subsequent set of peaks in the relaxation oscillations (open circles in Fig. 4.21), a smaller power dependence at all power levels is seen. The large initial drop in the amplitude of the peaks in the relaxation oscillation reduces the influence of power on the "de-damping" effect. This shows that the "de-damping" effect exists at all power levels. Thus Γ_r continues to remain considerably small for all power levels. This implies that

εP is almost independent of power for the "open circles", but decreases considerably with P for the "closed circles" in Fig. 4.21 . This, however, is inconsistent with the observed P dependence for f_r^2, except when f_r^2 saturates (Fig. 4.19) thus requiring a more complex strong signal analysis.

Chapter 5

DEVICE CHARACTERISTICS UNDER QUASI-DOUBLE-HETEROSTRUCTURE OPERATION

5.1 Introduction

The presence of strain in strained-layer systems has been theoretically shown to improve dynamic response and noise characteristics[38]. Extremely high modulation bandwidths (up to 90 GHz)[37] have been predicted based on theoretical estimates of the differential gain. Apart from the enhanced gain, it is also felt that despite a compensating increase in the carrier dependence of the real part of the refractive index, a reduced linewidth enhancement factor, α, could also result. Ghiti *et al.*[38] report that a two thirds reduction in α can be expected. Ohtoshi *et al.*[98] predict an α value as low as 0.8 based largely on the expected enhancement of the differential gain. Rideout *et al.*[25] have measured MOVCD grown InGaAs-GaAs-AlGaAs strained-layer QW buried heterostructure lasers with a 4.8 nm InGaAs quantum well and a lasing wavelength near 1.07 μm . They show that the values for dg/dN and dn/dN are significantly enhanced for the strained versions and report an α value of approximately 2 at a carrier density of 5×10^{18} cm^{-3} and with minimum of 1.7. These improvements are a consequence of the modification of the band structure due to strain and quantum effects.

However, a factor which is sometimes overlooked for QW lasers is linear gain saturation, which causes the differential gain to decrease at high injected carrier densities. In addition, the increase in the carrier induced change in the real part of the refractive index could result in a higher α than the theoretical estimates of Ohtoshi *et al.* [98]. To overcome the reduction in the differential gain due to linear gain saturation when operating from the first energy level in the QW, it is possible to increase the loss by a suitable amount to operate the laser at the second energy level of the QW and achieve an enhancement in the differential gain. Experimental[99] work in lattice matched GaAs/AlGaAs SQW lasers has shown that there is a 55% increase in resonance frequency due to the decrease in the photon lifetime along with a higher differential gain as a consequence of increased loss shifting operation to the second quantized state.

As seen in Chapter 4, in addition to linear gain saturation which is further enhanced when operating at high injections, the lasers also exhibited gain dependence on output power when operating from the n=1 level in the quantum well. This leads to a nonlinear behavior of the relaxation oscillation frequency with power. The presence of the nonlinear gain mechanisms forces the device to shift to shorter lasing wavelengths with higher losses which could prove helpful in terms of increasing modulation bandwidth. Theoretical[100] work on lattice matched $In_{0.53}Ga_{0.47}As/InP$ SQW laser showed that there is a reduced nonlinear gain contribution when lasing from the second quantized state accompanied with a higher differential gain as compared to lasing from the first quantized state. With reasonably high losses, substantial carrier leakage out of the active layer into the surrounding

barrier regions results in switching of lasing emission from the quantum well to the barrier. Of particular interest is then the behavior of such a strained-layer QW laser, due to linear gain effects, at these extremely high injection levels with lasing exclusively from the barrier. The losses in the cavity can be suitably increased by choosing a short cavity (say, 200μm : high mirror loss) and a narrow stripe width (say, 5μm : large lateral loss). The separate confinement QW structure would then operate in a quasi-double-heterostructure (quasi-DH) mode with a possible positive influence superimposed due to the strain in the InGaAs QW region. Thus, the question arises if the increase of the Fermi energy levels in such a high injection condition could still provide a reduced α. This chapter reports the experimentally determined spectral variation of the differential gain, differential index and hence the dispersion of α for narrow-stripe InGaAs/GaAs separate-confinement heterostructure single-quantum-well (SQW) gain-guided lasers operated under high loss conditions at the barrier wavelength in a quasi-DH mode.

5.2 Device Structure and Threshold Characteristics

The schematic representation of the epitaxial layers in the strained-layer SQW laser structure is as shown before (see Fig. 3.1). The layers were grown by Molecular Beam Epitaxy (MBE) and processed as described elsewhere[35]. The stripe width selected was 5 μm and the cavity length about 200 μm ensuring high lateral and longitudinal optical losses necessary for quasi-DH operation[35,48]. The laser operated in a multilongitudinal mode and

in a single transverse mode with a longitudinal mode spacing of 4.15 Å. The substantial number of longitudinal modes observed above threshold is contrary to gain-guided unstrained GaAs/AlGaAs QW lasers which often tend to oscillate in a single longitudinal mode for smaller stripe widths. This has been attributed to the increased lateral loss due to the stronger antiguiding in the strained QW laser[35].

The threshold was fairly high (≈ 77 mA, see Fig 5.1.) as a result of the large optical losses and the laser operated at 877 nm (12.6 °C), close to GaAs emission. The combination of a narrow stripe width and a relatively short cavity length obviously provides large enough losses in this case to require sufficient quasi-Fermi level separation for carrier spill-over and lasing at the barrier wavelength. This contention is supported by the fact that the observed threshold current, despite of its high value, is still substantially lower than that reported for an equivalent device with a longer cavity, viz. 155 mA for 400 μm cavity length[35], thus exhibiting the normal cavity-length dependence of threshold as expected for a standard DH laser. Additionally, we tested some broad-stripe lasers (50 μm wide) with the shorter length of 200 μm fabricated from the same epitaxial wafer: in one particular case, when raising current, we observed below threshold gain initially at 930 nm wavelength, but subsequently, at currents close to a very high threshold of 230 mA, substantial gain also at around 880 nm, however, not yet sufficient for lasing; this clearly indicates the beginning of spill-over into the barrier even in this broad-stripe device with it's lower lateral losses. Note that broad area (50 μm), short cavity (200 μm) devices from the wafer processed here did lase at the longer wavelengths as described in chapter 3. The increase in threshold current with

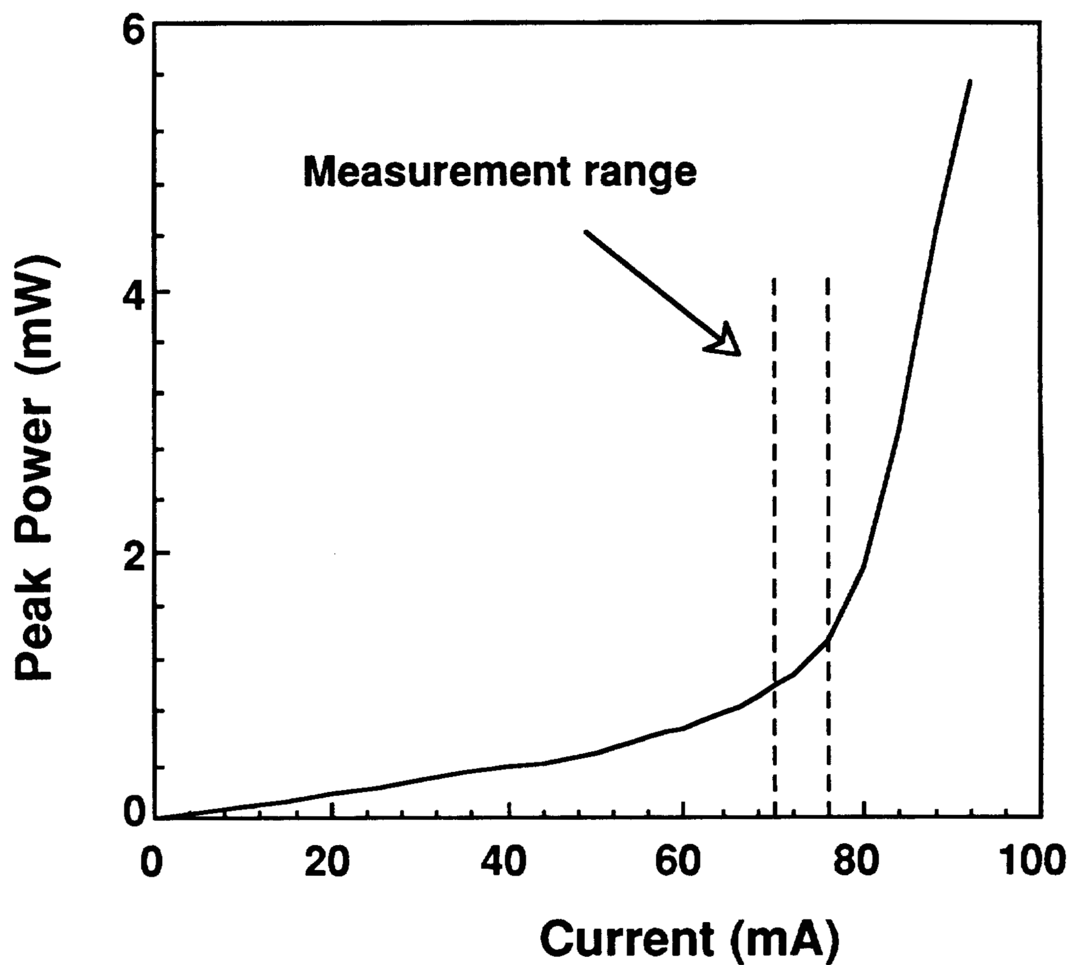

Figure 5.1. Light-current curve for 5 μm × 200 μm with the current range chosen for gain measurements indicated by vertical lines (dashed).

stripe width observed at the shorter cavity length is similar to the dependence expected for standard DH lasers and contrary to the anomalous stripe width dependence of strained-layer InGaAs/GaAs SQW lasers with longer cavity length[35]. It is interesting to note in this context that a more dramatic increase of threshold current towards shorter cavity length has been observed for broad-stripe strained-layer InGaAs/GaAs SQW lasers[48] as compared to their unstrained GaAs/AlGaAs counterparts[49], once again suggesting, in case of the strained-layer, a Fermi level separation at threshold approaching the condition for carrier spill-over into the GaAs guide layers. We conclude that the strained-layer InGaAs/GaAs SQW device selected for the measurements lased under high enough injection to provide quasi-DH operation near threshold and a substantial influence on the linewidth enhancement factor might be expected in such an operation.

5.3 Experimental Technique

The linewidth enhancement factor, α, which characterizes the linewidth broadening due to fluctuations in the carrier density altering the refractive index, is a key parameter that determines the performance of semiconductor lasers both under CW operation and under high frequency modulation[101,102]. This factor α is proportional to the ratio of the change in the refractive index with carrier density (dn/dN) to the change in gain with carrier density (dg/dN). α can be expressed conveniently in terms of the change in internal mode gain ($G_i = \Gamma g$; Γ is the gain confinement factor) and the wavelength shift ($d\lambda$) of the Fabry Perot cavity modes with change in

the injected current (dI) below threshold as[103],

$$\alpha = \frac{2\pi}{\Delta\lambda}\left(\frac{d\lambda/dI}{d(G_iL)/dI}\right) \tag{5.1}$$

where $\Delta\lambda$ is the Fabry-Perot mode spacing for a cavity of length L.

The technique to measure the α parameter was to observe the spectral shift of individual Fabry-Perot modes of the laser and to calculate the gain change with injection level from their peak-to-valley ratios[70]. The experimental set up that was used in this investigation is similar to the spectral measurement set up shown earlier (see section 3.4), but a chart recorder was used to record the spectra at the different injection levels. The laser was operated pulsed (pulse width 200 ns, 5 kHz repetition rate) to minimize heating effects. The laser mount was temperature controlled at 12.6 °C. The mode spectra were measured by passing the emission through a SPEX 1704 one meter grating spectrometer to a photomultiplier cooled to -100 °C, and conditioned using an EG&G box car averager with a Model 165 gated integrator and a chart recorder. A CCD camera and a TV monitor was used for initial alignment of the laser with the grating spectrometer's input and output slits. The current range was chosen close to threshold and was limited at the lower end by noise and at the higher end by the onset of lasing. Spontaneous emission spectra were plotted at 1 mA current intervals to enable unambiguous identification of the shifting laser modes.

5.4 Results

5.4.1 Differential Gain

The modal net gain, G, was obtained from the depth of modulation in the spontaneous emission intensity as before (section 3.4.3). In the limited current range studied we may assume α_i to be a constant and thus: $dG/dI = dG_i/dI$ allowing us to replace G_i by G in eqn. (5.1). Figure 5.2 shows the mode spectrum below threshold at various current levels as indicated. A shoulder on the long wavelength side of the mode was found to be dependent on the current pulse width but not with amplitude and thus not caused by higher-order lateral mode excitation. The shoulder is undesirable since it could affect the estimation of the true ratio, r (see section 6 below). Figure 5.3 presents the gain length product, GL, as a function of wavelength at three current levels. It was found to be approximately parabolic and was thus fitted with a standard equation $[G(\lambda) = G_0 - ((2 / \Lambda)(\lambda - \lambda_0))^2]$ where G_0, λ_0 and Λ are fitting parameters. There is essentially no appreciable shift of the spectral gain peak with current towards shorter wavelengths which would be expected due to band filling; such a shift is generally observed in DH lasers[104]. The net gain was found to vary linearly with current as shown in Fig 5.4 at the gain peak and did not show any indication of linear gain saturation effects due to the high injection levels as would be expected in a QW structure, a fact consistent with our assumption of quasi-DH operation. However, the relatively narrow current range available may not be large enough to allow for a possible

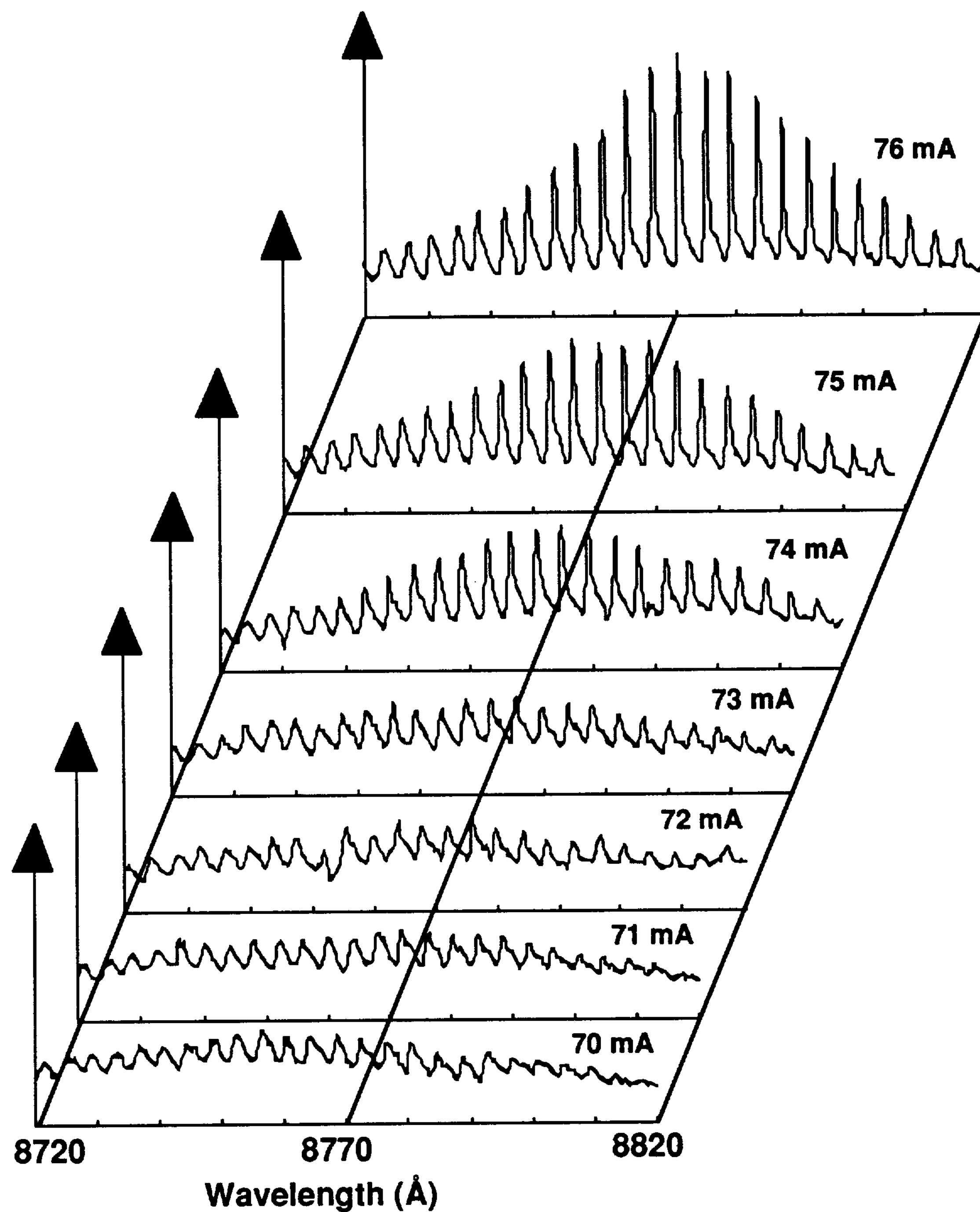

Figure 5.2. Evolution of the mode spectrum with increasing drive level. The intensities were normalized to a same but arbitrary maximum and is indicated by the vertical arrow.

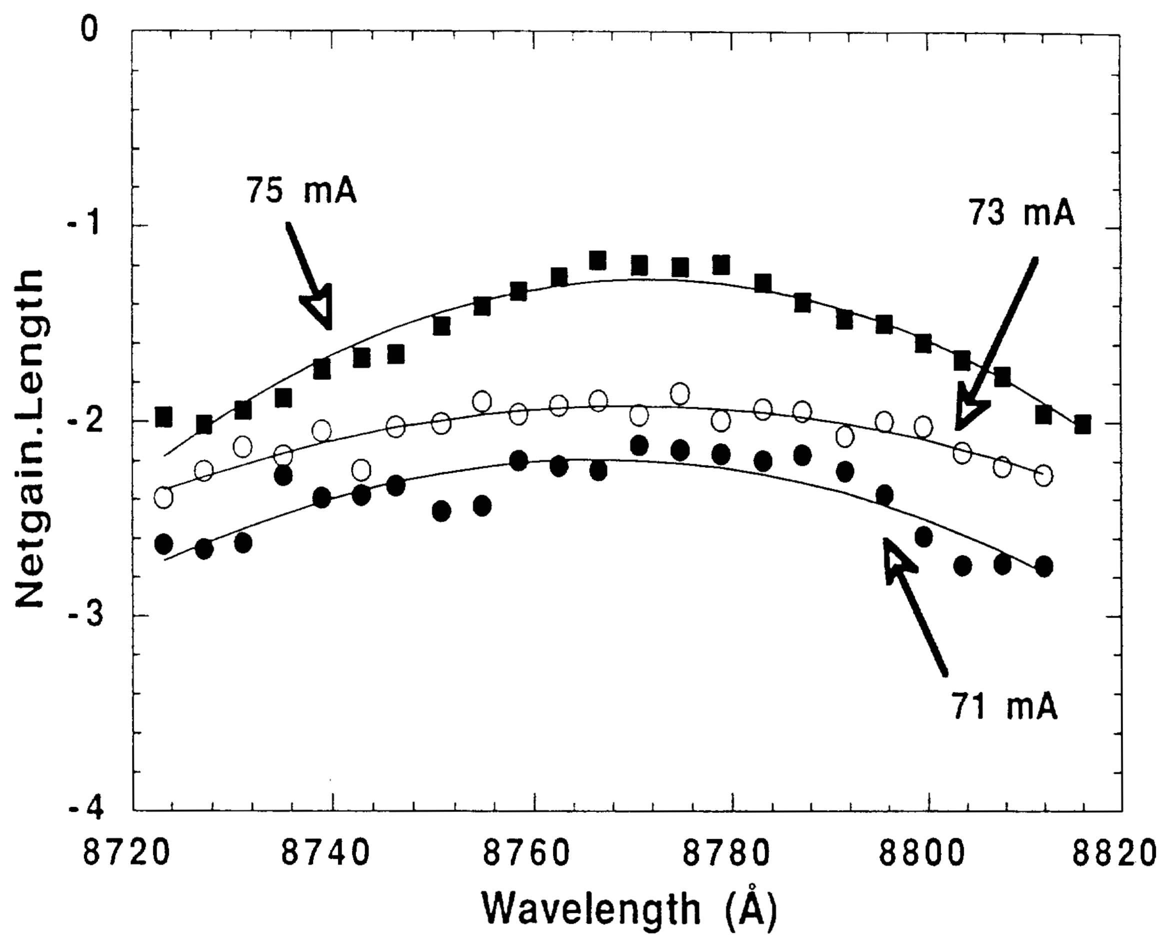

Figure 5.3. (Gain . Length) product at three injection levels (71 mA, 73 mA and 75 mA). The data were fitted to standard parabolic relationship (see text).

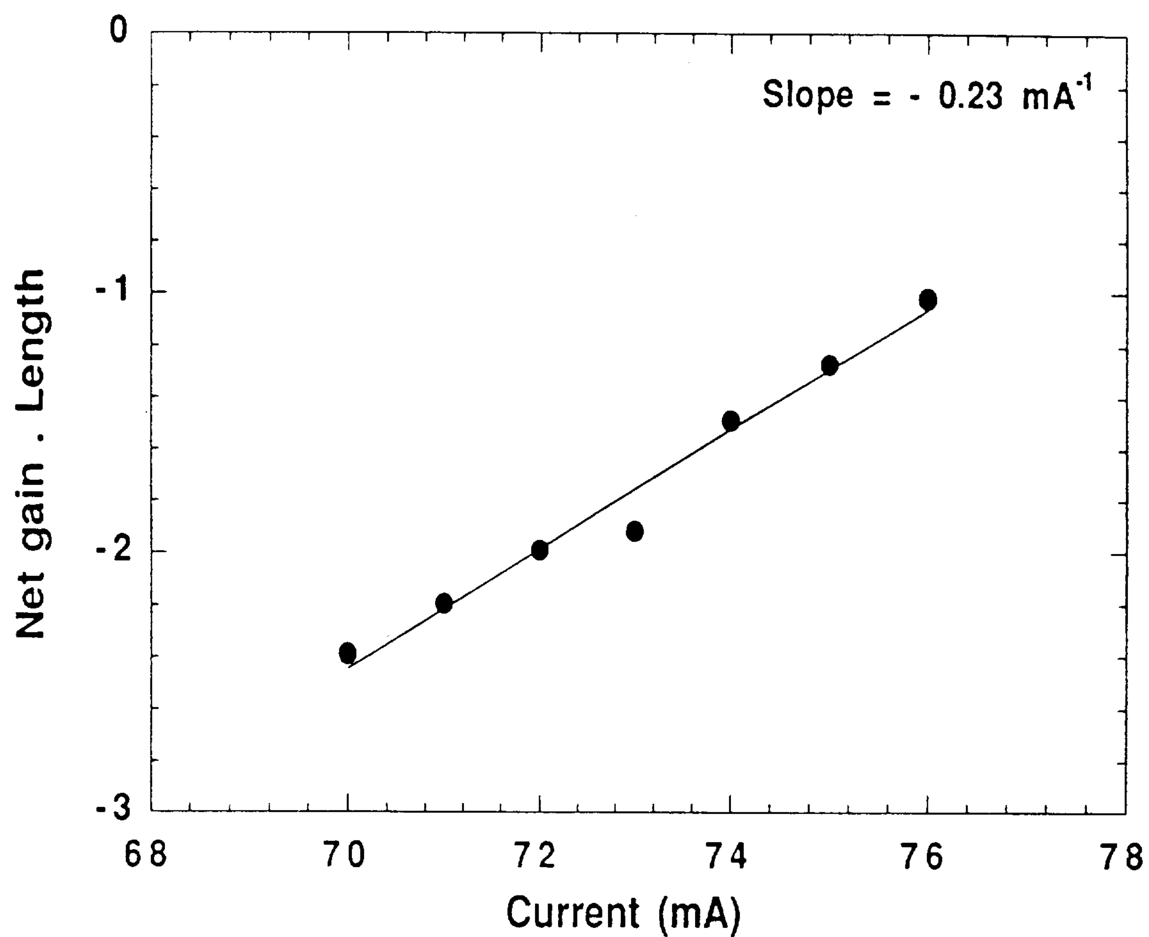

Figure 5.4. (Net gain . Length) product with drive current at 877 nm. The slope is the change in this product in the current range measured at 877 nm.

saturation trend to be detected. The slope of the variation of the gain-length product with current (dGL/dI) was then obtained at various wavelengths as plotted in Figure 5.5. The peak of this curve at 0.23 mA^{-1} is seen to more or less coincide with the spectral position of the gain peak which was also the lasing wavelength.

To determine an approximate value of dg/dN from the peak value of dGL/dI, knowledge of the dependence of the current density J on the carrier density N, $J = q L_z [AN+BN^2+CN^3]$, where each term represents, respectively, the contribution of non-radiative, radiative and Auger recombination mechanisms, is necessary. L_z is the active material thickness and q is the electronic charge. Following Asada *et al.*[105] in the range of N values considered, these contributions can be described by

$$J \approx q L_z B_{eff} N^2 \tag{5.2}$$

where B_{eff} is an effective (radiative)recombination constant. Assuming massive carrier spill-over from the QW into the guide and neglecting the current from the QW, we replace L_z in eqn. (5.2) by the guide thickness d_z. The carrier density in the guide, averaged over the stripe width, is then given by

$$N = \sqrt{(I/(d_z W_{eff} q B_{eff} L))} \tag{5.3}$$

where W_{eff} is an effective width of the stripe that accounts for lateral current spreading. We then obtain

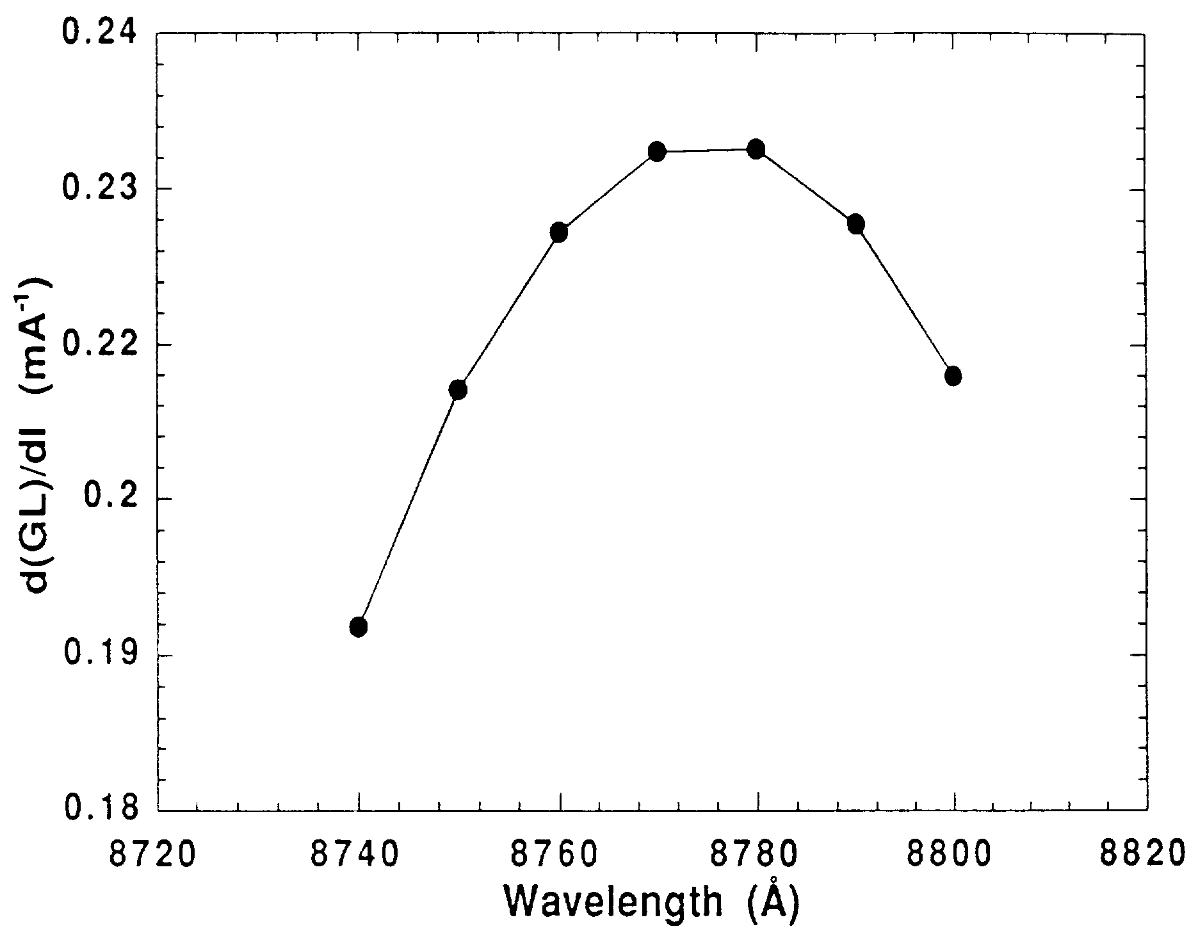

Figure 5.5. Spectral variation of the change in the Gain.Length product with drive current over a 60 Å wavelength range. The line connecting the data points is only an interpolation of the points.

$$\frac{dI}{dN} = \frac{2I}{N} \tag{5.4}$$

Additionally, $dG = G_{d_z} dg$, where G_{d_z} is the mode confinement to the guide layer.

The various parameters needed for the carrier density estimation are listed in Table 5.1. W_{eff} was estimated assuming a lateral current spread of about 1.5 μm (equivalent to the spacing between the stripe contact and the active QW layer) on each side of the stripe. Thus, the dGL/dI peak value of 0.23 mA^{-1} corresponds to a value for dg/dN of 8.2×10^{-16} cm^2 at a carrier density in the guide, N, of 3.4×10^{18} cm^3 (I= 75 mA); note that the high N value obtained in the estimate clearly justifies the spill-over assumption and the neglect of the QW current. In comparing this value with those of Rideout *et al.*[25] for strained InGaAs/GaAs QW lasers at around the same carrier densities but restricted to the QW, we find that our values are about 1.2 times higher. Note, however, that our values are at a temperature (12.6 °C) slightly below room temperature. Our estimated peak value for the differential gain, dg/dN, is a factor of 2 greater than the values determined both theoretically[106] and experimentally[107,108] for unstrained AlGaAs/GaAs QW lasers operated with low injection at comparable carrier densities in the QW. Values reported for GaAs DH structures[104,109] are quoted in terms of dg/dI only and, thus, a quantitative comparison is not possible due to lack of information on carrier density estimates. However, our peak value of dg/dN is a factor of 3.5 greater than the highest values reported for InGaAsP bulk lasers[110,111]. This remarkably higher value, in spite of the spill-over into the guide due to a

Table 5.1. Parameters used in the estimate of carrier density at I = 75 mA

	Variable	Values
Cavity length	L	200 μm
Stripe width	W	5 μm
Effective width	W_{eff}	8 μm
Recombination coefficient	B_{eff}	1.0×10^{-10} cm^3/s [a]
Well thickness	L_z	7.5 nm
Guide thickness	d_z	258 nm
Confinement factor	Γ_{d_z}	0.68 [b]
Group index	n_g	4.63
Mode spacing	$\Delta\lambda$	4.15 Å
Lasing wavelength	λ	877 nm

[a] Henry Kressel and J. K. Butler, "Semiconductor Lasers and Heterojunction LEDs", pp. 93, Academic Press Inc., New York, 1977.

[b] Calculated from a five-layer waveguide model.

high quasi-Fermi level, is indicative of effects potentially still caused by strain and the quantum well.

5.4.2 Mode Shift and Differential Index

The carrier induced shift in the mode position was determined as a function of injection level. To get an accurate value for the shift a cross-correlation technique was employed. The spectral charts were digitized using a scanner and processed in a Macintosh computer to generate enough number of data points. It was then transferred to a Microvax computer where data sets for three modes centered at a particular wavelength for two successive current levels were taken and the shift between them was reliably obtained using the technique. Figure 5.6 provides the extent of shift in mode position with drive current at the gain peak and Fig. 5.7 shows the spectral variation of this shift exhibiting a small scatter. Fig. 5.7 is approximated by a straight line since there was not much justification to assume otherwise, even though it also fits a parabolic curve with a small curvature, as shown. The magnitude of shift was about 0.3 Å per mA change in the injected current. Using the previously derived relationship between current and carrier density and,

$$\frac{n_g}{\Gamma_{d_z}\lambda}\, d\lambda = dn \tag{6}$$

where the group index $n_g = \lambda^2/(2L\Delta\lambda)$, we can relate the mode shift $d\lambda$ to the

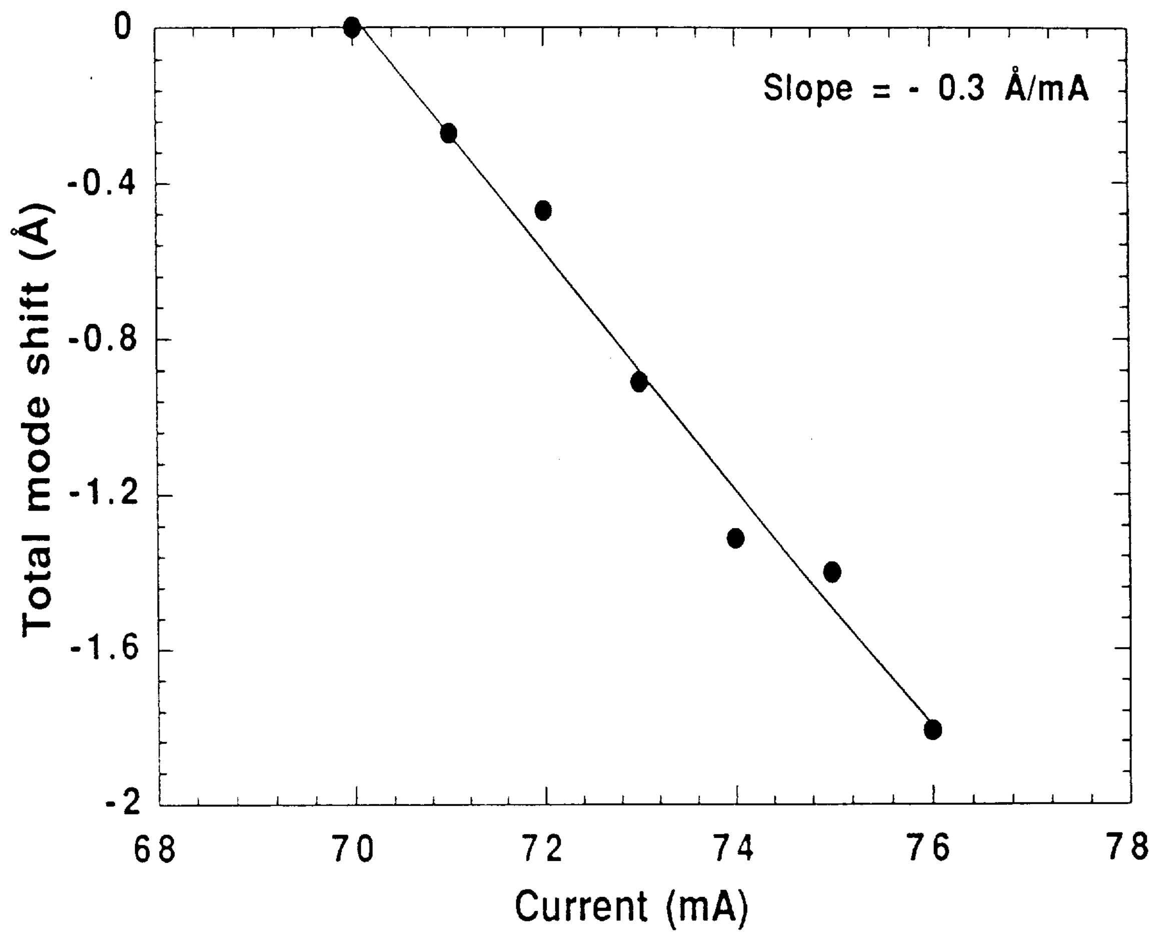

Figure 5.6. Total mode shift as a function of drive current for mode at 877 nm.

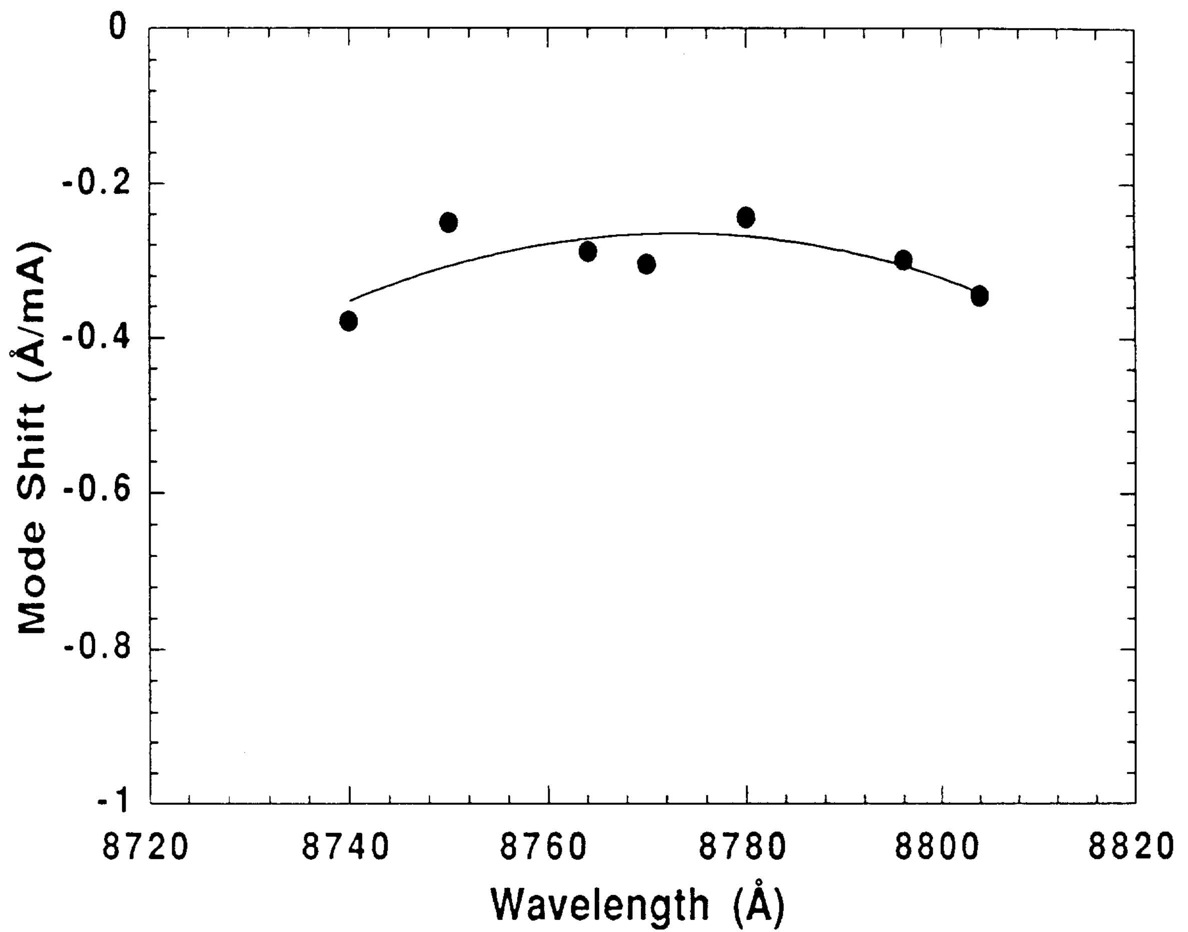

Figure 5.7. Spectral variation of the mode shift over a 60 Å wavelength range. A parabolic fit is shown to indicate the trend in the data.

change in refractive index dn. We see that the shift $d\lambda/dI$ of -0.3 Å mA^{-1} correlates to a value for dn/dN of about -1.1×10^{-20} cm^3 at a carrier density in the guide N of 3.4×10^{18} cm^{-3} . This value for dn/dN is comparable to those of standard DH AlGaAs lasers[112], a good indication of the spill-over and the emission being close to GaAs; it is less than values reported for bulk InGaAsP lasers by Manning *et al.*[112] and is also less by a factor of about 1.5 when compared with the values of Rideout *et al.*[25] for strained-layer InGaAs/GaAs QW lasers at that carrier concentration in the QW. Since we could not measure dg/dN and dn/dN as a function of the carrier concentration over a larger range, a comparison with similar relationships published by others such as Rideout *et al.*[25] is not too meaningful.

5.4.3 Linewidth enhancement factor

The spectral variation of the linewidth enhancement factor as given by eqn. (5.1), is shown in Figure 5.8. A minimum of 1.7 was measured at the wavelength where the gain as well as the differential gain peaked. This value is in agreement with the minimum value determined by Rideout *et al.*[25] for a 4.8 nm strained-layer InGaAs/GaAs SQW buried heterostructure device with a 3.5 μm stripe width and a cavity length of 49 μm at a lasing wavelength of 1.07 μm and a QW carrier density of 5.0×10^{18} cm^{-3} ; it should be noted that this minimum α was observed below the maximum value for dg/dN. In our investigation, however, the quantum well size was 7.5 nm with a 5 μm gain-guided stripe width and a cavity length of 200 μm, while lasing occurred in quasi-DH operation at 877 nm. This makes the measured low value of α

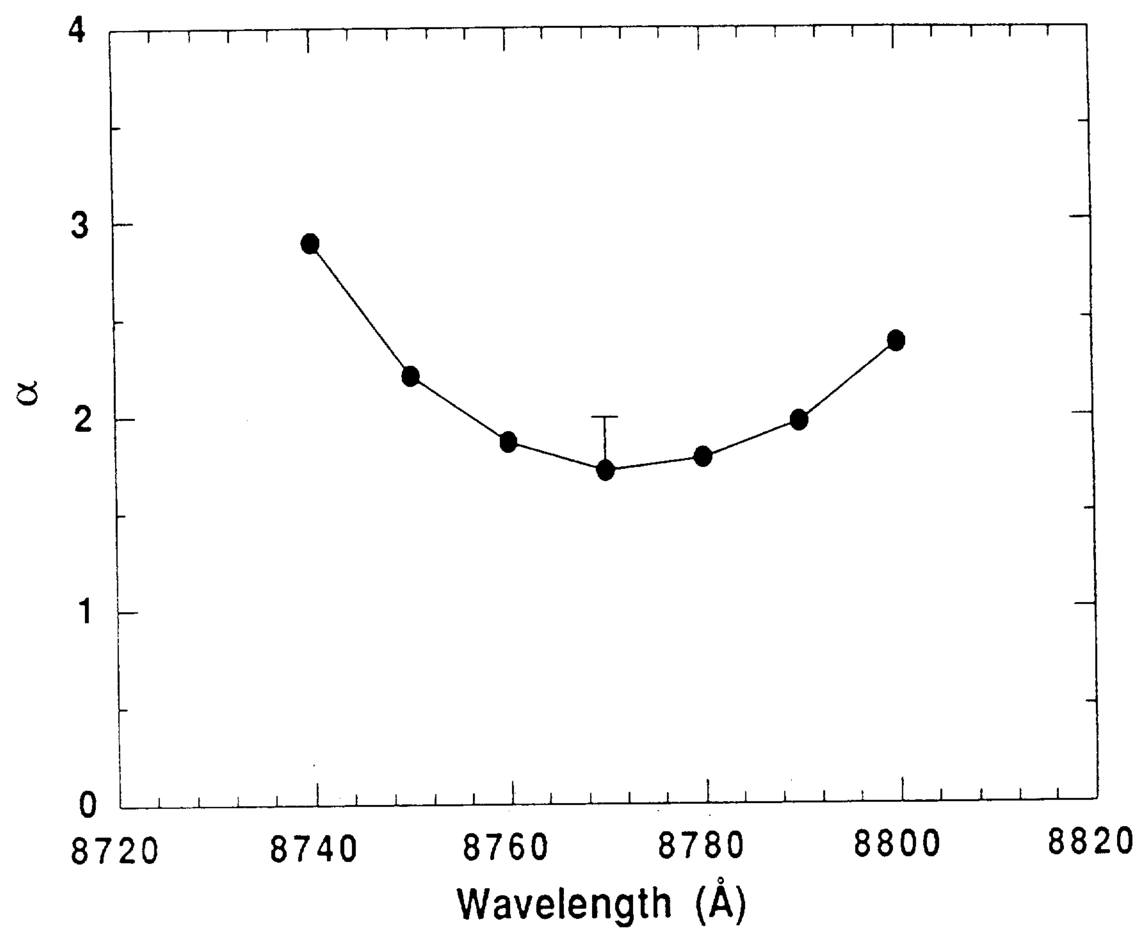

Figure 5.8. Spectral variation of the linewidth enhancement factor, α, over a 60 Å wavelength range under quasi-DH operation.

particularly remarkable, since the emission is dominated by recombination from the GaAs guiding layer. The lower value could in part be a result of the increased losses pushing up the quasi-Fermi level which has been shown theoretically and experimentally by Arakawa and Yariv[113] to influence the value of α. In their investigations of GaAs/AlGaAs DH lasers with different photon energy they found that α decreased monotonically with higher photon energy (i.e., increase in Fermi level) with a lowest value measured near 2.6 . Interestingly, our spectral variation of α is qualitatively similar to that measured for unstrained multi-quantum-well (MQW) structures by Hausser *et al.*[114] and the strained InGaAs/InP MQW laser measured by Dutta *et al.*[103]

In the above investigations a polarizer was not used to remove the TM component of the emitted light. This resulted in an artificial baseline to be superimposed thereby affecting the accurate estimation of the peak-to-valley ratio, r, and hence that of the net gain. Subsequently, we estimated the TE-to-TM ratio and found it to be about 70% to 30% in the current range of interest. The TM component did not saturate at threshold exhibiting a small positive slope at current levels just above threshold. To account for this TM component as well as for the shoulder on the long wavelength side of the longitudinal modes, (Fig. 5.2), an analysis was done to estimate its effect on the value for the differential gain and hence that of α. We concluded that there could be at most a 20% uncertainty in the final value for α resulting in somewhat higher values than measured (as shown by error bar in Fig. 5.8). Considering this uncertainty we find that the minimum value for α is still about 2 at the gain maximum, which is lower than values reported for DH

lasers but close to the values reported for strained and unstrained QW lasers by other workers.

5.5 Discussion

In summary the spectral variation of d(GL)/dI, dl/dI, and α for a strained-layer InGaAs/GaAs SQW laser operated in a quasi-DH mode at the barrier wavelength under extremely high injection condition have been measured below lasing threshold over a wavelength range of 60 Å. The necessary large lateral and longitudinal (mirror) losses were provided by a narrow (5 μm) gain-guided lasing stripe and a relatively short (200 μm) cavity length. From the measured quantities rough estimates for the average carrier density, N, in the GaAs guide layer, the differential gain, dg/dN, and differential index, dn/dN, were made at the optimum wavelength (Table 5.2). An enhanced value for the differential gain (dg/dN) has been estimated, (8.2×10^{-16} cm^2 at about 3.4×10^{18} cm^{-3} injection carrier density in the guide layer), for this narrow-stripe short device which is higher than values reported by other workers at corresponding carrier densities for both QW (strained and unstrained) and DH structures.

It is relevant to point out that these estimates are dependent on the accuracy of parameters like W_{eff} and B_{eff} used in the above estimation. From equations (5.3) and (5.4) for dg/dN and from equations (5.4) and (5.5) for dn/dN, it is seen that both dg/dN and dn/dN are proportional to $(W_{eff}B_{eff})^{1/2}$. With a maximum expected uncertainty of ± 50% in the value for B_{eff} and an additional ± 20% possible uncertainty for W_{eff}, there results a

Table 5.2. Estimated values at optimum wavelength λ = 877 nm

Carrier density	N	$(3.4 \times 10^{18} \mp 0.9 \times 10^{18})$ cm^{-3}
Differential gain	dg/dN	$(8.2 \times 10^{-16} \pm 2.2 \times 10^{-16})$ cm^2
Differential index	dn/dN	$(-1.1 \times 10^{-20} \mp 0.3 \times 10^{-20})$ cm^3
Linewidth enhancement factor	α	$1.7^{+0.3}_{-0.0}$

r.m.s variation of $\pm 27\%$ in the values for dg/dN and dn/dN; the r.m.s variation in the value for N is however, $\mp 27\%$ since the carrier density (from equation (5.3)) is seen to be inversely proportional to $(W_{eff}B_{eff})^{1/2}$. Consequently, a realistic lower limit for dg/dN would be around 6×10^{-16} cm^2 at the carrier density, N, of 4.3×10^{18} cm^{-3} in the guide. Note that an upper bound in N results in a lower bound for dg/dN and dn/dN. On the other hand, any additional non-radiative or Auger current contributions (AN and CN^3) would increase B_{eff}, thus increasing dg/dN and dn/dN from the estimates given.

The estimated value for the index shift (dn/dN), ($- 1.1 \times 10^{-20} \mp 0.3 \times 10^{-20}$ cm^2), however, is in excellent agreement with values reported in the literature for the case of GaAs DH lasers, a good indication of the carrier spill-over into the guide due to the large losses. This index shift is considerably lower than values reported for QW structures. Thus the enhanced differential gain results in a remarkably low value for the linewidth enhancement factor, α, of about 1.7 - 2.0 at a carrier density of $(3.4 \times 10^{18} \mp 0.9 \times 10^{18})$ cm^{-3}, in spite of the lasing being from the GaAs guiding region. This result could be due to the combined influence from strain and quantum effects. Even though the increased loss leads to a strong increase in the threshold current[35,48] with a simultaneous shift of the lasing wavelength to shorter values close to the GaAs barrier, such narrow-stripe gain-guided strained-layer SQW lasers have the additional advantage of providing strong lateral coupling in laser array applications[115]. The low value for α even under quasi-DH operation at high injection makes such lasers attractive for incorporating a wavelength switching capability by proper control of losses in the lasing cavity.

Chapter 6

CONCLUSIONS

In the present dissertation the device characteristics in terms of time-integrated and time-resolved lasing properties have been experimentally investigated under pulsed high injection conditions for strained-layer InGaAs/GaAs single-quantum-well gain-guided stripe-geometry lasers. The experiments show the potential use of such devices for wavelength switching operation between widely separated wavelengths in a single device. We have demonstrated the possibility of shifting the operating wavelength in a controllable manner using the choice of appropriate cavity length and stripe-width. These devices exhibited lasing wavelength switching and "simultaneous" (in a time-integrated sense) multiple wavelength emission through appropriate variation in the injection current utilizing the different transitions available in the quantum well and the barrier.

In determining the relationship between the threshold current and the cavity length, a striking feature was the rise in threshold current towards shorter cavity length which is caused by the strong gain saturation at these high injection densities. The low gain confinement, Γ, in a single quantum well, makes this "anomalous" effect more pronounced. The additional larger

optical lateral losses that were seen in these strained-layer devices, as compared to the unstrained systems, and the increased pumping required to achieve gain forced loss of carriers from the quantum well. This enhanced the gain saturation seen at the quantum well transitions. With sufficient carriers present in the surrounding regions due to excessive carrier spill-over, the device was found to switch to shorter wavelengths corresponding to the barrier bandgap, for shorter cavities and/or smaller stripe-widths, at sufficiently high injection levels.

A systematic study on the spectral and temporal characteristics of the successive wavelength switching observed in the devices through both time-resolved spectral and picosecond resolved light pulse measurements provided a better handle on the possible physical mechanisms involved for the observed behavior. Measurements of the relaxation oscillation frequency with power showed the presence of an instability condition, $dg/dP > 0$ due to saturable absorber or lateral hole burning. Preliminary comparison of the experimentally observed behavior of the relaxation oscillation frequency with that for the damping, using a small signal analysis model, indicated that a more complex large signal analysis is required. In addition to spectral hole burning effects, due to the energetic redistribution of the carriers, redistribution of carriers spatially (vertically and laterally) also have to be taken into account to understand the nonlinear gain dependence with power observed at the longer wavelengths which facilitated the onset of lasing at the shorter wavelengths. The "de-damping" as a result of this nonlinearity resulted in self-pulsations in the output. However, the shift in the operating wavelength to shorter values was associated with the degradation of the

spectra due to lateral instabilities in the gain profile. The chaotic behavior observed in the light output will have to be removed to make the device useful for applications.

Properties of the strained-layer systems, like differential gain and linewidth enhancement factor, were investigated under fairly high injections. It is known that as a result of the splitting of the valence band and a reduction in the asymmetry of the density of states these values are improved at low injection when gain saturation effects are not yet in play. Operating the device in a quasi-double-heterostructure mode, however, showed remarkably high values for the differential gain and low values for the linewidth enhancement factor. Their spectral variation was also similar to the unstrained and strained systems at low injections.

Further investigation of such devices need to be performed with more controllable loss mechanisms to obtain controllable switching of the operating wavelength and to also maintain single spatial mode operation at all current levels of interest. This would make the device suitable for several applications. Index guided structures, often used for single mode operation, have to be used with integrated control of the loss (either mirror or internal) to obtain multi-wavelength operation in a single device. The realization of a laser diode with controllable switching of widely separated wavelengths would allow for simple wavelength multiplexing in non-coherent optical communication systems as well as multi-wavelength addressing in optical information systems. Additionally, it is anticipated[59] that monolithic integration of wavelength switching laser diodes with other photonic elements might create new optical logic circuits which could, e.g., provide

simple digital functions in optical interconnects. With the availability of wavelengths from 1.1μm to 880 nm, there is a possibility of "simultaneous" frequency doubled generation of blue and green with a single source and a waveguide using Quasi-Phase Matching (QPM) techniques[116]. Such an arrangement, if done in a hybrid configuration, would prove invaluable in enhancing the performance of optical storage systems, optical recording, displays, and many other systems that require compact visible sources.

References

1. Y. Arakawa and A. Yariv, "Quantum well lasers - gain, spectra, dynamics", *IEEE J. Quantum Electron.*, vol. QE-22, pp. 1887-1899, 1986.
2. J. H. Van der Merve, "Crystal Interfaces. Part I. Semi - infinite crystals," *J. Appl. Phys.*, vol. 34, pp 117-122, 1963. -----, "Crystal Interfaces. Part II. Finite overgrowth," J.Appl. Phys., vol. 34, pp. 123-127., 1963
3. J. W. Matthews and A. E. Blakeslee, "Defects in epitaxial multilayers. 1. Misfit dislocations," *J. of Crystal Growth*, vol 27, pp 118-125, 1974.
4. I. J. Fritz, S. T. Picraux, L. R. Dawson, T. J. Drummond, W. D. Laidig and N. G. Anderson, "Dependence of critical layer thickness on strain for $In_xGa_{1-x}As$/GaAs strained-layer superlattices," *Appl. Phys. Lett.*, vol. 46, pp 967-969, May 1985.
5. G. C. Osbourn, "Strained-layer superlattices: A brief review," *IEEE J. Quantum. Electron.*, vol. QE-22, pp. 1677-1681, 1986.
6. G. C. Osbourn, P. L. Gourley, I. J. Fritz, R. M. Biefield, R. L. Dawson, and T. E. Zipperian, "Principles and applications of semiconductor strained-layer superlattices," in *Semiconductors and Semimetals*, vol. 24, R. K. Willardson and A. C. Beer, Ed. New York: Academic, 1987.
7. M. D. Camras, J. M. Brown, N. Holonyak, Jr., M. A. Nixon, R. W. Kaliski, M. J. Ludowise, W. T. Dietze, and C. R. Lewis, "Stimulated emission in strained-layer quantum well heterostructures," *J. Appl. Phys.*, vol. 54, pp. 6183-6189, 1983.
8. N. G. Anderson, Y. C. Lo, and R. M. Kolbas, "High efficiency carrier collection and simulated emission in thin (50Å) pseudomorphic $In_xGa_{1-x}As$ quantum well," *Appl. Phys. Lett.*, vol. 49, pp. 758-760, 1986.
9. M. A. Tischler, N. G. Anderson, R. M. Kolbas, and S. M. Bedair, "Stimulated emission from ultra-thin (6.6Å) InAs/GaAs quantum well heterostructures grown by atomic layer epitaxy," *Appl. Phys. Lett.*, vol. 50, pp. 1266-1268, 1987.
10. W. D. Laidig, P. J. Caldwell, Y. F. Lin, and C. K. Peng, "Strained-layer quantum-well injection laser," *Appl. Phys. Lett.*, vol. 44, pp. 653-655, 1984.
11. W. D. Laidig, Y. F. Lin, and P. J. Caldwell, "Properties of $In_xGa_{1-x}As$-GaAs strained-layer quantum-well-heterostructure lasers," *J. Appl. Phys.*, vol. 57, pp. 33-38, 1985.
12. T. E. Zipperian, R. L .Dawson, E. E. Barnes, J. J. Wiczer, and G. C. Osbourn, "InGaAs/GaAs strained-layer superlattice (SLS), junction photodetectors, LED's, injection lasers and FET's for optoelectronics applications," in *IEEE Int. Electron Devices Meet. Tech. Dig.*, pp. 524-527, 1984.
13. D. Fekete, K. T. Chan, J. M. Ballantyne, and L. F. Eastman, "Graded

index separate-confinement InGaAs/GaAs strained-layer quantum well laser grown by metalorganic chemical vapor deposition," *Appl. Phys. Lett.*, vol 49, pp. 1659-1660, 1986.

14. S. E. Fischer, D. Fekete, G. B. Feak, and J. M. Ballantyne, "Ridge waveguide injection laser with a GaInAs strained-layer quantum well (l = 1μm)," *Appl. Phys. Lett.*, vol. 50, pp. 714-716, 1987.
15. Y. J. Yang, K. Y. Hsieh, and R. M. Kolbas, "Continuous room temperature operation of an InGaAs-GaAs-AlGaAs strained-layer laser," *Appl. Phys. Lett.*, vol. 51, pp. 215-217, 1987.
16. S. M. Bedair, T. Katsuyama, M. Timmons, and M. A. Tischler, "A new GaAsP-InGaAs strained-layer superlattice light emitting diode," *IEEE Electron. Device. Lett.*, vol. EDL-5, pp. 45-47, 1984.
17. T. Katsuyama, Y. J. Yang, and S. M. Bedair, "Lifetime test for high current injection strained layer superlattice light emitting diode," *IEEE Electron. Device. Lett.*, vol. EDL-8, pp. 240-242, 1987.
18. G. E. Bulman, D. R. Myers, T. E. Zipperian, R. L. Dawson, J. J. Wiczer, and R. M. Biefeld, "Photocurrent multiplication in ion implanted lateral $In_{0.2}Ga_{0.8}As$/GaAs strained-layer superlattice photodetectors," *Appl. Phys. Lett.*, vol. 47, pp. 733-755, 1985.
19. J. J. Rosenberg, M. Benlamri, P. D. Kirchner, J. M. Woodall,and G. D. Pettit, "An $In_{0.15}Ga_{0.85}As$/GaAs pseudomorphic single quantum well HEMT," *IEEE Electron Device Lett.*, vol. EDL-6, pp. 491-493, 1985.
20. T. Henderson, M. I. Aksun, C. K. Peng, M. Morkoc, P. C. Chao, P. M. Smith, K. H. G. Duh, and L. F. Lester, "Microwave performance of a quarter-micrometer gate low noise pseudomorphic InGaAs/AlGaAs modulation doped field effect transistor," *IEEE Electron Device Lett.*, vol. EDL-7, pp. 649-651, 1986.
21. D. F. Welch, W. Streifer, C. F. Schaus, S. Sun, and P. L. Gourley, "Gain characteristics of strained quantum well lasers," *Appl. Phys. Lett.*, vol. 56, pp. 10-12, 1990.
22. D. P. Bour, D. B. Gilbert, L. Elbaum, and M. G. Harvey, "Continuous, high-power operation of a strained InGaAs/GaAs quantum well laser," *Appl. Phys. Lett.*, vol. 53, pp. 2371-2373 , 1988.
23. W. Stutius, P. Gavrilovic, J. E. Williams, K. Meehan, and J. H. Zarrabi, "Continuous operation of high power (200 mW) strained-layer Ga1-xInxAs/GaAs quantum-well laser with emission wavelength 0.87μm < l < 0.95μm," *Electron. Lett.*, vol. 24, pp. 1492-1493 , 1988.
24. S. D. Offsey, W. J. Schaff, P. J. Tasker, and L. F. Eastman, "Optical and microwave performance of GaAs-AlGaAs and strained layer InGaAs-GaAs-AlGaAs graded index separate confinement heterostructure single quantum well lasers," *IEEE Photon. Technol. Lett.*, PTL-2, pp. 9-11 , 1990.

25. W. Rideout, B. Yu, J. Lacourse, P. K. York, K. J. Beernink, and J. J. Coleman, "Measurement of the carrier dependence of differential gain, refractive index, and linewidth enhancement factor in strained-layer quantum well laser," *Appl. Phys. Lett.*, vol. 56, pp. 706-708 , 1990.
26. K. Y. Lau, S. Xin, W. I. Wang, N. Bar-Chaim, and M. Mittelstein, "Enhancement of modulation bandwidth in InGaAs strained-layer single quantum well laser," *Appl. Phys. Lett.*, vol. 55, pp. 1173-1175 , 1989.
27. N. K. Dutta, J. Wynn, D. L. Sivco, and Y. Cho, "Linewidth enhancement factor in strained quantum well laser," *Appl. Phys. Lett*, vol. 56, pp. 2293-2294 , 1990.
28. E. Yablonovitch and E. O. Kane, "Reduction of lasing threshold current density by the lowering of valence band effective mass," *J. Lightwave Technol.*, vol. LT-4, pp. 504-506, 1986; see also ------- "Correction", *J. Lightwave. Technol.*, vol. LT-4, pp.961, 1986.
29. R. M. Kolbas, N. G. Anderson, W. D. Laidig, Y. Sin, Y. C. Lo, K. Y. Hsieh, Y. J. Yang, "Strained-layer InGaAs-GaAs-AlGaAs photopumped and current injection lasers", IEEE J. Quantum Electron., vol.24 , pp.1605-1613 , 1988.
30. C. Shieh, H. Lee, J. Mantz, D. Ackley, and R. Engelmann, "Critical thickness in strained-layer GaInAs/GaAs quantum well lasers," *Electron. Lett.* vol. 25, pp. 1226-1228, Aug 1989.
31. A. Larsson, S. Forouhar, J. Cody, R. J. Lang, "High Power operation of highly reliable narrow stripe pseudomorphic single quantum well lasers emitting at 980nm," *IEEE Photon. Technol. Lett.*, vol. 2, pp. 307-309, 1990.
32. M. Okayasu, M. Fukuda, T. Takeshita, and S. Uehara, "Stable operation (over 5000 h) of high power 0.98-μm InGaAs-GaAs strained quantum well ridge waveguide lasers for pumping Er^{3+} - doped fiber amplifiers," *IEEE Photon. Technol. Lett.*, vol. 2, pp. 689-691, 1990.
33. R. G. Waters, P. K. York, K. J. Beernink, and J. J. Coleman, "Viable strained-layer laser at $\lambda = 1100$ nm," *J.Appl. Phys.*, vol. 67, pp. 1132, 1990.
34. K. J. Beernink, P. K. York, J. J. Coleman, R. G. Waters, J. Kim, and C. M. Wayman, "Characterization of InGaAs-GaAs strained-layer lasers with quantum wells near critical thickness," *Appl. Phys. Lett.*, vol. 55, pp. 2167-2169, 1989.
35. C. Shieh, J. Mantz, H. Lee, D. Ackley, and R. Engelmann, "Anomalous dependence of threshold current on stripe width in gain-guided strained-layer InGaAs/GaAs quantum well lasers," *Appl. Phys. Lett.*, vol. 54, pp. 2521-2523, 1989.
36. K. J. Beernink, J. J. Alwan, and J. J. Coleman, "Antiguiding in narrow stripe gain-guided InGaAs-GaAs strained-layer lasers," *J. Appl. Phys.*,

vol. 69, pp. 56-60, 1991.

37. I. Suemune, L. A. Coldren, M. Yamanishi, and Y. Kan, "Extremely wide modulation bandwidths in a low threshold current strained quantum well laser," *Appl. Phys. Lett.*, vol. 53, pp. 1378-1380, Oct. 1988.

38. A. Ghiti, E. P. O'Reilly, and A. R. Adams, "Improved dynamics and linewidth enhancement factor in strained-layer lasers," *Electron. Lett.*, vol. 25, pp. 821-823, June 1989.

39. P. Urquhart, "Review of rare earth doped fiber lasers and amplifiers," *IEE Proc.* part J, vol. 135, pp. 385, 1988.

40 P. K. York, K. J. Beernink, G. E. Fernandez, and J. J. Coleman, "InGaAs-GaAs strained-layer quantum well buried heterostructure lasers (l > 1μm) by metalorganic chemical vapor deposition," Appl. Phys. Lett., vol. 54, pp. 499-501, Feb. 1989.

41 J. Hwang, C. K. Shih, P. Pianetta, G. D. Kubiak, R. H. Stulen, L. R. Dawson, Y. C. Pao, and J. S. Harris, "Effect of strain on the band structure of GaAs and $In_{0.2}Ga_{0.8}As$," *Appl. Phys. Lett.*, vol. 52, pp.308-310, Jan. 1988.

42. E. D. Jones, S. K. Lyo, J. F. Klem, J. E Schirber, and C. P. Tigges, "Simultaneous measurement of the conduction and valence-band masses in strained layer structures," *Proc. 18th Int. Symp. GaAs Related compounds*, Inst. Phys. Conf. Ser., vol. 96, Atlanta, Ga, pp. 243-247, 1988.

43. A. R. Adams, "Band-structure engineering for low threshold high efficiency semiconductor lasers," *Electron. Lett.*, vol. 22, p. 249-250, Feb. 1986.

44. J. P. Loehr and J. Singh, "Theoretical studies of the effect of strain on the performance of strained quantum well lasers based on GaAs and InP technology," *IEEE J. Quantum Electron.*, vol. 27, pp. 708-715, 1991.

45. P. S. Zory, A. R. Reisinger, L. J. Mawst, G. Costrini, C. A. Zmudsinski, M. A. Emanuel, M. E. Givens, J. J. Coleman, "Anomalous length dependence of threshold for thin quantum well AlGaAs diode laser," *Electron. Lett.*, vol. 22, pp. 475-476, 1986.

46. A. R. Reisinger, P. S. Zory, and R. G. Waters, "Cavity length dependence of the threshold behavior in thin quantum well semiconductor laser," *IEEE J. Quantum Electron.*, QE-23, pp. 993-999, 1987.

47. J. Z. Wilcox, G. L. Peterson, S. Ou, J. J. Yang, M. Jansen, and D. Schecter, "Length dependence of threshold current in multiple quantum well laser," *Electron. Lett.*, vol. 24, pp.1218-1219, 1988.

48. J. Lee, C. Shieh, and M. O. Vassell, "Variation of threshold current with cavity length in strained-layer InGaAs/GaAs quantum well lasers," *J. Appl. Phys.*, vol. 69, pp. 1882-1891, 1991.

49. C. Shieh, R. Engelmann, J. Mantz, and K. Alavi, "Cavity length

dependence of threshold current for quantum well lasers," *Appl. Phys. Lett.*, vol. 54, pp. 1089-1091,1991.

50. W. Idler, S. Hauser, H. Schweizer, G. Weimann, and W. Schlapp, "Reduced spontaneous emission factor in quantum well laser," *Electron. Lett.*, vol .24, pp. 786-787, 1988.
51. K. Petermann, "Calculated spontaneous emission factor in double-heterostructure injection laser with gain-induced waveguiding," *IEEE J. Quantum Electron.*, QE-15, pp. 566-570, 1979.
52. R. B. Michael, D. Fekete, and R. Sarfaty, "Quantum well width and In composition effects on the operating characteristics of InGaAs/GaAs strained single quantum well diode lasers," *Appl. Phys. Lett.*, vol. 59, pp. 3219-3222, 1991.
53. J. A. Brum, and G. Bastard, "Resonant carrier capture by semiconductor quantum wells," *Phys. Rev. B.*, vol. 33, pp. 1420-1423, 1986.
54. G. P. Agrawal and N. K. Dutta, *Long Wavelength Semiconductor Lasers*. New York: Van Rostrand Reinhold, 1986.
55. C. Zah, R. Bhat, F. J. Favire, Jr., S. G. Menocal, N. C. Andreadakis, K. W. Cheung, D. M. D. Hwang, M. A. Koza, and T. P. Lee, "Low-threshold 1.5μm compressive-strained multiple- and single-quantum-well lasers," *IEEE J. Quantum Electron.*, vol. 27, pp. 1440-1450, 1991.
56. H. Hirayama, Y. Miyake, and M. Asada, "Analysis of current injection efficiency of separate-confinement-heterostructure quantum-film lasers," *IEEE J. Quantum Electron.*, vol. 28, pp. 68-74, 1992.
57 R. Nagarajan, T. Kamia, and A. Kurobe, "Band filling in GaAs/AlGaAs multiquantum well lasers and its effect on threshold current," *IEEE J. Quantum Electron.*, vol. 25, pp. 1161-1170, 1989.
58. Y. Cai, R. Engelmann, and R. Raghuraman, "Simple model for carrier spill-over in quantum-well lasers consistent with local charge neutrality," OSA '92, Albuquerque, New Mexico, September 1992.
59. M. Mittelstein, Y. Arakawa, A. Larsson, and A. Yariv, "Second quantized state lasing of a current pumped single quantum well laser", *Appl. Phys. Lett.*, vol. 49, pp.1689-1691, 1986.
60. Y. Tokuda, N. Tsukada, K. Fujiwara, K. Hamanaka, and T. Nakayama, "Widely separated wavelength switching of single quantum well laser diode by injection-current control", *Appl. Phys. Lett.*, vol. 49, pp.1629-1631, 1986.
61. Y. Tokuda, Y. Abe, T. Matsui, K. Kanamoto, N. Tsukada, and T. Nakayama, "Emission spectra of single quantum well lasers with inhomogeneous current injection", *J. Appl. Phys.*, vol. 64, pp. 1022-1026, 1988.
62. K. J. Beernink, J. J. Alwan, and J. J. Coleman, "Wavelength switching in narrow oxide stripe InGaAs-GaAs-AlGaAs strained-layer quantum well

heterostructure lasers", *Appl. Phys. Lett.*, vol. 58, pp. 2076-2078, 1991.

63. T. R. Chen, Y. Zhuang, Y. J. Xu, B. Zhao, A. Yariv, J. Ungar, and Se Oh, "Second quantized state oscillation and wavelength switching in strained-layer multi-quantum-well lasers", *Appl. Phys. Lett.*, vol. 60, pp. 2954-2956, 1992.
64. P. S. Zory, A. R. Reisinger, R. G. Waters, L. J. Mawst, C. A. Zmudzinski, M. A. Emanuel, M. E. Givens and J. J. Coleman, "Anomalous temperature dependence of threshold for thin quantum well AlGaAs diode lasers," *Appl. Phys. Lett.*, vol. 49, pp.16-18, 1986 .
65. E. O. Göbel, R. Höger, J. Kuhl, H. J. Polland and K. Ploog, "Homogeneous gain saturation in GaAs/AlGaAs quantum well laser," *Appl. Phys. Lett.*, vol. 47, pp.781-783, 1985.
66. J. T. Ebner, "Growth, fabrication, and modeling of pseudomorphic laser diodes," *Ph.D Thesis*, Oregon State University, pp.25-39, 1989.
67. M. C. Amman, "New stripe geometry laser with simplified fabrication process," *Electron. Lett.*, vol. 15, pp. 441-442, 1979.
68. S. R. Chinn, P. S. Zory, and A. R. Reisinger, "A model for GRIN-SCH-SQW diode lasers," *IEEE J. Quantum Electron.*, vol. 24, pp. 2191-2214, 1988.
69. H. C. Casey Jr., and M. B. Panish, *Heterostructure lasers : Part B*, Academic Press, 1978.
70. D. K. Wagner, R. G. Waters, P. L. Tihanyi, D. S. Hill, A. J. Rosa Jr., H. J. Vollmer, and M. M. Leopold, "Operating characteristics of single-quantum-well AlGaAs/GaAs high-power lasers" *IEEE J. Quantum Electron.*, vol. 24, pp. 1258-1265, 1988.
71. B. W. Hakki and T. L. Paoli, "CW degradation at 300 °K of GaAs double-heterostructure junction lasers. II. Electronic gain," *J. Appl. Phys.*, vol. 44, pp. 4113-4119, 1973.
72. R. P. Brouwer, C. H. F. Velzel, and B.-S. Yeh, "Lateral modes and self oscillations in narrow-stripe double-heterostructure GaAl-As injection lasers", *IEEE J. Quantum Electron.*, vol. 17, p 694-701, May 1981.
73. N. G. Basov, "Dynamics of injection lasers," *IEEE J. Quantum Electron.*, vol. 4, pp. 855-864, 1968.
74. H. Imai, K. Isozumi, and M. Takusagawa, "Deep level associated with the slow degradation of GaAlAs DH laser diodes," *Appl. Phys. Lett.*, vol. 33, pp. 330-332, 1978.
75. J. A. Copeland, "Semiconductor-laser self pulsing due to deep level traps," *Electron. Lett.*, vol. 14, pp. 809-810, 1978.
76. D. Kato, "Microscale degradation in (GaAl)As double-heterostructure diode lasers," *Appl. Phys. Lett.*, vol. 31, pp. 588-590, 1977.
77. R. W. Dixon, and W. B. Joyce, "A possible model for sustained oscillations (pulsations) in (Al,Ga)As double-heterostructure lasers,"

IEEE J. Quantum Electron., vol. 15, pp. 470-474, 1979.

78. J. P. Van der Ziel, J. L. Mertz and T. L. Paoli, "Study of intensity pulsations in proton-bombardment stripe-geometry double-heterostructure $Al_xGa_{1-x}As$ lasers," *J. Appl. Phys.*, vol. 50, pp. 4620-4637, 1979.
79. J. C. Cambell, S. M. Abbott, and A. G. Dentai, "A comparison of "normal" lasers and lasers exhibiting light jumps," *J. Appl. Phys.*, vol. 51, pp. 4010-4013, 1980.
80. C. H. Henry, "Theory of defect-induced pulsations in semiconductor injection lasers," *J. Appl. Phys.*, vol.51, pp. 3051-3061, 1980.
81. A. J. Schorr and W. T. Tsang, "Development of self-pulsations due to self-annealing of proton bombarded regions during aging in proton bombarded stripe-geometry AlGaAs DH lasers grown by molecular beam epitaxy," *IEEE J. Quantum Electron.*, vol. 16, pp. 898-901, 1980.
82. M. Kuznetsov, "Pulsations of semiconductor lasers with a proton bombarded segment: well developed pulsations," *IEEE J. Quantum Electron.*, vol. 21, pp. 587-592, 1985.
83. N. B. Patel, T. J. S. Mattos, F. C. Prince, and A. S. Nunes, "Narrow stripe graded barrier single quantum well lasers - Threshold current considerations," *IEEE J. Quantum Electron.*, QE-23, pp. 988, 1987.
84. H. Kressel and J. K. Butler, *Semiconductor Lasers and Heterojunction LEDs* (Academic, New York, 1975), pp 559-562.
85. Y. Arakawa, and T. Takahashi, "Effect of nonlinear gain on modulation dynamics in quantum-well lasers," *Electron. Lett.*, vol. 25, pp. 169-170, Jan 1989.
86. B. Zhao, T. R. Chen, and A. Yariv, "Comparison of differential gain in single quantum well and bulk double heterostructure lasers," *Electron. Lett.*, vol. 27, pp. 2343-2344, 1991.
87. B. Zhao, T. R. Chen, and A. Yariv, "Effect of state filling on the modulation response and the threshold current of quantum well lasers," *Appl. Phys. Lett.*, vol. 60, pp. 1930-1932, April 1992.
88. A. Ghiti, and E. P. O'Reilly, "Nonlinear gain effects in strained-layer lasers," *Electron. Lett.*, vol. 26, pp. 1978-1980, Nov. 1990.
89. C. B. Su and V. Lanzisera, "Ultra-high-speed modulation of 1.3μm InGaAsP diode lasers," *IEEE J. Quantum Electron.*, vol. QE-22, p1568, 1986.
90. W. F. Sharfin, J. Schlafer, W. Rideout, B. Elman, R. B. Lauer, J. LaCourse, and F. D. Crawford, "Anomalously high damping in strained InGaAs-GaAs single quantum well lasers", *IEEE Photon. Technol. Lett.*, vol 3, pp. 193-195, March 1991.
91. G. P. Agrawal, "Effect of gain nonlinearities on the dynamic response of single-mode semiconductor lasers," *IEEE Photon. Technol. Lett.*, vol. 1,

pp. 419-421, 1989.

92. J. E. Bowers, "High speed semiconductor laser design and performance," *Solid-State Electron.*, vol. 30, pp. 1-11, 1987.
93. D. J. Channin, "Effect of gain saturation on injection laser switching," *J. Appl. Phys.*, vol. 50, pp. 3858-3860, 1979.
94. G. P. Agrawal, "Modulation bandwidth of high-power single-mode semiconductor lasers: Effect of intraband gain saturation," *Appl. Phys. Lett.*, vol. 57, pp. 1-3, 1990.
95. M. Yamada, and Y. Suematsu, "Analysis of gain suppression in undoped injection lasers," *J. Appl. Phys.*, vol. 52, pp. 2653-2664, 1981.
96. D. Ahn and S. L. Chuang, "Optical gain and gain suppression of quantum well lasers with valence band mixing," *IEEE J. Quantum Electron.*, vol. 26, pp.13-24, 1990.
97. M. Willatzen, T. Takahashi, and Y. Arakawa, "Nonlinear gain effects due to carrier heating and spectral hole burning in strained-quantum-well lasers," *IEEE Photon. Technol. Lett.*, vol. 4, pp. 682-684, July 1992.
98. T. Ohtoshi and N. Chinone, "Linewidth enhancement factor in strained quantum well lasers," *IEEE Photon. Technol. Lett.*, vol. 1, pp. 117-119, 1989.
99. A. Larsson and C. Lindstrom, "Modulation bandwidth of GaAs/AlGaAs single quantum well lasers operating at the second quantized state," *Appl. Phys. Lett.*, vol. 54, pp. 884-886, 1989.
100. J. Yao, O. Gallion, W. Elsässer, and G. Debarge, "Nonlinear gain and its influence on the laser dynamics in single-quantum-well lasers operating at the first and second quantized states," *IEEE Photon. Technol. Lett.*, vol. 4, pp. 1210-1212, 1992.
101. C. H. Henry, "Theory of linewidth of semiconductor lasers," *IEEE J. Quantum Electron.*, vol. 18, pp. 259-264, 1982.
102. K. Vahala and A. Yariv, "Semiclassical theory of noise in semiconductor lasers - Part I," *IEEE J. Quantum Electron.*, vol. 19, pp. 1096-1101, 1983.
103. N. K. Dutta, H. Temkin, T. Tanbun-Ek, and R. A. Logan, "Linewidth enhancement factor for InGaAs/InP strained quantum well lasers," *Appl. Phys. Lett.*, vol. 57, pp. 1390-1391, 1990.
104. B. W. Hakki and T. L. Paoli, "Gain spectra in GaAs double heterostructure injection lasers," *J. Appl. Phys.*, vol. 46, pp. 1299-1306, 1975.
105. M. Asada and Y. Suematsu, "The effects of loss and nonradiative recombination on the temperature dependence of threshold current in 1.5 - 1.6 μm GaInAs/InP lasers," *IEEE J. Quantum Electron.*, vol. 19, pp. 917-923, 1983.
106. Y. Arakawa, and A. Yariv, "Theory of gain, modulation response, and spectral linewidth in AlGaAs quantum well lasers," *IEEE J. Quantum*

Electron., vol. 21, pp. 1666-1674, 1985.

107. T. Yuasa, T. Yamada, K. Asakawa, M. Ishii, and M. Uchida, "Very high relaxation oscillation frequency in dry-etched short cavity Gaas/AlGaAs multiquantum well lasers," *Appl. Phys. Lett.*, vol. 50, pp. 1122-1124, 1987.
108. N. Ogasawara, R. Ito, K. Tone, and H. Nakae, "Dispersion of the linewidth enhancement factor in semiconductor injection lasers," *Jap. J. Appl. Phys.*, vol. 23 pp. L518-L520, 1984.
109. N. K. Dutta and R. J. Nelson, "Temperature dependence of the lasing characteristics of the 1.3 μm InGaAsP - InP and GaAs - $Al_{0.36}Ga_{0.64}As$ DH lasers," *IEEE J. Quantum Electron.*, vol. 18, pp. 871-878, 1982.
110. C. Su and V. Lanzisera, "Effect of doping level on the gain constant and modulation bandwidth of InGaAsP semiconductor lasers," *Appl. Phys. Lett.*, vol. 45, pp. 1302-1304, 1984.
111. W. Cheng, S. Huang, A. Appelbaum, J. Pooladdej, K. Buehring, D. Wolf, D. Renner, K. Hess, and S. Zehr, "Wide-band modulation of 1.3 μm InGaAsP buried crescent lasers with Iron- and Cobalt-doped semi-insulating current blocking layers," *IEEE J. Quantum Electron.*, vol. 25, pp. 1352-1361, 1984.
112. J. Manning, R. Olshansky, and C. B. Su, "The carrier induced index change in AlGaAs and 1.3 μm InGaAsP diode lasers," *IEEE J. Quantum Electron.*, vol. 19, pp. 1525-1530, 1983.
113. Y. Arakawa and A. Yariv, "Fermi energy dependence of linewidth enhancement factor of GaAlAs buried heterostructure lasers," *Appl. Phys. Lett.*, vol. 47, pp. 905-907, 1985.
114. S. Hausser, W. Idler, E. Zelinski, M. H. Pilkuhn, G. Weimann, and W. Schlapp, "Spontaneous emission factor and waveguiding in GaAs/AlGaAs MQW lasers," *IEEE J. Quantum Electron.*, vol. 25, pp. 1469-1476, 1989.
115. K. J. Beernink, J. J. Alwan, and J. J. Coleman, "InGaAs-GaAs-AlGaAs gain-guided arrays in the in-phase fundamental array mode," *Appl. Phys. Lett.*, vol. 57, pp. 2764-2766, 1990.
116. M. M. Fejer, G. A. Magel, D. H. Jundt and R. L. Byer, "Quasi-phase-matched second harmonic generation: tuning and tolerances," *IEEE J. Quantum Electron.*, vol. 28, pp. 2631-2654, 1992.

APPENDIX A

This appendix is a table of the processing steps used in the fabrication of gain-guided stripe-geometry lasers of different cavity lengths and stripe widths.

1.	Wafer cleaning	(a) Clean with Acetone, Methanol or IPA, DI water (b) N_2/O_2 Plasma cleaning (c) Dip in HCl + DI solution to remove native oxide and rinse with DI and blow dry.
2.	Photolithography	(a) Resist spinning (i) Place a few drops of HMDS (ii) Spin : 5s @ 2k rpm and 60s @3.3k rpm (iii) Place a few drops of 1811 photoresist (iv) Spin as in step (ii) (b) Soft bake @ 100 °C for 60s on hot plate (c) Edge bead removal (i) Use mask with suitable pattern according to wafer size to expose only the edges (ii) Expose for 3 min to remove edge bead (iii) Develop in AZ400k solution (≈ 120s) (iv) Rinse with DI and blow dry (d) Pattern wafer with suitable mask (e) Develop in AZ400k, rinse and dry
3.	Etching of p+ GaAs cap layer	Three ways to do it : (a) Selective etch Citric acid solution + H_2O_2 (10 : 1) Citric acid solution is 50% by weight of citric acid in H_2O. Etch rate is ≈ 0.25 μm/s (NOTE: etches p+ GaAs and n type AlGaAs and NOT p+ type AlGaAs) (b) HCl + H_2O_2 in H_2O (2:6:100) Etch rate ≈ 30 Å/s (c) Phosphoric etch H_3PO_4 + H_2O_2 + DI H_2O (3 : 1 : 25) Etch rate ≈ 32 - 33 Å/s (NOTE : Etch profile independent of crystal orientation)

4.	Resist removal	Rinse with acetone, DI and blow dry Place the wafer in dehumidifier overnight
5.	P metallization	(a) Solvent cleaning (i) 3 beakers of 100 ml of TCE, hot (not boiling) (ii) Dip in each (5 min) and transfer to next (iii) Repeat (ii) in hot acetone but not boiling (iv) Repeat (ii) in hot IPA but not boiling (v) Rinse wafer in room temperature IPA for 30s (vi) Rinse wafer in DI and blow dry (b) Dry N_2/O_2 plasma cleaning for oxygen descum (c) Standard acid etch to remove oxide layer (d) Metal deposition Deposit 50 nm of Ti, 50 nm of Pt and 250 nm of Au in that order
6.	Lapping	Substrate to be thinned to ≈ 100 ± 25 μm
7.	N Metallization	Steps (a) through (c) as in step 5 (d) Metal deposition Deposit 100 nm of Au/Ge, 20 nm of Ni, and 100 nm of Au (e) Alloying Alloy for 90s @ 430 °C with forming gas (10% H_2 , 90% N_2)
8.	Cleaving	Scribe and cleave wafer

APPENDIX B

This appendix provides the details of the temperature control circuit that was used to monitor and control the temperature of the laser mount using a thermo-electric cooler and a thermistor.

Note:

(1) With R = 380 Ω, the voltage across the 20 kΩ potentiometer, for ±10V supplies, is ≈ 1V. This range can be changed by different value for R.

(2) The potentiometer is a 10 turn pot. Thus @5 it is 0V, @0 it is -0.5V and @10 it is +0.5V

(3) The analog output of the OMEGA temperature controller provides a 10mV/°C signal. Thus, in principle, a temperature range of - 50 °C to + 50 °C can be controlled.

(4) Relay ON : Switch open ; Relay OFF : Switch closed . Relay is off in normal operation. When thermal runaway happens, i.e., $T > T_{S2}$, then 2N3904 is ON, which switches the Relay to be ON, i.e., switch is now open, and hence no current to TE module. T_{S2} can be set to, say 10 °C above T_{S1} .

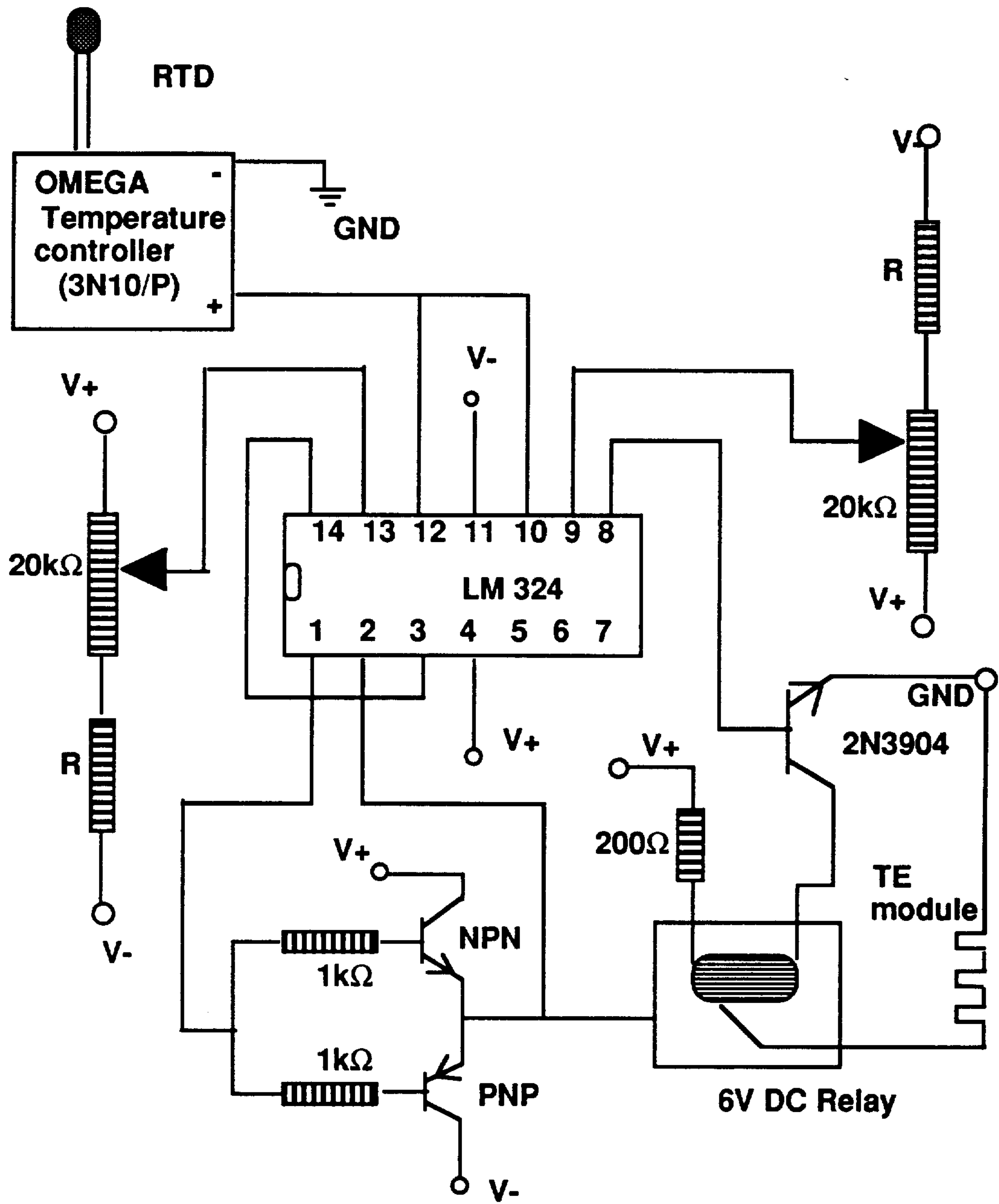

Schematic representation of the temperature control circuit using active feedback with the RTD and TE module.

VITA

Raghuraman Ranganathan was born in the state of Tamil Nadu, India on June 14, 1963. He attended D. G. Vaishnav (University of Madras) in Madras, India, and received the degree Bachelor of Science in Physics in May 1984. Subsequently, he joined the Department of Physics at the Indian Institute of Technology, Madras, India to pursue graduate studies in Physics, receiving the degree Master of Science, M.Sc (Physics), in July 1986. Continuing at the same institution, he completed all requirements by August 1988 and received the degree Master of Science, M.S (Engineering), from the Department of Electrical Engineering in August 1990.

The author began his studies at the Orgeon Graduate Institute of Science & Technology (formerly Oregon Graduate Center) in September 1988 to work towards his Ph.D and completed all requirements for the degree Doctor of Philosophy (Ph.D.) in Electrical Engineering in January 1993.

His research interests are semiconductor lasers, optoelectronics and optical communication.

List of Publications

Journals:

1. "Spectral dependence of the differential gain, mode shift and the linewidth enhancement factor for strained-layer InGaAs/GaAs single-quantum-well laser operated under high injection conditions", R. Raghuraman, Nu Yu, R.Engelmann, H. Lee and C. L. Shieh (*IEEE J Quant. Electron.* , vol. 29, 69, Jan '93).

2. "Stripe-width and cavity length dependent wavelength switching in strained-layer InGaAs/GaAs single quantum well lasers", R. Raghuraman, R. Engelmann and J. R. Arthur. (to be submitted.)

Conferences and Meetings:

1. "Sub-threshold gain and refractive index variation in InGaAs/GaAs strained-layer quantum-well devices", R. Raghuraman, Nu Yu, and R. Engelmann, presented at the Annual meeting of the Oregon Academy of Sciences , OR., Feb 1991.
2. "Linewidth enhancement factor in narrow-stripe strained-layer InGaAs/GaAs single-quantum well laser operated under high injection conditions", R.Raghuraman, Nu Yu, R. Engelmann, H. Lee, and C. L. Shieh, presented at IEEE/LEOS meeting at San Jose, CA., Nov, 1991.
3. "Observation of increased recombination from the barriers in strained layer InGaAs/GaAs quantum well lasers grown by Molecular Beam Epitaxy", R.Raghuraman, R. Engelmann and J.R. Arthur, presented at the Annual meeting of the Oregon Academy of Sciences, Feb 1992.
4. "Simple model for carrier spill-over in quantum-well lasers consistent with local charge neutrality", Y. Cai, R. Engelmann and R. Raghuraman, OSA '92 Annual meeting, Albuquerque, New Mexico, Sept 1992.
5. "Dual wavelength laser operation in lossy gain-guided InGaAs/GaAs strained-layer quantum-well laser stripe", R. Raghuraman, R. Engelmann and J. R. Arthur, OSA '92 Annual meeting, Albuquerque, New Mexico, Sept 1992.